Transverse Energy Distributions, Global Event Shapes, and Flow Study in Ultra-relativistic Heavy Ion Collisions

A Dissertation Presented

by

Yingchao Zhang

to

The Graduate School

in Partial Fulfillment of the Requirements

for the Degree of

Doctor of Philosophy

in

Physics

State University of New York
at
Stony Brook

August 1995

State University of New York
at Stony Brook

The Graduate School

Yingchao Zhang

We, the dissertation committee for the above candidate for the **Doctor of Philosophy** degree, hereby recommend acceptance of the dissertation.

Johanna Stachel (advisor)
Professor of Physics

Edward Shuryak
Professor of Physics

Robert L. McGrath (chair)
Professor of Physics

Roy A. Lacey
Assistant Professor of Chemistry

This dissertation is accepted by the Graduate School.

Graduate School

Abstract of the Dissertation

Transverse Energy Distributions, Global Event Shapes, and Flow Study in Ultra-relativistic Heavy Ion Collisions

by

Yingchao Zhang

Doctor of Philosophy

in

Physics

State University of New York at Stony Brook

1995

Transverse energy (E_T) production in 11.4 A·GeV/c Au + Au collisions at the BNL AGS has been measured over nearly the full solid angle with the E877 apparatus. While the longitudinal spectra $dE_T/d\eta$ indicate a large degree of stopping of the colliding nuclei and stronger longitudinal expansion than the transverse one, the study of azimuthal event shapes is the main subject of this thesis. The azimuthal anisotropy, which is based on the collective flow phenomena, reflects the collision dynamics and is sensitive to the nuclear equation of state (EOS). A novel Fourier expansion analysis is introduced and discussed in detail after an overview of the other existing methods. The Fourier expansion approach is applied to azimuthal distributions of E_T in different pseudorapidity intervals. For the first time at ultra-relativistic energies, an azimuthal anisotropy is observed and quantified as a function of collision centrality in heavy ion collisions. For semi-central collisions a pronounced event anisotropy reaches its maximum with a clear forward-backward anti-correlation. The signals decrease for peripheral and very central collisions. Comparisons with cascade and hydrodynamical model calculations show that the observed flow signals are larger than those from a cascade model, but smaller than those from a hydrodynamical calculation.

To my grandma

⌣̈

for all her love

♡

Contents

List of Figures

List of Tables

Preface

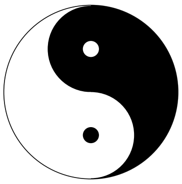

Let us begin with the above diagram, a symbol for the *Taoism*, an ancient Chinese philosophy. It is known as *Yin Yang* 阴阳, where the *Yin* (dark) and the *Yang* (bright) are arranged in a symmetric yet non-static way, illustrating the co-existence of opposing aspects in harmony within one object. Niels Bohr used this symbol to explain quantum mechanics, in which a sub-atomic object can be characterized by a wave on the one hand, and a particle on the other. The Yin Yang relationship can also be found in many other physics concepts or objects, *e. g.*, positive and negative charge, matter and anti-matter.

The original name for this symbol is *Tai Ji* 太极, or "the Supreme Ultimate". According to Taoism, it is only the *Tao* (can be translated to "law" or "nature") that exists forever, and has created our universe out of nothing. Starting from zero (the big circle), zero produces one (the "S" curve in the middle), then one splits to two (the white and black dots), and two produce everything. This is similar in concept to the "big-bang" theory, where the current universe was created fifteen billions years ago from a single point containing all energies in any form in our present universe after a big explosion.

The circles and the rotational symmetry in the diagram represent ceaseless cyclic motions and changes of nature. “Returning is the motion of the *Tao*”, “Going far is returning”; these are the words from the master and creator of the Taoism, Lao Zi (or Lao Tzu). From that, I believe a “big-collapse” will happen ultimately, which will be the end of the present universe, but the beginning of the next universe following another “big-bang”.

For the purpose of flow analysis, which is the central topic of this thesis, the picture can be viewed as a collision between two nuclei at a finite impact parameter. The black and white dots are the center of the projectile and target nuclei, and the “S” curve between the beam (white) and target (black) is the shock front produced by compression during the collision. The deflection of the particles generates an up-down asymmetry, and the sideward flow is generated naturally from this picture.

Interested readers are referred to Capra [1] for more discussion on the parallel relations between the *Tao* and modern physics. However, the meaning and interpretations of the symbol are certainly not limited to physics. To me, it is the way of life.

Acknowledgements

I would like to express my deepest gratitude towards my thesis advisor Prof. Johanna Stachel. Other than members of my family, she has given me the biggest impact that has changed the trajectory of my life forever. Her advice was crucial to the success of my thesis work from the beginning through the end. Her generous support made it possible for me to have many opportunities to explore my future in the field, and, more importantly, her enthusiasm for physics and her tireless attention on her work set me an icon and motivated me throughout out my years at Stony Brook. I am especially grateful to her for spending tremendous amount of time on reading, correcting, and commenting on my thesis, from the general contents to the many mistakes in my use of English. I would also like to thank Profs. Robert L. McGrath, Edward Shuryak, and Roy A. Lacey for serving on my thesis committee.

I got to know our group leader Prof. Peter Braun-Munzinger from his nuclear physics class, which I took as a breadth course at the time. I was inspired by his teaching, and joined his group later on. I have had his advice and support ever since. Dr. Nu Xu was the other reason that I joined the group. His invaluable encouragement kept me up during the early days in the

group, and the discussions between us on physics or non-physics issues are always interesting and exciting. Prof. Thomas. K. Hemmick impressed me the most with his excellent programming skills, and his positive attitude towards things and people around him. It has always been fun to talk to him, and I wish I could have gotten more chances to work with him during my stay at Stony Brook. I also would like to thank him for his support on many occasions which were invaluable to me.

I am deeply indebted to Dr. Sergei Voloshin for stimulating discussions which led to the Fourier analysis approach presented in Chapter 2 that is essential for the successful flow analysis. Drs. Gabor David, Norbert Hermman, and Johannes Wessels are sincerely acknowledged for helpful discussions at the early stage of the flow analysis. I am grateful to Dr. Zhenzhi Zhang, whose efforts on PCAL maintenance and calibration made it possible to measure flow with this device.

My fellow students Chuan-Ming Zou, Byungsik Hong, and James Dee, who all joined the group in the same year as I did, Sergey Panitkin and Youngil Kwon, who joined us one year later, deserve my special thanks. The working relationship and the warm friendship between us contributed the most to my pleasant experience in the group. I also indebted to the following former group members for early guidance in my research efforts: Rene Bellwied who introduced me to the data analysis; Gabor David for being nice to me and patient with all my questions; William J. Llope who taught me everything about UCAL; Moorthy Muthuswamy with whom I had many discussions on physics; Laurie Waters from whom I inherited a wealth of computer programs

for TCAL analysis. Among the "junior" students at Stony Brook, I benefited the most from discussions (sometime they went beyond physics) with Wen-Chen Chang. I pray with him (even though I am not a Christian) that there will never be a war between Mainland China and Taiwan, and I hope we will keep our friendship regardless what happen in the future.

To the rest of the group including former group members, Rich Bersch, Gami Dadusc, Rich Hutter, Stephen Johnson, Dariusz Miskowiec, Timothy Piazza, Mark Pollack, Modala N. Rao, Sergey Sedykh, Martin Trzaska, and Thongbay Vongpaseuth, it has been my pleasure to know you and to work with you, and I thank you all. I also thank all the members of the E814/E877 collaboration who have made the experiment a success. To my Chinese friends here at Stony Brook, the friendship and social life you brought to me reduced my homesickness and enlightened my life, and I wish our friendship will last long even if we are no longer together.

To save the best for last, I thank my parents, my sister, and my dearest wife for their love and support, and to whom I dedicate this thesis. But most of all, it is dedicated to my grandma who loves me with all her heart. She cares the most for who I am, and the least for what I have accomplished. She won't be able to read my thesis, but from the bottom of my heart, grandma, this is for you.

Chapter 1

Introduction

1.1 Quark Gluon Plasma and Relativistic Heavy Ion Collisions

Our current understanding of cosmology and particle physics tells the following story. Some fifteen billions years ago, the current universe was born after a huge explosion – the "big-bang". It all came from a single point containing tremendous energy, which was released into the surrounding vacuum and converted to all forms of matter. All elementary particles were formed at a very early stage, including quarks, leptons and gauge bosons (photons, gluons, W and Z). Initially quarks and gluons were interacting and moving freely in a phase called *quark gluon plasma* (QGP), and hadrons were not formed until about 10^{-6} sec after the big-bang. At this stage, where the temperature (T) was about 150 MeV, quarks and gluons started to condense into confined hadrons, in the form of either a quark anti-quark pair (meson), or three quarks (baryon). This process is called the *confinement* phase transition, or hadronization. Free quarks and bare gluons disappeared except for a possible existence in the core of remote neutron stars. Can we prove the above theory by reproducing a small version of big-bang in the laboratory, in which a QGP can be formed via the *deconfinement* phase transition? Relativistic heavy ion collisions will probably provide the unique answer to this question.

According to the theory of quantum chromodynamics (QCD), the critical conditions for the phase transition are reached at a critical temperature $T_c \simeq$ 150 MeV, or a critical energy density ϵ_c= 2-3 GeV/fm^3 [2]. These conditions might be achieved when two heavy ions collide head-on with each other at extremely high energy, and deposit sufficient energy in the center of mass. To create a QGP in the laboratory and to explore its properties serves as the main goal for studying ultra-relativistic heavy ion collisions.

Table 1.1: List of current or proposed facilities, the ion beams, and the corresponding beam momentum and center of mass energy per nucleon pair.

Machine	Location	Ion beam	Momentum (A·GeV/c)	$\sqrt{s}$ † (GeV)	Start of experimental program
AGS	BNL	^{16}O, ^{28}Si	14.6	5.4	Oct 1986
		^{197}Au	11.4	4.8	Apr 1992
SPS	CERN	^{16}O, ^{32}S	200	19.4	Sep 1986
		^{208}Pb	160	17.4	Nov 1994
RHIC	BNL	^{197}Au	100	200	Spring 1999
LHC	CERN	^{208}Pb	3150	6300	$\sim$ 2005 (projected)

† per nucleon-nucleon pair for a symmetric colliding system.

Since the spring of 1986 various experiments have taken place both at the Alternating Gradient Synchrotron (AGS) at Brookhaven National Laboratory (BNL), and the Super Proton Synchrotron (SPS) at CERN [3]. Within four and ten years, respectively, the Relativistic Heavy Ion Collider (RHIC) at BNL and the Large Hadron Collider (LHC) at CERN will come online, and many proposed experiments will complete the study and hopefully fulfill our goal. Table 1.1 lists the facilities and the invariant mass per nucleon-nucleon pair. In the nuclear phase diagram of energy density versus baryon density, one expect to explore the high baryon density axis at the AGS and SPS, and the high energy density axis with a baryon-free (or low) environment at RHIC and the LHC.

In the past eight years, much progress has been made in the field, yet the observation of a phase transition remains uncertain. A recent review of the experiments both at the AGS and SPS has been given by Stachel and Young [4]. In recent years, the proceedings of Quark Matter Conferences have provided a rather complete set of references on both theoretical and experimental developments [5, 6, 7, 8, 9, 10, 11, 12]. There are two achievements worth mentioning here. Firstly, transverse energy and baryon rapidity distributions indicate a large degree of stopping at AGS [13, 14, 15, 16] and SPS [17] energies. Secondly, at AGS energies there are quite convincing data and interpretation to support the notion that thermal and chemical equilibration has been reached to some extent [18, 19, 20].

1.2 Signatures for the Phase Transition

It is intuitively simple to imagine a phase transition at high baryon density or high temperature. The hadron density is dramatically increased in both cases, via compression of the incident baryons or formation of mesons and baryons, respectively. When the average distance between two neighboring quarks becomes so short that they all interact perturbatively in the limit of asymptotic freedom, the boundary of the hadron becomes meaningless, and a QGP is believed to be formed. Since perturbative QCD does not work for a large scale regime, it is difficult to describe the nature of the phase transition from first principles. A promising approach to study the phase transition is the numerical solution of Lattice QCD (LQCD). Although the calculations are extremely time consuming, they produce more accurate results as the size of the lattice is increased. A result from a calculation with only gluons predicts a critical temperature of about 200 MeV and a first order phase transition [22]. More detailed calculations including the low mass quarks, up (u) and down (d), have shown that the transition is second order [23]. The most recent results show that the transition is perhaps continuous but still confined to a narrow temperature range [12].

In order to prove the existence of a QGP and a phase transition, one needs observables or "signatures", which are sensitive to the presence of a QGP phase or the phase transition itself, in heavy ion collisions. The first type of signature is based on exclusive measurements of certain rare particle species. The second type measures thermodynamic variables. Signatures of the first type, *e. g.*, strangeness enhancement or J/ψ-suppression, are sometimes ambiguous since they can also be produced by hadronic physics. The thermodynamic variables, on the other hand, are sensitive to the phase transition itself. The idea is to measure the equation of state (EOS), and look for a discontinuity in quantities such as ϵ/T^4 or s/T^4 (s is the entropy density) over a small region in T. The thermodynamic variables can be inferred from experiments, such as T from $\langle p_t \rangle$ or hadron abundances, ϵ or s from dE_T/dy or dN/dy. This is only an approximation. For example, one can argue that the $\langle p_t \rangle$ variable from hadrons reflects the temperature and the expansion flow velocity near freeze-out, not during the phase transition. Direct photons and leptons, which are more penetrating than hadrons, may carry out the initial information, but are difficult to measure.

The flow signal is a good candidate as a signature of the phase transition. Similar to the thermodynamic variables, we seek a discontinuity in the flow signal as a function of beam energy, size of the system or the impact parameter. Even if a small drop of QGP is formed in the collision zone, the EOS of the matter will be soft and the flow signal will be reduced. The difficulty for this study is three-fold. It requires more beam time and different beam energies for a systematic study; it demands a large acceptance apparatus to detect the shape of the whole event; and it needs an effective approach to extract the signal from the experimental data.

1.3 Equation of State and Flow Studies

In a system in complete equilibrium, particles are moving thermally and randomly. There is no net current at any space point at any time. If a current exists, collective motion is present on top of the thermal motion, which is called flow. The flow velocity is thus the velocity of the center of mass of the co-moving particles relative to the center of mass of the whole system.

The concept of flow comes from hydrodynamics. It was introduced to nuclear collisions by Scheid, Müller, and Greiner in 1974 [24]. Following hydrodynamical considerations, they anticipated that nuclear matter, if stopped in central collisions, is compressed and heated, and may subsequently expand primarily in the direction perpendicular to the beam axis. The experimental studies to test these ideas began in 1978 at the Bevalac (at Lawrence Berkeley Laboratory) and are presently being pursued in heavy ion collisions from intermediate energies (*e. g.*, at NSCL, Michigan State University) to relativistic energies (SIS at GSI, Darmstadt) to ultra-relativistic energies (BNL AGS and CERN SPS). Extensive amounts of data have been collected for different systems with detectors ranging from emulsion trackers [25] to sophisticated electronic detectors like the 4π Equation of State Time Projection Chamber (EOS TPC) [26]. A review of results from all major experiments up to 1989 is given in [27]. The results for beam energies ranging from 60 MeV to 1 GeV per nucleon have established collective flow as an experimental fact. Recent investigations have focused on measurements involving different particle species, especially mesons and resonances. On the theoretical side, initially only the hydrodynamic models were able to explain the data quantitatively [28], while the intra-nuclear cascade (INC) model failed [29]. The implementation of viscosity to the hydrodynamic model calculations helped to improve the quantitative agreement with data [30, 31]. With proper inputs of compressibility, transport models (*e. g.*, BUU[32]) have shown good agreement with data. A recent paper by Danielewicz discusses a transport model with detailed treatment of the shock wave and the effects of compression and collective expansion on particle emission [33]. The question now is whether or not the flow phenomena still exists at much higher energies.

It is the intention of this thesis to answer this question. To be more specific, the question is whether or not flow is present in heavy ion collisions at ultra-relativistic energies such as at the AGS. There have been a few flow analyses carried out before this thesis work. An analysis by G. David of the E814 Collaboration did not reveal any azimuthal asymmetry in Si on Pb collisions within the detectors' sensitivity [34]. The E802 Collaboration has reported a correlation between particle production ratios and the transverse momenta of projectile fragments for Si on Au collisions [35]. However the latter result is not conclusive enough to establish the existence of flow at AGS energies. With the truly heavy Gold (Au) beam, it is time to give a definite answer to this question. Note that at the Bevalac, flow was discovered only when a heavy beam such as La became available.

In Chapter 2 we discuss approaches used in the flow analysis. The Experiment 877 at the AGS is briefly introduced in Chapter 3, including apparatus and data collection and event selection. Details of the data analysis are presented in Chapter 4. The global variables and their correlations are discussed first, followed by a discussion of transverse energy longitudinal distributions. The rest of the analysis effort is devoted to an azimuthal event shape analysis, which is the main thrust of this thesis. In Chapter 5, we compare our results of the azimuthal distributions with a cascade model, and a hydrodynamical model. Chapter 6 summarizes the main results of this thesis and gives an outlook towards future flow analysis.

For the most part, we will discuss the azimuthal transverse flow. This being the case, terms like "flow", "anisotropy", and "azimuthal asymmetry" will be used interchangeably. There could be different origins for the anisotropy: hydrodynamical flow due to pressure gradients, shadowing, both, or some other mechanism we do not know yet.

Chapter 2

Approaches for Flow Analyses

2.1 Introduction

In the study of specific processes such as the flow phenomena, it is very important to find variables which are easy to work with and which have clear physical interpretations. In this chapter a general and novel approach is proposed for the study of flow phenomena in ultra-relativistic nuclear collisions. Not only does this approach include almost all pre-existing methods in a natural way, but it also clarifies their interrelation, and gives a clear physical meaning to the whole analysis. Moreover, it permits the detection of flow and the reconstruction of event shapes without determination of the reaction plane on an event-by-event basis. Reaction plane determination is often ambiguous due to finite multiplicity fluctuations.

An overview of all the previously used methods in flow analyses is given in Sec. 2.2. For each method, the definition and physical meaning is given, followed by brief discussions of the advantages, disadvantages, and the relationship to other methods. In Sec. 2.3 we introduce the new Fourier expansion approach, and explain its physical meaning. The fluctuations due to finite particle multiplicity are discussed in detail in Sec. 2.4. It is also shown how to detect flow without the reconstruction of the reaction plane event-by-event, which is the central core of the azimuthal data analysis in this thesis. The reaction plane resolution due to fluctuations is still an interesting topic itself. The analytical formula for the dispersion and related questions are discussed in Sec. 2.5. Based on these formulae, an azimuthal correlation between flow angles in different (pseudo)rapidity windows is expected. This correlation provides an alternative way to detect flow, and is presented in Sec. 2.6. The advantages as well as the limitations of the new method are addressed in Sec. 2.7.

Figure 2.1: Definition of the coordinates, the impact parameter, and the reaction plane. In this particular case, the reaction plane angle is $\psi_r = \pi$.

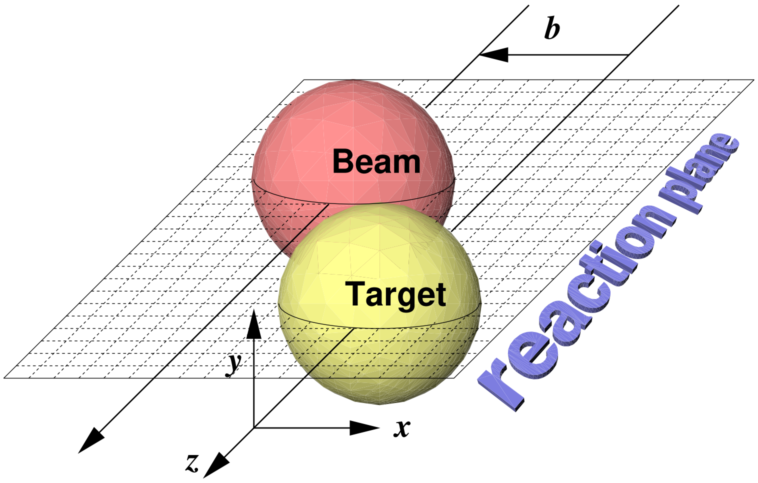

Table 2.1 lists the definition of the coordinates and some physical variables, and symbols used in this thesis. Many other specific quantities are defined through out the text. Fig. 2.1 illustrates schematically the definitions of the coordinates, the impact parameter, and the reaction plane.

2.2 Review of Previously Used Methods

2.2.1 Directivity

The $\mathbf{Q}$ vector,[1] which is also referred as directivity, was originally introduced in the flow analysis by Danielewicz and Odyniec in 1985 [36]:

$$\mathbf{Q} = \sum_{\nu=1}^{M} \omega_\nu \mathbf{p}_{t;\nu} \, , \tag{2.1}$$

where $\mathbf{p}_{t;\nu}$ is the transverse momentum vector of the ν-th particle, ω_ν is a weight factor, and M is the particle multiplicity. Normally $\mathbf{Q} \equiv (Q, \psi)$ [2] is constructed event-by-event from baryons only, with $\omega_\nu = 1$ for $y_\nu > y_c + \delta$, $\omega_\nu = -1$ for $y_\nu < y_c - \delta$, and $\omega_\nu = 0$ otherwise. For symmetric collisions

[1] To follow prior conventions, vectors are written in **boldface**.

[2] Note that $\mathbf{Q}$ is a 2-D vector in the transverse plane.

Table 2.1: Definition of coordinates, variables and abbreviations.

coordinate related quantities	$\mathbf{b} = (b, \psi_r)$	impact parameter vector, from the center of the target to the trajectory of the center of the beam at distance of closest approach
	ψ_r	the reaction plane angle ($0 \le \psi_r < 2\pi$)
	z-axis	longitudinal or beam direction
	x, y axes	transverse directions in laboratory †
	t or T	subscript of transverse components of the physical quantities ‡
	θ, ϕ	particle's polar and azimuthal emission angle
	ϑ, ψ	polar and azimuthal angle obtained for event variables
	1-D, 2-D, 3-D	one, two or three dimension(al)
physical quantities	p, ϵ	particle's momentum and total energy
	p_t, ϵ_t	transverse momentum and energy $p_t = p \sin\theta$, $\epsilon_t = \epsilon \sin\theta$
	p_x, p_y, p_z	$p_x = p_t \cos\phi$, $p_y = p_t \sin\phi$, $p_z = p\cos\theta$
	M	multiplicity, number of particles
	P_T, E_T	$P_T = \sum_{\nu=1}^{M} p_{t;\nu}$, $E_T = \sum_{\nu=1}^{M} \epsilon_{t;\nu}$
	y	rapidity $y = \frac{1}{2}\ln\frac{\epsilon+p_z}{\epsilon-p_z}$
	η	pseudorapidity $\eta = \frac{1}{2}\ln\frac{p+p_z}{p-p_z} = -\ln\tan(\theta/2)$
misc.	N	number of events
	$r.m.s.$	root mean square
	σ	cross-section, or standard deviation
	dw/dx	event probability distribution for variable x,
	c.m.s.	center of mass system

† Normally the x-axis is the horizontal axis in the laboratory frame. Sometimes it is in the direction of the reaction plane (*i. e.*, $\psi_r = 0$) if declared in the text.
‡ In my own convention, lower case is usually used for quantities associated with individual particles, while upper case for event quantities after integration or summation over the particles in a given acceptance.

y_c is the overall c.m.s. rapidity. The quantity δ removes particles from the region around mid-rapidity which do not contribute to the determination of the reaction plane, and can be chosen experimentally to optimize the reaction plane resolution. The angle ψ can be used to measure the reaction plane in an event, while the amplitude Q determines the net transverse momentum transfer in the event.

To estimate the accuracy of the reaction plane angle ψ, the authors [36] introduced a sub-event scheme, to randomly divide each event into two, and compare the measured reaction plane angles ψ_I and ψ_{II}. A non-flat distribution $dN \ / \ d(\psi_I \ - \ \psi_{II})$ testifies to the determination of the reaction plane. They did a Monte Carlo study, and obtained the ψ distribution with respect to the true reaction plane, but did not provide the analytical form for it. The authors then argued the width of ψ should be factor of 2 smaller than the width of $\psi_I - \psi_{II}$, which is approximately but not exactly true. It is correct in the limit that the flow is strong and both distributions are close to a one dimensional Gaussian distribution. We will discuss this in detail later in Sec. 2.5.

Squaring Eq. (2.1) one obtains:

$$Q^2 = \sum_\nu \omega_\nu^2 p_{t;\nu}^2 + \sum_{\mu \neq \nu} (\omega_\mu \mathbf{p}_{t;\mu}) \cdot (\omega_\nu \mathbf{p}_{t;\nu}). \tag{2.2}$$

Averaging over many events of the same centrality, if the $\mathbf{p}_{t;\nu}$ are randomly oriented, one obtains $\langle Q^2 \rangle = \langle \sum_\nu p_{t;\nu}^2 \rangle$.[3] On the other hand, if an anisotropy is present, the mean of the weighted transverse momentum is non-zero,

$$\langle \frac{\omega p_x}{m} \rangle \simeq \left(\frac{\langle Q^2 - \sum_\nu p_{t;\nu}^2 \rangle}{\langle A^2 - \sum_\nu m_\nu^2 \rangle} \right)^{1/2}, \tag{2.3}$$

where the x-axis lies in the reaction plane, m_ν is the mass of ν-th particle, and $A = \sum_\nu m_\nu$. If one takes only one particle species in the forward (or backward) rapidity region, one can get the mean transverse momentum into the true reaction plane $\langle p_x \rangle$ from Eq. (2.3).

The most commonly used scheme applying this method is to calculate $\langle p_{x'} \rangle$ as a function of rapidity (y), where x' is the direction of the measured

[3]Note that $\omega_\nu^2 = 1$ if one excludes the particles around mid-rapidity from the summation.

reaction plane. To avoid auto-correlations, the reaction plane is usually determined for each particle of interest, which is not included in the reaction plane determination,

$$p_{x';\nu} = p_{t;\nu} \cdot \mathbf{Q}_\nu / Q_\nu, \quad \mathbf{Q}_\nu = \sum_{\mu \neq \nu} \omega_\mu \mathbf{p}_{t;\mu}. \tag{2.4}$$

Since the particle momenta are projected onto the measured reaction plane, which disperses around the true reaction plane, the average momenta is reduced: $\langle p_{x'}(y) \rangle < \langle p_x(y) \rangle$. We will obtain the analytical relation between these two quantities in Sec. 2.5 from our approach.

Ever since it was first introduced, the $\mathbf{Q}$ vector method has become the most commonly used tool for flow analysis in intermediate energy heavy ion collisions, and it remains valid for high energy heavy ion collisions. The limitation of this method is that one has to have momentum (or energy) measurements of each particle over a large solid angle, preferentially with particle identification. Eq. (2.3) can not be applied to measurements using calorimeters without particle separation and identification. The large popularity of this method is due to the following facts. Firstly, it is straightforward and easy to handle for experimentalists. Secondly, it decouples the transverse motion (p_t) from the longitudinal one (y), thus it is sensitive to the detailed azimuthal shapes. The latter enabled the authors to observe the collective motion in Ar on KCl collisions at 1.8 GeV/nucleon, which was not revealed by the standard sphericity tensor method.

2.2.2 Three dimensional sphericity

The standard sphericity tensor, or the 3-D sphericity method as we will call it later, was used in high energy physics for jets studies before it was introduced to heavy ion physics by two groups in 1982 [29, 37].

The standard sphericity matrix is defined as

$$S_{ij} \equiv \sum_{\nu=1}^{M} \omega_\nu p_{i;\nu} p_{j;\nu}, \tag{2.5}$$

where $i, j = x, y, z$ refer to a Cartesian coordinate system with the z-axis pointing to the beam direction, and ω_ν is a weighting factor, commonly chosen as $1/m$ so that S_{ij} is proportional to kinetic energy in the non-relativistic limit. Note that momenta are measured in the c.m.s. system. The matrix can be diagonalized:

$$S = \Lambda \begin{pmatrix} f_1 & 0 & 0 \\ 0 & f_2 & 0 \\ 0 & 0 & f_3 \end{pmatrix} \Lambda^\dagger, \tag{2.6}$$

where the eigenvalues $f_1 \leq f_2 \leq f_3$ are along the direction of the three major (symmetry) axes of an ellipsoid, and

$$\Lambda = R_z(\psi) R_y(\vartheta) R_z(\chi), \tag{2.7}$$

is a product of the orthogonal rotation matrices about fixed z, y, and z axes with angles χ, ϑ, and ψ respectively. Here (ϑ, ψ) are the polar and azimuthal angles associated with the largest eigenvalue f_3. Physically, ϑ corresponds to the angle of most rapid collective matter flow, while ψ is an estimate of the azimuthal angle of the reaction plane. It was realized by Danielewicz and Gyulassy [38] that the probability distributions $dw/d(f_2/f_1)d(f_3/f_2)$ and $dw/d\vartheta$ were distorted by Jacobian factors reflecting the phase space. If $M \to \infty$ this distortion can be neglected. For $M < 100$, which is the case for many collisions at intermediate energies, the distributions have to be corrected with Jacobian factors. Fig. 2.2, reproduced from Fig. 3(a) of Ref. [38], shows $dN/d\cos\vartheta$ for fixed $f_3/f_2 = 1.9$, $f_2/f_1 = 1.0$ at $\vartheta = 20°$ for different multiplicities M. Note, $dN/d\cos\vartheta = dN/\sin\vartheta d\vartheta \simeq dN/\vartheta d\vartheta$ for small ϑ.

The first experimental observation of the collective flow at the Bevalac was achieved by employing this method [21]. The distributions $dN/d\cos\vartheta$ from the data indeed showed similar structures as Fig. (2.2), which established the anisotropic event shapes. The idea of fitting the 3-D momentum distribution to an ellipsoid gives a clear physical picture of the 3-D global event shape. The capability of identifying spherical (isotropic), prolate ("cigar") or oblate ("pancake") shapes is unique among all the methods for flow analysis. Obviously $f_1 \simeq f_2 \simeq f_3$ represents isotropic events, $f_1 \simeq f_2 < f_3$ is prolate and $f_1 < f_2 \simeq f_3$ ($\vartheta \simeq 90°$) is oblate, the latter of which preferentially appears in very central collisions. But it requires momentum measurement into 4π solid angle. It also has the following disadvantages: (1) Event shapes for asymmetric collisions are not described well by this method, since the events may appear like a pear shape. (2) Since it always fits data with ellipsoids, the details of event shapes, namely the rapidity dependence of the azimuthal anisotropy, are lost in the analysis. (3) In high energy heavy ion collisions, the longitudinal expansion is much stronger than the transverse one (see Sec. 4.1.1). Thus the ellipsoids are prolate or "cigar" shaped even for head on collisions. The polar flow angle ϑ is very small, of the order of a few degrees, which diminishes the resolution of the reaction plane and the flow signal. To illustrate the latter point, consider that

$$\vartheta \simeq \arctan \frac{\langle p_x \rangle (y_{beam})}{p_z(y_{beam})}. \tag{2.8}$$

Taking an AGS beam momentum of 11.4 A·GeV/c, the value of $p_z(y_{beam})$ in c.m.s. is 2.3 GeV/c. Assuming $\langle p_x \rangle (y_{beam}) \simeq 0.1$ GeV/c, one gets $\vartheta \simeq 2.5°$.

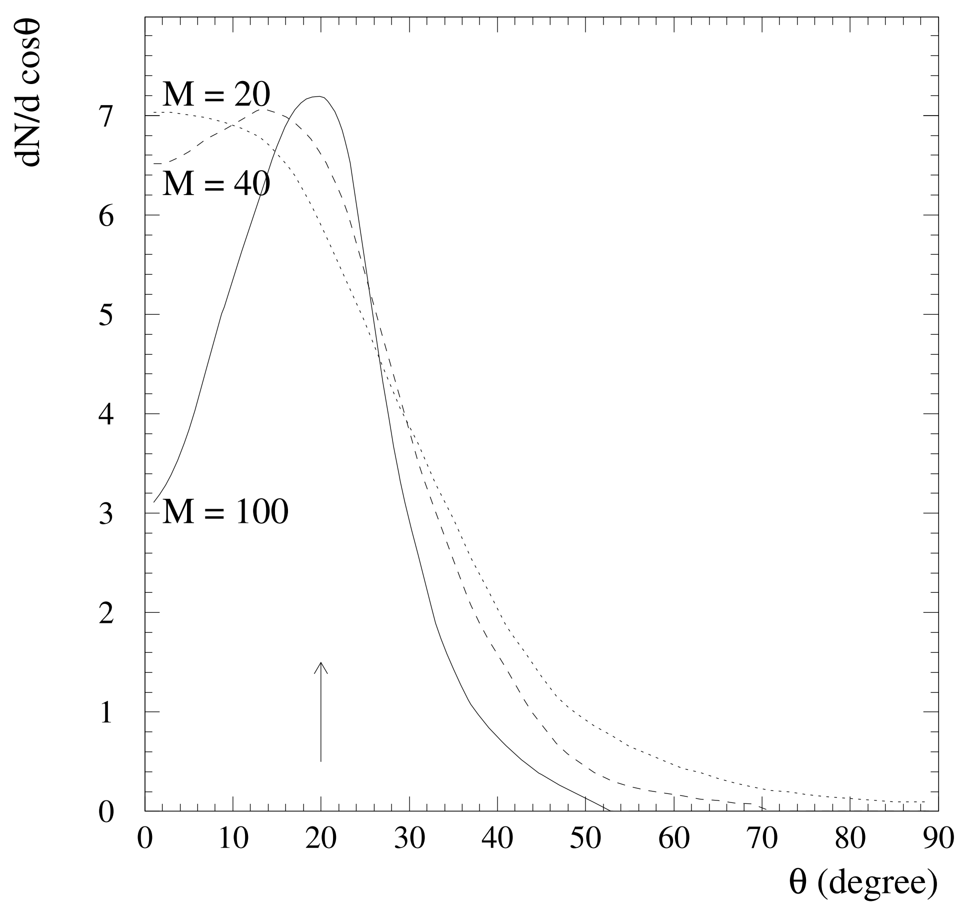

Figure 2.2: $dN/d\cos\vartheta$ plotted versus ϑ for "cigar" shape events with $f_3/f_2 = 1.9$ and $f_2/f_1 = 1.0$ oriented at $\vartheta = 20°$. The multiplicity dependence is illustrated. For the largest multiplicity, $M = 100$, the peak value is close to the intrinsic 20°, while the peaks are getting closer to zero for $M = 40$ and $M = 20$.

Note that as the incident energy increases, ϑ approaches zero, and $f_1, f_2 << f_3$. It was this observation that led Ollitrault to a reduction of the 3-D sphericity to 2-D sphericity [39].

2.2.3 Two dimensional sphericity

The idea here is to fit the transverse 2-D momentum distribution by an ellipse. The 2-D transverse sphericity tensor $S^\perp$ is simply the upper-left 2×2 matrix of (2.5),

$$S^\perp = \begin{pmatrix} \sum_{\nu=1}^{M} \omega_\nu p_{t;\nu}^2 \cos^2 \phi_\nu & \sum_{\nu=1}^{M} \omega_\nu p_{t;\nu}^2 \cos\phi_\nu \sin\phi_\nu \\ \sum_{\nu=1}^{M} \omega_\nu p_{t;\nu}^2 \cos\phi_\nu \sin\phi_\nu & \sum_{\nu=1}^{M} \omega_\nu p_{t;\nu}^2 \sin^2 \phi_\nu \end{pmatrix} \tag{2.9}$$

and can be parameterized with three parameters (ε, α and ψ) in the following way [39, 40]:

$$S^\perp = \frac{\varepsilon}{2} \begin{pmatrix} 1 + \alpha\cos 2\psi & \alpha \sin 2\psi \\ \alpha \sin 2\psi & 1 - \alpha \cos 2\psi \end{pmatrix}, \tag{2.10}$$

with

$$\varepsilon \equiv \mathrm{tr} S^\perp = f_1 + f_2, \tag{2.11}$$

$$\alpha \equiv \frac{f_1 - f_2}{f_1 + f_2}. \tag{2.12}$$

To obtain explicitly the eigenvalues f_1, f_2 and the rotation angle ψ, we solve the equation $\det(S^\perp - fI) = 0$, where I is the 2×2 unit matrix, which yields

$$\varepsilon = f_1 + f_2 = \sum_{\nu=1}^{M} \omega_\nu p_{t;\nu}^2, \tag{2.13}$$

$$\alpha\varepsilon = f_1 - f_2 = \sqrt{(\sum_{\nu=1}^{M} \omega_\nu p_{t;\nu}^2 \cos 2\phi_\nu)^2 + (\sum_{\nu=1}^{M} \omega_\nu p_{t;\nu}^2 \sin 2\phi_\nu)^2}, \tag{2.14}$$

and the azimuthal angle[4] is

$$2\psi = \arctan \frac{\sum_{\nu=1}^{M} \omega_\nu p_{t;\nu}^2 \sin 2\phi_\nu}{\sum_{\nu=1}^{M} \omega_\nu p_{t;\nu}^2 \cos 2\phi_\nu}. \tag{2.15}$$

[4]Normally $-\pi/2 \leq \arctan(y/x) \leq \pi/2$. Here one should take into account the signs of x and y components to get an angle covering 2π.

Eqs. (2.13-2.15) are easy to obtain but the author [39, 40] did not derive them explicitly. Nevertheless, they are important in two ways. They simplify data analysis procedure from an event-by-event diagonalization to a simple summation, and they show similarity with the directivity method, which led me to the idea of generalization of those methods to Fourier expansion (Sec. 2.3.1). The limitation of this method is that it is sensitive only to the elliptical component of azimuthal distributions.

2.2.4 Thrust

Thrust has been used in analyzing high energy electron-positron collisions [44]. It is one of the earliest methods of global shape analysis for heavy ion collisions, and was introduced by Kapusta and Strottman in 1981 [45]. The *directed thrust* is defined as

$$\tilde{T}(\hat{\mathbf{n}}) = \sum_{\nu} |\mathbf{p}_{\nu} \cdot \hat{\mathbf{n}}| / \sum_{\nu} |\mathbf{p}_{\nu}|, \tag{2.16}$$

where $\hat{\mathbf{n}}$ is a unit vector pointing in any direction, and $\mathbf{p}_{\nu}$ is the momentum of each particle in the c.m.s. $\tilde{T}(\hat{\mathbf{n}})$ is interpreted as directed momentum flow in the direction of $\hat{\mathbf{n}}$, and satisfies $0 \leq \tilde{T}(\hat{\mathbf{n}}) \leq 1$. The *thrust* is then defined as the maximum value of the *directed thrust* when $\hat{\mathbf{n}}$ is varied over all directions.

$$T = \max_{\hat{\mathbf{n}}} \tilde{T}(\hat{\mathbf{n}}). \tag{2.17}$$

In analogy to the 3-D sphericity, this method requires momentum measurements over a 4π solid angle. The physical meaning is also similar to that of 3-D sphericity; $\hat{\mathbf{n}}_{\text{max}}$ reflects the direction of the most rapid collective matter flow, which is analogous to the maximum axis of the ellipsoid defined as the maximum eigenvalue f_3 (ϑ and ψ) in 3-D sphericity. For an event in which an infinite number of particles are emitted isotropically (neglecting fluctuations), one has $T = 1/2$ and $f_1 = f_2 = f_3$. For an extremely long "cigar" event in which all particles come out back to back along a common axis, one has $T = 1$ and only f_3 is non-zero.

In electron-positron collisions, where multiplicity is low and most of the emitted particles form jets, it is relatively easy to find the maximum axis. However, in heavy ion collisions where the multiplicity is high and the asymmetry is relatively small, one has to calculate the direct thrust at all angles in 4π to find it. For this reason it was not extensively used in flow analysis. The advantage of thrust over its counterpart 3-D sphericity is that it involves a summation over the momenta other than the squares of the momenta. This, however, can be implemented easily into 3-D sphericity by replacing a particle's $p_{x;\nu}$, $p_{y;\nu}$ and $p_{z;\nu}$ with $\sqrt{p_\nu}\sin\theta_\nu\cos\phi_\nu$, $\sqrt{p_\nu}\sin\theta_\nu\sin\phi_\nu$, and $\sqrt{p_\nu}\cos\theta_\nu$, respectively. In this case the direction of $\hat{\mathbf{n}}_{\max}$ coincides with that of f_3. The advantages of the linear summation is discussed in Sec. 2.3.1.

2.2.5 Azimuthal two particle correlations

An azimuthal two particle correlation function

$$C(\Delta\phi) = \frac{P_{cor}(\Delta\phi)}{P_{uncor}(\Delta\phi)}, \tag{2.18}$$

where $\Delta\phi$ is the azimuthal angle between two particles, was proposed in [41] to study transverse flow. Here $P_{uncor}(\Delta\phi)$ is the distribution generated by "event mixing", which should be flat in principle but may be distorted by the detector's asymmetric azimuthal efficiencies. $P_{cor}(\Delta\phi)$ is the observed pair distribution in the same events, and it is the convoluted integration of two single particle azimuthal distributions. For a given single particle azimuthal distribution $r(\phi) = dM/d\phi$ in a certain event class, one can get a general expression (this is not done in the literature),

$$\begin{aligned} C(\Delta\phi) &\propto \int d\phi\, d\phi'\, r(\phi)\, r(\phi')(1+\lambda(\Delta\phi))\,\delta(\Delta\phi - \phi' + \phi) \\ &= \int d\phi\, r(\phi)\, r(\phi+\Delta\phi)(1+\lambda(\Delta\phi)), \end{aligned} \tag{2.19}$$

where $1+\lambda(\phi)$ is the intrinsic two particle azimuthal correlation function,

$$1+\lambda(\Delta\phi) = \frac{d^2w/d\phi\, d\phi'}{(dw/d\phi)\,(dw/d\phi')}. \tag{2.20}$$

This has to be calculated on an event-by-event basis, which is difficult if the multiplicity M in each event is low. But since decays and Bose-Einstein correlation are the major causes of such an intrinsic two particle azimuthal correlation, we do not expect $\lambda(\Delta\phi)$ to be large, except around $\Delta\phi = 0$,[5] and assume $\lambda(\Delta\phi) = 0$. In this case any non-flat distribution in $r(\phi)$ will result a non-flat distribution in $P_{cor}(\Delta\phi)$. To test its sensitivity, let us consider a simple azimuthal harmonic distribution $r(\phi) \propto 1 + 2v_1\cos\phi$, which is the most commonly used form by previous analyses. Substituting this distribution into Eq. (2.19) one simply gets

$$C(\Delta\phi) = 1 + 2v_1^2\cos(\Delta\phi). \tag{2.21}$$

[5] At RHIC energy the presence of 2-jets may introduce correlations at $\Delta\phi = \pi$.

The correlation function $C(\Delta\phi)$ obtained from experiments can be fitted with the distribution 2.21 to extract the anisotropy parameter v_1. If $C(\Delta\phi)$ shows an abnormally large peak at $\Delta\phi = 0$ as expected from the intrinsic two particle correlation, one should leave out the region around the abnormal peak position before fitting.

If the intrinsic correlation is not unity over a wide range of $\Delta\phi$, one can adopt the so called "high-order" two particle correlation as defined by [42]

$$\Delta\phi_n = (\prod^{K} \Delta\phi)^{1/K}, \quad K = \frac{1}{2}n(n-1), \tag{2.22}$$

where the product runs over all K azimuthal separations $\Delta\phi$ of all possible pairs from n particles ($n \leq M$). Obviously $\Delta\phi_2$ coincides with $\Delta\phi$. The higher the order n, the more sensitive is the function $C_n(\Delta\phi_n)$ to correlations from collective motion (other than intrinsic pair correlation).

There are two problems that limit the use of the two particle correlation method. The first problem is the sensitivity. One always has $2v_1^2 < 2v_1$ since $v_1 < 1$, which means that the signal is diminished. In case where $v_1 \ll 1$, it is experimentally difficult to measure $2v_1^2$. For example, if one take $2v_1 = 0.1$, which is still a large azimuthal anisotropy, one gets the value of 0.005 for $2v_1^2$, with a large reduction factor of 20. The second problem is that the azimuthal distribution $r(\phi)$ which we want to explore is unknown beforehand. These two problems are solved in the following new approach. The first one is discussed in Sec. 2.6, and second one in Sec. 2.3.2.

Nevertheless, this method has proven to be effective for flow analysis in intermediate energy heavy ion collisions. This is because the anisotropy parameter v_1 is reasonably large.[6] Comparing with other methods, it is also free from uncertainties associated with reaction plane determination. It is also not affected by detector defects (if they are not too large) because of the normalization to $P_{uncor}(\Delta\phi)$ from mixed events.

2.3 Fourier Expansion of Azimuthal Distribution

2.3.1 General idea

Since the 2-D sphericity analysis introduced by Ollitrault [39] is intended to be used for ultra-relativistic heavy ion collisions, it became a natural choice

[6]Typically, $2v_1 \sim 0.5$ in the intermediate energy heavy ion collisions.

for our flow studies to begin with. The similarity between the 2-D sphericity and the directivity was soon noticed. If one replaces $p^2_{t;\nu}$ with $p_{t;\nu}$, $2\phi_\nu$ with ϕ_ν, and 2ψ with ψ, Eqs. (2.13-2.15) are equivalent to the ones used in the directivity method, with $\varepsilon\alpha = Q$ being the length of $\mathbf{Q}$ defined in Eq. (2.1), while ψ is the same measure of the reaction plane angle. It does not matter in principle whatever one takes for the quantity $p_{t;\nu}$, or $p^2_{t;\nu}$, or even $\epsilon_{t;\nu}$ in our experiment. But taking the linear term $p_{t;\nu}$ or $\epsilon_{t;\nu}$ is advantageous in two respects. Firstly, the summation over particles is equivalent to summation over detector cells. This is important in using calorimeters without sufficient granularity to measure the energy deposition for individual particles, which is increasingly difficult in high multiplicity environments with increasing beam energy. Secondly, the contribution of a cluster (d, ^{3}He, etc.) is equivalent to that of its constituent nucleons. This is important when the production rates for clusters are high, which is the case for low and intermediate energy, or for "bounce-off" (spectators) flow at all energies.

We generalized Eqs. (2.13-2.15) by replacing $p^2_{t;\nu}$ with $\epsilon_{t;\nu}$ (or any other linear quantities), $2\phi_\nu$ with $n\phi_\nu$, and 2ψ with $n\psi$. As first pointed out by Voloshin, the summation of the n-th term is essentially the Fourier expansion coefficient of the n-th harmonic [46].

2.3.2 Fourier expansion

The methods discussed above can be categorized into two approaches. One is to detect 3-D event shapes directly, as done in 3-D sphericity and thrust methods. The other is a two dimensional analysis, exploring the two dimensional shapes through p_t distributions as in directivity and 2-D sphericity, or by azimuthal correlations as in azimuthal two particle correlation. Our approach belongs to the latter. For an azimuthal analysis, it is convenient to adopt a cylindrical coordinate system. One can use p_z, y or η as the longitudinal variable, p_t, ϵ_t or multiplicity as transverse quantities, and ϕ as the azimuthal angle. With particle identification and momentum measurement, the set (y, p_t, ϕ) contains the most complete information, and should be used preferentially. For the present analysis we use (η, ϵ_t, ϕ), which contains the same azimuthal angle as the former.

In our approach, we divide the whole y (or η) acceptance into a few intervals, and perform Fourier analyses in each interval. Fourier coefficients of different harmonics reflect the different type of anisotropy in the particle azimuthal distribution. To get more details of the event shapes one would like to divide the whole y (or η) acceptance into as many windows as possible. The limitation comes from the finite multiplicity fluctuations. The multiplicity in each window should be sufficiently large to keep the fluctuation under control (see Sec. 2.3.3).

The azimuthal distribution function of the quantity under study is denoted by $r(\phi)$, *e.g.*, $r(\phi) = dP_T(\phi)/d\phi$, $r(\phi) = dE_T(\phi)/d\phi$, or $r(\phi) = dM(\phi)/d\phi$. The function $r(\phi)$ can be constructed from experimental data event-by-event. Since $r(\phi)$ is a periodic function it can be written in form of a Fourier expansion:

$$r(\phi) = \frac{x_0}{2\pi} + \frac{1}{\pi}\sum_{n=1}^{\infty}[x_n\cos(n\phi) + y_n\sin(n\phi)]. \tag{2.23}$$

The Fourier coefficients x_n and y_n are the integrals of $r(\phi)$ with weights proportional to $\cos(n\phi)$ or $\sin(n\phi)$. Since there is only a finite number of particles in each event, the integrals become simple sums over particles found in the appropriate y-window:

$$x_n = \int_0^{2\pi} d\phi\, r(\phi)\cos(n\phi) = \sum_\nu r_\nu\cos(n\phi_\nu), \tag{2.24}$$

$$y_n = \int_0^{2\pi} d\phi\, r(\phi)\sin(n\phi) = \sum_\nu r_\nu\sin(n\phi_\nu), \tag{2.25}$$

where ν runs over all particles in the y-window, r_ν and ϕ_ν are the values of the observable r and the azimuthal angle of the ν-th particle.[7] Each non-zero pair of x_n and y_n indicates the presence of a multiple component of order n in the flow pattern, which is characterized by a magnitude v_n and an angle [8] ψ_n,

$$v_n = \frac{\sqrt{x_n^2 + y_n^2}}{x_0}, \tag{2.26}$$

$$\psi_n = \frac{1}{n}\arctan\frac{y_n}{x_n}. \tag{2.27}$$

Note that the flow amplitude v_n is normalized to $x_0 = M\langle r\rangle$ to make it easier to compare the magnitudes of flow in different rapidity windows or centrality bins, or between different experiments. The following discussion remains almost the same without this normalization (see *e.g.* Ref.[46]).

If ϕ is defined relative to the reaction plane angle, $r(\phi)$ is an even function. All terms in y_n would be zero, and

$$r(\phi) = \frac{x_0}{2\pi}[1 + \sum_{n=1}^{\infty} 2v_n\cos(n\phi)], \tag{2.28}$$

[7] One can choose r_ν to be $p_{t;\nu}$, $\epsilon_{t;\nu}$, or simply 1 in case of multiplicity, while ϕ_ν remains the same no matter what transverse variables are used.

[8] Taking into account the signs of x_n and y_n, one gets $0 \leq 2\psi_n < 2\pi$.

The distribution (2.28) can be used to calculate the azimuthal two particle correlation function $C(\Delta\phi)$ from (2.19),

$$C(\Delta\phi) = 1 + \sum_{n=1}^{\infty} 2v_n^2 \cos(n\Delta\phi), \tag{2.29}$$

which is a generalized expression of (2.21) including the higher moments. Since ψ_r is canceled out event-by-event in calculating $\Delta\phi$, Eq. (2.29) is not affected by the determination of reaction plane. Knowing the measured distribution $C(\Delta\phi)$, one can calculate the Fourier coefficients directly from Eq. (2.29),

$$v_n = \sqrt{\frac{1}{2}\int_0^{2\pi} d\Delta\phi\, C(\Delta\phi)\cos(n\Delta\phi)}. \tag{2.30}$$

This is exactly the solution to the second problem raised at the end Sec. 2.2.5. With the concept of Fourier expansion, the azimuthal two particle correlation $C(\Delta\phi)$ is given a clearer meaning and an analytical solution. But the first problem (Sec. 2.2.5) is not solved, namely it is difficult to detect weak flow signals with this method.

2.3.3 Physical meaning

Let us now examine the meaning of the Fourier coefficients. Without any flow and neglecting fluctuations, the azimuthal distribution is flat and $r(\phi)$ is a constant as shown in Fig. 2.3(a). This corresponds to a circular distribution in 2-D (Fig. 2.3(b)). All Fourier coefficients would be zero except for $x_0 = \sum_\nu r_\nu = M\langle r\rangle$. Note that if one takes the variable r_ν as the transverse energy of individual particles, ϵ_ν, one would get $x_0 = \sum_\nu \epsilon_\nu = E_T$.

If flow is present, $r(\phi)$ is no longer a constant, but can be any function as illustrated in Fig. 2.3(c), and the shape of the distribution is no longer a circle centered at the origin. Instead, it can be a complicated distribution shown in Fig. 2.3(d) as an example. Note that even in this most general case, symmetry with respect to the reaction plane (indicated by dotted-dashed lines in the figures) should be preserved. The azimuthal distribution $r(\phi)$ may contain contribution from any harmonic term. A few harmonic terms are discussed below when they are present alone.

The first harmonic coefficients correspond to an overall shift of the distribution in the transverse plane, with the flow amplitude v_1 and flow angle ψ_1 (Fig. 2.4(a, b)). Such flow is called directed *sideward flow*. If $r(\phi)$ is the transverse momentum distribution, the coefficients x_1 and y_1 are the x and y

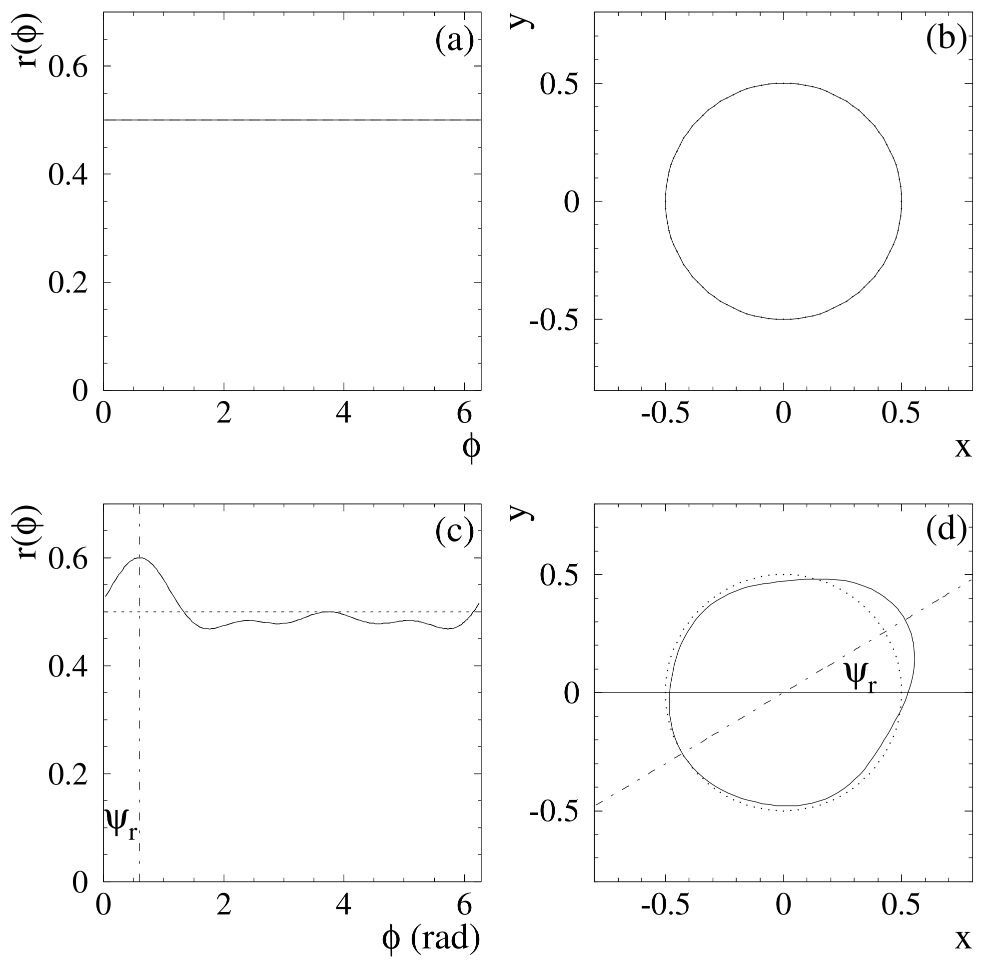

Figure 2.3: The azimuthal distributions (a, c) and the corresponding 2-D polar distributions (b, d) without or with flow. Dotted line and circle in (c, d) are the solid line and circle in (a, b) for comparisons.

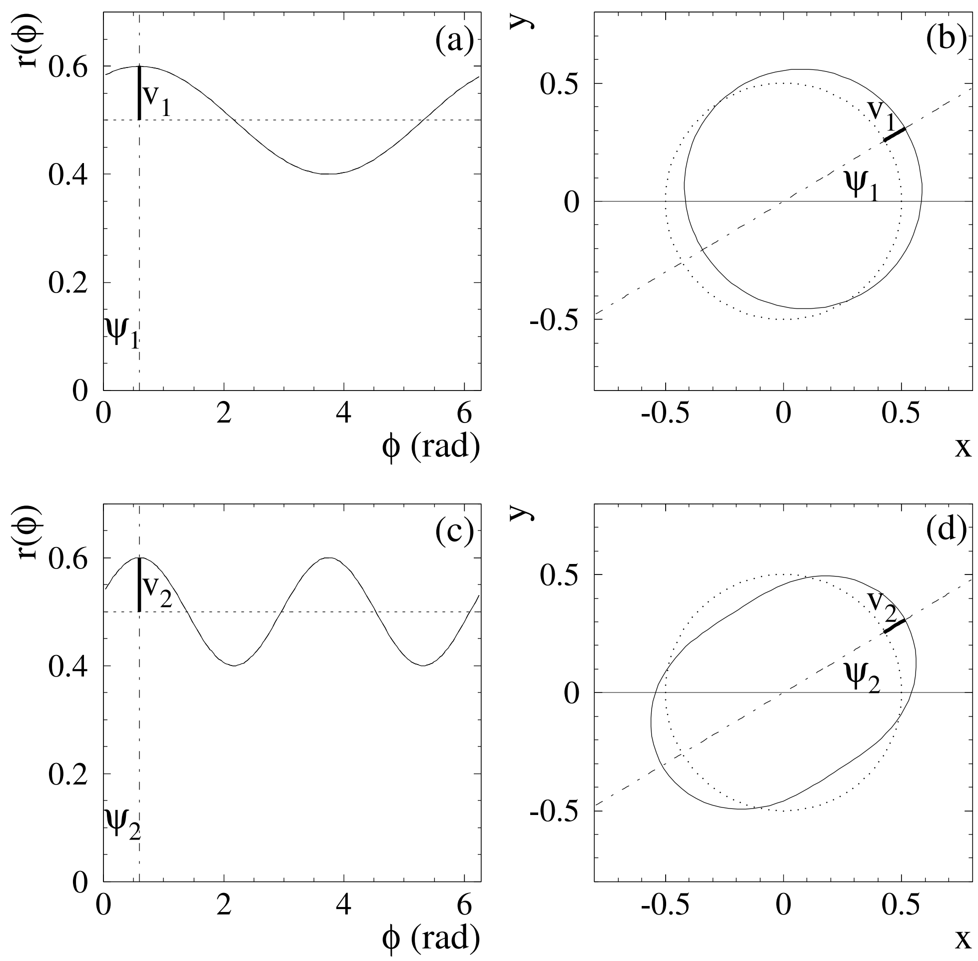

Figure 2.4: The azimuthal distributions (a, c) and polar distributions (b, d) for the first (a, b) and the second (c, d) harmonic. Dotted line and circle from Fig. 2.3(a, b) are plotted for comparisons.

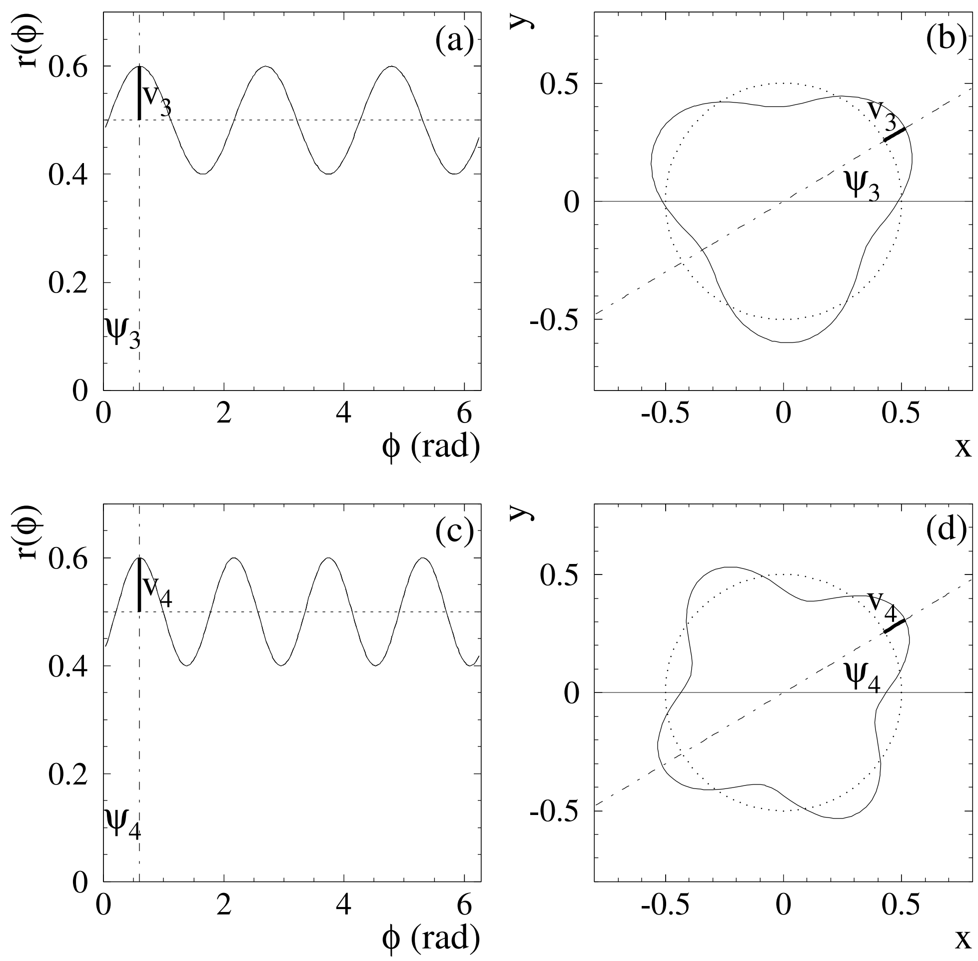

Figure 2.5: The azimuthal distributions (a, c) and polar distributions (b, d) for the third (a, b) and the forth (c, d) harmonic. Dotted line and circle from Fig. 2.3(a, b) are plotted for comparisons.

components of the total transverse momentum ($P_X = \sum_\nu p_{x;\nu}$, $P_Y = \sum_\nu p_{y;\nu}$) of the particles produced in the rapidity window. Taking $\omega_\nu = 1$, the vector $\mathbf{Q}$ in Eq. (2.1) coincides with with vector $P_T \mathbf{v}_1 \equiv P_T(v_1, \psi_1)$, where $P_T = \sum_\nu p_{t;\nu}$. In the case of negligible fluctuations the direction of flow coincides with the reaction plane angle, *i. e.*, $\psi_1 = \psi_r$ (repulsive flow), or points in the opposite direction, *i. e.*, $\psi_1 = \psi_r + \pi$ (attractive flow) for a forward rapidity interval, and is reversed for a backward rapidity interval.

If the azimuthal distribution can be described by an ellipse, as shown in Fig. 2.4(c,d), then the coefficient v_2 is proportional to the difference between the major and minor axes f_1 and f_2. If we choose r_ν to be $\omega_\nu p_{t;\nu}^2$, we find that our coefficient v_2 is equivalent to the 2-D sphericity parameter, *i. e.*, $v_2 = \dfrac{f_1 - f_2}{f_1 + f_2} = \alpha$ following Eqs. (2.12-2.14). Also (2.15) is identical with (2.27) for $n = 2$, giving the same orientation of the major axis, defined by the angle ψ_2. Due to symmetry with respect to the reaction plane, ψ_2 is either in the reaction plane (ψ_r or $\psi_r + \pi$ as in Fig. 2.4), or perpendicular to it ($\psi_r + \dfrac{\pi}{2}$ or $\psi_r + \dfrac{3\pi}{2}$). The latter has been called *squeeze-out* [47] flow, and was observed in the mid-rapidity window at lower beam energies.

The coefficient v_3 is non-zero if the azimuthal distribution has a sort of triangular shape (Fig. 2.5(a, b)). This might happen for asymmetric nuclear collisions, where it represents the asymmetry of flow due to the different sizes of the colliding nuclei. Even for a symmetric system, it might happen in a rapidity window not centered around mid-rapidity. The symmetry constrains the azimuthal flow angle ψ_3 to be $\psi_r - m\dfrac{2\pi}{3}$ or $\psi_r - m\dfrac{2\pi}{3} + \dfrac{\pi}{3}$.

The shape of the forth moment is shown in Fig. 2.5(c, d). The amplitude v_4 could be non-zero, *e. g.*, for y-windows close to the c.m.s., where both squeeze-out and sideward flow can exist and form a superposition of v_2 perpendicular to two back-to-back v_1 components. The azimuthal flow angle ψ_4 is equal to one of $\psi_r - m\dfrac{\pi}{2}$ if the origin of the rectangle-type flow is the one mentioned above. But $\psi_4 = \psi_r + \dfrac{\pi}{4}$ can not be ruled out from symmetry arguments. Indeed a hydrodynamical calculation shows an azimuthal distribution with $\psi_4 = \psi_r + \dfrac{\pi}{4}$ (see Sec. 5.2).

To summarize, each coefficient v_n is the magnitude of the anisotropy in the n-th harmonic of the azimuthal distribution, and the orientation ψ_n is related to the reaction plane angle in the following way:

$$\psi_n = \psi_r - m\frac{2\pi}{n} + l\frac{\pi}{n}, \tag{2.31}$$

where $l = 0, 1$, which can be determined from the data, and m is a integer to reduce the flow angle into a meaningful range $0 \leq \psi_n < \dfrac{2\pi}{n}$.

2.4 Finite Multiplicity Fluctuations

Mathematically, the Fourier expansion can only be applied to periodic continuous functions. But in reality, only finite numbers of particles are emitted in each collision. This introduces some ambiguity in detecting the anisotropy on an event-by-event basis. Even if the distribution is azimuthally isotropic, statistical fluctuations can lead to non-zero coefficients v_n. On the other hand, statistical analysis enables us to suppress the fluctuations and extract the real signal from the probability distribution of v_n. In this and the following sections we derive these distributions and show how to extract the underlying anisotropy parameters.

We first present three assumptions to simplify the problem. First, since two particle correlations are experimentally found to be weak [48], all particles in the same event and in the same y-window can be treated as being independent. Second, although we study finite multiplicity fluctuations, we consider the case where the total number of particles in the selected window is relatively large ($M \gg 1$). Third, we can classify events according to their centrality or the impact parameter, and we assume to have the same magnitude of flow and the same multiplicities for events in the same class. Since the impact parameter is strongly correlated with global variables (E_T, M, and zero degree energy, etc.) in model calculations, one can select events of the same centrality experimentally. The justification for these assumptions will be discussed further in Sec. 2.7.

Under these assumptions, in the absence of flow, the probability distribution of the vectors (v_n, ψ_n) has to be Gaussian due to the central limit theorem (Appendix A):

$$\frac{d^2w}{v_n dv_n d(n\psi_n)} = \frac{1}{2\pi\sigma_n^2}\exp(-\frac{v_n^2}{2\sigma_n^2}), \tag{2.32}$$

with the peak of the distribution centered at the origin ($v_n = 0$). The variance of the distribution is the same for any n-th moment:

$$\sigma_n^2 = \frac{M\langle r^2\rangle\langle\cos^2(n\phi)\rangle}{(M\langle r\rangle)^2} = \frac{\langle r^2\rangle}{2M\langle r\rangle^2} \equiv \sigma^2, \tag{2.33}$$

where M is the number of particles in the window under study. We see that if we have $M \to \infty$, then $\sigma \to 0$, and the Gaussian distribution becomes a δ-function, and we get $v_n = 0$ event-by-event.

With the appearance of flow in the n-th harmonic, the above δ-function is shifted to $(\tilde{v}_n, n\tilde{\psi}_n)$, where $n\tilde{\psi}_n$ is $n\psi_r$ or $n\psi_r + \pi$ (see Eq. (2.31)).[9] With finite M, we again have a Gaussian distribution with centroids being at the position of the shifted δ-function, $(\tilde{v}_n, n\psi_r)$:

$$\frac{d^2 w}{v_n dv_n d(n\psi_n - n\psi_r)} = \frac{1}{2\pi\sigma_n^2}\exp(-\frac{\tilde{v}_n^2 + v_n^2 - 2\tilde{v}_n v_n \cos(n\psi_n - n\psi_r)}{2\sigma_n^2}), \quad (2.34)$$

where $\tilde{v}_n$ should be a constant in the same event class. When the flow amplitudes are small $\tilde{v}_n \ll 1$, one has the same σ_n for all harmonics because $\langle\cos^2(n\phi)\rangle = 1/2$. For the rest of the discussion, including data analysis, we assume $\sigma_n = \sigma$ (see discussion in Sec. 2.7).

The integration over orientation $n\psi = n\psi_n - n\psi_r$ gives the probability distribution of v_n:

$$\begin{aligned} \frac{dw}{v_n\, dv_n} &= \frac{1}{2\pi\sigma^2}\int_0^{2\pi} d(n\psi)\exp(-\frac{\tilde{v}_n^2 + v_n^2 - 2\tilde{v}_n v_n \cos(n\psi)}{2\sigma^2}) \\ &= \frac{1}{\sigma^2}\exp(-\frac{\tilde{v}_n^2 + v_n^2}{2\sigma^2}) I_0(\frac{\tilde{v}_n v_n}{\sigma^2}), \end{aligned} \quad (2.35)$$

where I_0 is the modified Bessel function (Appendix B). The shape of the distribution (2.35) for a few values of the parameters is shown in Fig. 2.6, where we plot $dw/\chi_n d\chi_n$ using the notation $\chi_n \equiv v_n/\sigma$ and $\tilde{\chi}_n \equiv \tilde{v}_n/\sigma$. The extrema are defined by the solution of the equation (see the property of Bessel function in Appendix B)

$$\tilde{v}_n\, I_1(\frac{v_n\tilde{v}_n}{\sigma^2}) - v_n\, I_0(\frac{v_n\tilde{v}_n}{\sigma^2}) = 0. \quad (2.36)$$

It follows from (2.36) that the distribution (2.35) has a local minimum at $v_n = 0$ if $\tilde{v}_n/\sigma > \sqrt{2}$ (see proof in Appendix B). Thus, the observation of such a minimum in the data is a sufficient condition for the appearance of anisotropic flow. Such a minimum is not required for the extraction of $\tilde{v}_n$ and σ by fitting the form (2.35) to data.

The functional form (2.35) was derived almost a decade ago for the distribution of polar flow angles extracted from the 3-D sphericity matrix [43].

[9] For simplicity we choose $n\tilde{\psi}_n = n\psi_r$ for the rest of the discussion. An angle π can be inserted whenever needed.

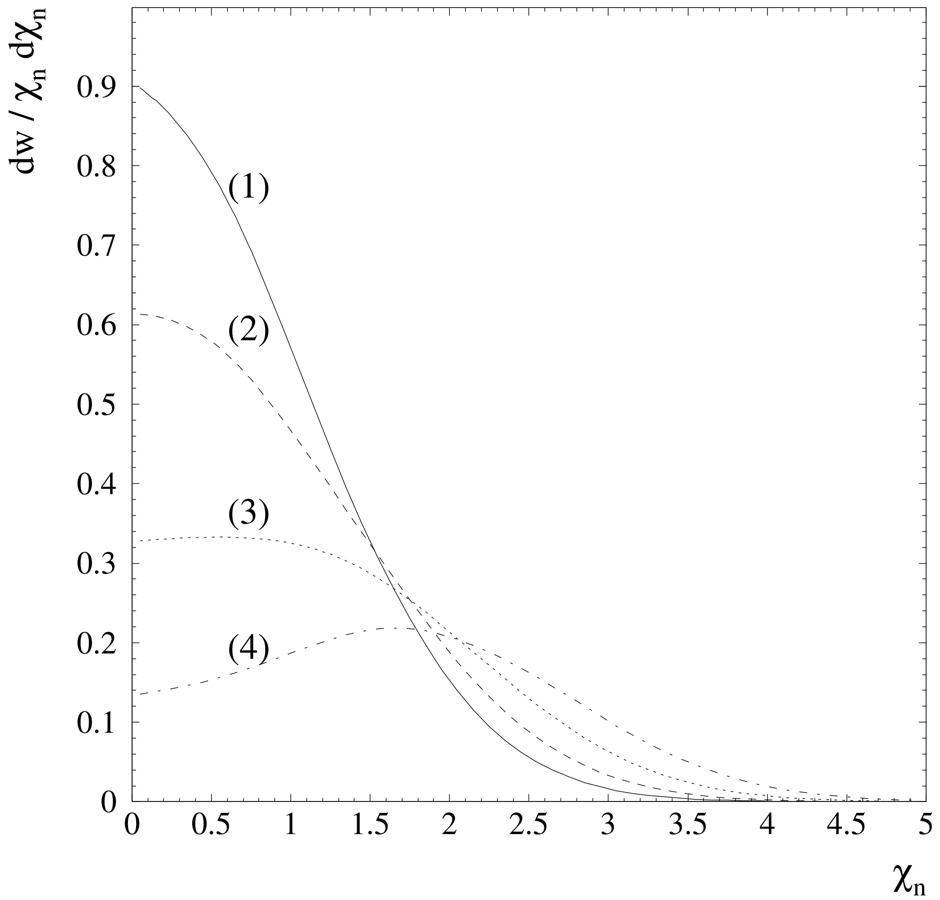

Figure 2.6: The distribution $dw/\chi_n d\chi_n$ from Eq.(2.35) using $\chi_n = v_n/\sigma$ for different values of $\tilde{\chi_n} = \tilde{v}_n/\sigma$. The curves marked by 1, 2, 3, and 4 correspond to $\tilde{\chi_n} = 0.5$, 1.0, 1.5, and 2.0, respectively.

Recently a similar study was done for the 2-D sphericity [39, 40]. Here we want to emphasize that with the same fluctuation parameter, σ, one would expect more stable and sensitive results by fitting simultaneously all $dw/v_n dv_n$ distributions with $k+1$ free parameters $\tilde{v}_n$ ($n = 1, 2, ..., k$) and σ. The number of anisotropy parameters k depends on the actual azimuthal distribution. This fitting procedure is crucial for a successful data analysis (see Sec. 4.3.3). Another interesting point is that, if we treat σ as a free fit parameter in data analysis on one hand, and calculate it from (2.33) on the other hand, we can compare these two and get information on dynamical fluctuations if they deviate from the statistical ones. This will be discussed in Sec. 4.3.5.

After discussion of the fluctuations, we now address the meaning of the anisotropy parameter $\tilde{v}_n$. Since it is independent of the fluctuations, we neglect the fluctuation ($M \to \infty$) to make the calculation easier. Also for simplicity, we assume that the orientation of the anisotropy is along the x-axis. Following the definitions in (2.24) and (2.26) we get,

$$\tilde{v}_n = v_n = \frac{x_n}{x_0} = \frac{M\langle r\cos(n\phi)\rangle}{M\langle r\rangle} = \frac{\langle r\cos(n\phi)\rangle}{\langle r\rangle}. \tag{2.37}$$

If r is chosen as transverse momentum, p_t, we get $\tilde{v}_n = \dfrac{\langle p_t\cos(n\phi)\rangle}{\langle p_t\rangle}$, and $\tilde{v}_1 = \dfrac{\langle p_x\rangle}{\langle p_t\rangle}$, where $\langle p_x\rangle$ is the mean transverse momentum in the direction of the true reaction plane (x-axis).

The combination of the anisotropy parameter and the fluctuation parameter determines the experimental sensitivity to the flow signal. From Eqs. (2.37) and (2.33), we have the combined parameter

$$\tilde{\chi}_n \equiv \frac{\tilde{v}_n}{\sigma} = \frac{\sqrt{2M}\langle r\cos(n\phi)\rangle}{\sqrt{\langle r^2\rangle}}. \tag{2.38}$$

We see that the rapidity windows must have a reasonably large multiplicity, M, to ensure that $\tilde{\chi}_n$ is not too small. Otherwise the distribution (2.35) would look the same as a Gaussian, and the fit will not produce reliable coefficients (see Fig. 2.6). The "relatively narrow" rapidity windows mentioned previously (Sec. 2.3.2) should be chosen experimentally with this consideration in mind.

2.5 Dispersion of the Measured Reaction Plane

Experimentally, the reaction plane can be inferred from the flow angle ψ_n on an event-by-event basis. To evaluate the accuracy of the procedure one should consider the distribution of $n\psi \equiv n\psi_n - n\psi_r$ by integrating over v_n in (2.34):

$$\begin{aligned}\frac{dw}{d(n\psi)} &= \int \frac{v_n dv_n}{2\pi\sigma^2} \exp(-\frac{\tilde{v}_n^2 + v_n^2 - 2\tilde{v}_n v_n \cos(n\psi)}{2\sigma^2}) \qquad (2.39)\\ &= \frac{1}{2\pi}[\exp(-\frac{\tilde{v}_n^2}{2\sigma^2}) + \frac{\tilde{v}_n \cos(n\psi)\sqrt{\pi}}{\sigma\sqrt{2}} \exp(-\frac{\tilde{v}_n^2 \sin^2(n\psi)}{2\sigma^2})(1 + \mathrm{erf}(\frac{\tilde{v}_n \cos(n\psi)}{\sigma\sqrt{2}}))].\end{aligned}$$

At the first look, it appears from (2.39) that $\tilde{\chi}_n = \tilde{v}_n/\sigma$ seems to be the only parameter to determine the dispersion of the reaction plane. The larger the $\tilde{\chi}_n$, the narrower the distribution, as shown in Fig. 2.7. After a second thought, we realize that v_n also affect the dispersion in the same way[10]. If one selects events with v_n larger than a certain value, one can go beyond the limit set by Eq. (2.39) and get a better estimate of the reaction plane. For events within a narrow bin $(v_n, v_n + \Delta v_n)$ we get

$$\frac{dw}{d(n\psi)} = \frac{v_n \Delta v_n}{2\pi\sigma^2} \exp(-\frac{\tilde{v}_n^2 + v_n^2 - 2\tilde{v}_n v_n \cos(n\psi)}{2\sigma^2}). \qquad (2.40)$$

Any n-th harmonic can be used to infer the reaction plane. Which one gives the best result? For the same magnitude of parameters $\tilde{v}_n$, one expects the same dispersion $r.m.s.[n(\psi_n - \psi_r)]$ for all harmonics, and a better resolution $r.m.s.(\psi_n - \psi_r)$ for a higher harmonic. However, for a single value ψ_n, there are $2n$ possible angles for ψ_r (see Eq. (2.31)), and there is an ambiguity in the determination of the reaction plane. In what follows, we only take the reaction plane angle measured by the first harmonic, ψ_1, and even there, there is ambiguity by π which is only solved by definition.

It is convenient to characterize the resolution of the reaction plane $dw/d\psi = dw/d(\psi_1 - \psi_r)$ by a value of $\langle \cos\psi \rangle$,

$$\begin{aligned}\langle \cos\psi \rangle &= \int d\psi \int \frac{v_1 dv_1}{2\pi\sigma^2} \cos\psi \, \exp(-\frac{\tilde{v}_1^2 + v_1^2 - 2\tilde{v}_1 v_1 \cos\psi}{2\sigma^2}) \qquad (2.41)\\ &= \frac{\sqrt{\pi}}{2\sqrt{2}} \frac{\tilde{v}_1}{\sigma} \exp(-\frac{\tilde{v}_1^2}{2\sigma^2})\, {}_1F_1(3/2; 2; \frac{\tilde{v}_1^2}{2\sigma^2}),\end{aligned}$$

where ${}_1F_1(\alpha; \beta; \gamma)$ is a confluent hypergeometric function. The behavior of $\langle \cos\psi \rangle$ and $r.m.s(\psi)$ as a function of $\tilde{\chi}_1 = \tilde{v}_1/\sigma$ is shown in Fig. 2.8.

We now pursue the optimal way to measure ψ_r by combining ψ_1 in all (pseudo)rapidity windows.[11] We begin with two windows a and b with param-

[10] Note, v_n and $\tilde{v}_n$ are in a symmetric position in (2.34)

[11] This is based on the initial idea and work done by Cleland, and Voloshin.

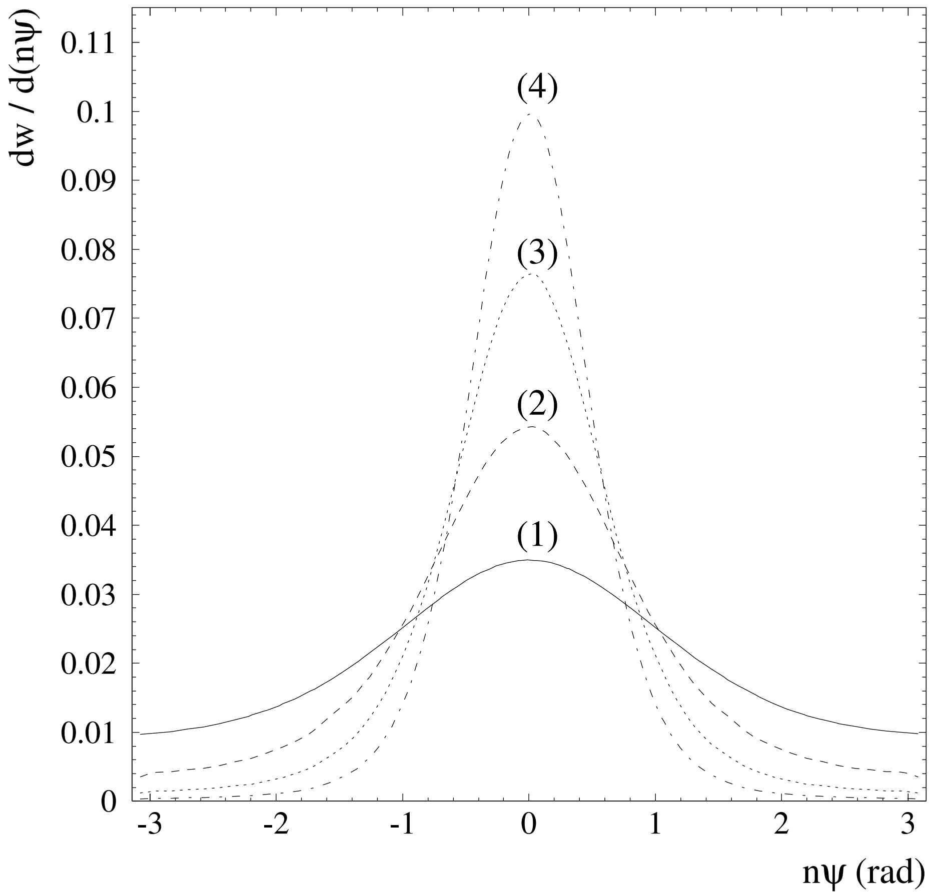

Figure 2.7: The distribution $dw/d(n\psi)$ from Eq. (2.39) ($n\psi = n\psi_n - n\psi_r$) for different values of $\tilde{\chi_n} = \tilde{v}_n/\sigma$. The curves marked by 1, 2, 3, and 4 correspond to $\tilde{\chi_n} = 0.5$, 1.0, 1.5, and 2.0, respectively.

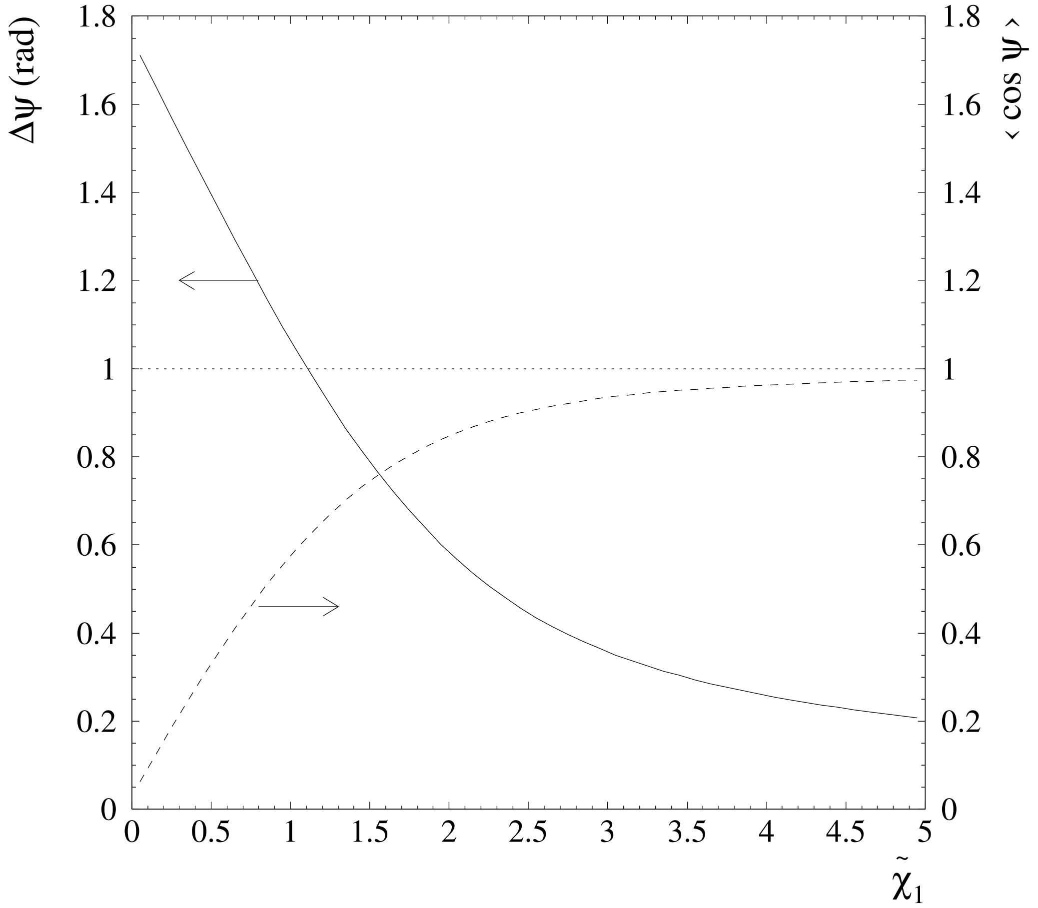

Figure 2.8: Reaction plane resolution as a function of parameter $\tilde{\chi}_1 = \tilde{v}_1/\sigma$. Two useful sets of numbers are given. The *r.m.s.* of the reaction plane measurement $\Delta(\psi)$ (solid line, labeled on the left), and $\langle\cos\psi\rangle$ (dashed line, labeled on the right).

eters $\tilde{\chi}_a = \tilde{v}_a/\sigma_a$ and $\tilde{\chi}_b = \tilde{v}_b/\sigma_b$.[12] The optimal reaction plane angle can be determined by taking the products of two equations of the form of (2.34) for a and b, and calculating the angle ψ_r at which a maximum likelihood is achieved for this product. Following the discussions in Appendix C, we obtain,

$$\psi_r = \arctan \frac{\chi_a \tilde{\chi}_a \sin(\psi_a) + \chi_b \tilde{\chi}_b \sin(\psi_b)}{\chi_a \tilde{\chi}_a \cos(\psi_a) + \chi_b \tilde{\chi}_b \cos(\psi_b)}. \tag{2.42}$$

On the other hand, a simple estimate for ψ_1 from the combined windows is

$$\psi_1 = \arctan \frac{\sum\limits_{\nu \in a,b} r_\nu \sin(\phi_\nu)}{\sum\limits_{\nu \in a,b} r_\nu \cos(\phi_\nu)} = \arctan \frac{v_a \sin(\psi_a) + v_b \sin(\psi_b)}{v_a \cos(\psi_a) + v_b \cos(\psi_b)}, \tag{2.43}$$

where the summation is taken over particles in both windows. Obviously (2.42) and (2.43) are not the same. Since (2.42) takes into account the flow signal as a weighting factor, it should give a better resolution than (2.43), which indeed is proved by a Monte Carlo study (see Appendix C). We generalize (2.42) by dividing the rapidity into an infinite number of windows, and introduce a continuous weighting factor $\omega(y) = \tilde{v}(y)/\sigma(y)^2$,

$$\psi_r = \arctan \frac{\sum\limits_{\nu}^{M} \omega(y)\, r_\nu \sin(\phi_\nu)}{\sum\limits_{\nu}^{M} \omega(y)\, r_\nu \cos(\phi_\nu)}, \tag{2.44}$$

where $\omega(y)$ should have a "+" or "−" sign taking into account the direction of particle's sideward motion. The azimuthal angle of $\mathbf{Q}$ from (2.1) is actually a simplified version of (2.44); Eq. (2.44) has a smooth weighting factor $\omega(y)$ over the whole rapidity range, while (2.1) takes a simple three step function as $\omega = -1, 0, 1$ in backward, middle, and forward windows, respectively.

2.6 Azimuthal Correlations

This section discusses the correlations between azimuthal flow angles defined in different windows, or between flow angles derived, possibly, in the

[12]We discuss only the first harmonic here, and omit the subscript "1" for simplicity.

same window but using different harmonics. The observation of such correlations could be very helpful for understanding the nature of flow and in the reconstruction of a global picture of 3-D event shapes. This analysis is also free from the uncertainties associated with the determination of the reaction plane.

As was pointed out previously in Sec. 2.4, the parameters $\tilde{v}_n$ and σ can be evaluated from the experimental data by fitting the distributions $dw/v_n dv_n$ with Eq. (2.35). Non-zero values of $\tilde{v}_n$ would reflect the existence and magnitude of flow of the n-th harmonic. Next, one can continue the analysis and check how the detected flow in one rapidity window is correlated with flow in another rapidity window, or whether the flow of one particle species is correlated with the flow of another species. The study of such correlations was proposed as a proof of the existence of flow in [36] (where the authors discuss in our notation the correlations of ψ_1 from different rapidity windows) and in [40] (correlations of ψ_2 from different windows). In our more general approach, along with these correlations we can study correlations between flow of different types to define the overall flow picture. In general, one can study the correlations between any rapidity window and any harmonic, $(v'_m, m\psi'_m)$ and $(v_n, n\psi_n)$. Denoting the relative angle by $\varphi = \psi'_m - \psi_n$ and averaging over the reaction plane angle the correlations can be described by the distribution:

$$\begin{aligned}\frac{dw}{d\varphi} &= \int \frac{d^2w}{d\psi'_m\, d\psi_n} d\psi'_m\, d\psi_n\, \delta(\varphi - \psi'_m + \psi_n) \qquad (2.45)\\ &= \int F_m(\psi'_m) F_n(\psi_n) d\psi'_m\, d\psi_n\, \delta(\varphi - \psi'_m + \psi_n) = \int d\psi\, F_m(\psi + \varphi) F_n(\psi),\end{aligned}$$

where $F_m(\psi'_m) \equiv dw/d\psi'_m$, $F_n(\psi_n) \equiv dw/d\psi_n$, and can be obtained from (2.39). Eq. (2.45) permits to calculate the correlation between azimuthal flow angles in different rapidity windows using the fit parameters ($\tilde{v}_n$, σ; $\tilde{v}'_m$, σ') to the distributions (2.35). Eq. (2.45) is not in an analytical form, but the calculation can be done numerically.

Note that the form of (2.45) is similar to (2.19). We can now answer the question raised in Sec. 2.2.5 about sensitivity. According to Eqs. (2.28) and (2.29), the parameter that controls the magnitude of the two particle correlation is the anisotropy parameter v_n itself,[13] while the corresponding parameter in our approach is $\tilde{\chi}_n = \tilde{v}_n/\sigma$, which is amplified by about a factor of $\sqrt{M}$. The difference originates from the fact that in the study of collective phenomena the collective (sum) variables fluctuate less than variables describing individual particles.

[13] Fluctuations are neglected and we have $v_n = \tilde{v}_n$.

There are a few more points to be addressed. Firstly, the derivation of (2.45) is based on the assumption of $(v'_m, m\psi'_m)$ and $(v_n, n\psi_n)$ being independent. If particle correlations between the two rapidity windows can not be neglected, an additional correlation will be present in the data. The comparison between results from (2.45) and the experimental data will provide the means to study those particle correlations, not due to flow, but due to momentum conservation, particle decay, etc. To turn this argument around, the consistency between (2.45) and data would be a proof of particles being emitted independently into the two rapidity windows under study. Secondly, the correlations between flow of different types in the same rapidity window can be biased by auto-correlations due to finite multiplicity. To avoid this problem one can study the correlations using as a reference an azimuthal flow angle defined in another rapidity window. Another way to suppress these pseudo-correlations is to calculate higher harmonics after removal of the lower harmonics event-by-event, *e.g.*, to perform a shift of the center of the particle distribution to the point (v_1, ψ_1) and then calculate $(v_2, 2\psi_2)$, etc..

2.7 Summary: Advantages and Limitations

We summarize our approach in the following:

(1) In the analysis of periodic functions, such as circular or azimuthal distributions, it is natural to adopt the method of Fourier expansion. The complete set of Fourier coefficients determines the azimuthal distribution completely. The azimuthal functions can be constructed from p_t, ϵ_t, multiplicity, or specific functions of one of the variables, *e. g.*, the use of p_t^2 to enhance contribution from particles with high p_t. To obtain a full triple differential cross-section, one can study particle distributions $dM/d\phi$ in different rapidity windows and p_t bins.

(2) It becomes clear, after the discussions in this chapter, that all the previously used 2-D analyses, including directivity, 2-D sphericity and two particle azimuthal correlation, merge naturally into the Fourier analysis. The higher harmonic components (3 and up) are also included in the present analysis, which have never been addressed before, but have been predicted to exist in hydrodynamical calculations (see Sec. 5.2).

(3) The event anisotropy parameters, which determine the azimuthal distribution, can be studied by the statistical distributions of event-by-event Fourier coefficients. It can be done either by fitting distributions of v_n with the analytical form of (2.35) in one (pseudo)rapidity window, or by studying correlations of ψ_n in different windows (according to Eq. (2.45)). The analysis

should be performed using both of them to either confirm the results, or to extract other information, *e. g.*, on particle correlations, etc., if they do not agree.

(4) The present method is especially useful for experiments like ours, where we have energy and multiplicity measurements over large solid angle, but do not have the capability of identifying each individual particle. When we construct Fourier coefficients, the summation over ν is equivalent to the summation over the detector cells in a certain pseudorapidity window if we choose the simple linear form ϵ_t (not ϵ_t^2 or anything else). In this case the fluctuation parameter σ is a fit parameter, because it can not be estimated from Eq. (2.33) without the information of single particle spectra.

It is said that nothing is perfect. This approach has its limitations. They are mostly related to the assumptions dealing with fluctuations. We now discuss these limitations and possible resolutions.

(1) Particle correlations:

If the particle correlations are non-negligible we expect larger fluctuations, namely σ will be larger than expected from Eq. (2.33). As an extreme but intuitive example, we consider particles emitted in pairs. This could be the case if the Bose-Einstein correlation between identical particles is very strong, but a condensation has not happened yet. The effective multiplicity in this case is only half of the real multiplicity, and fluctuations are increased by a factor of $\sqrt{2}$. In case where particle correlation manifests itself in two rapidity windows under study, the two probability distributions in the azimuthal angles are no longer independent (in Eq. (2.45) $d^2w/d\psi'_m\,d\psi_n \neq (dw/d\psi'_m)(dw/d\psi_n)$). As another extreme example, let us consider the two rapidity windows covering the entire forward and backward hemispheres. If we choose p_t as the variable, then momentum conservation will cause $dw/d\varphi$ in (2.45) to exhibit a δ-function at $\varphi = \pi$ whether or not any azimuthal anisotropy is established! If one selects relatively narrow rapidity windows, it is unlikely that momentum conservation dominates the correlation. If correlations are not strong, we can introduce a "direct" correlation function between two rapidity windows,

$$1 + \Lambda(\varphi) = \frac{d^2w/d\psi'_m\,d\psi_n}{(dw/d\psi'_m)(dw/d\psi_n)}, \tag{2.46}$$

and treat this as an additional fit parameter. This correlation function is similar to $(1+\lambda)$ defined in (2.20). The intrinsic two particle correlation $(1+\lambda)$ certainly contributes to the correlation between rapidity windows $(1+\Lambda)$, but is reduced due to the fact that the latter is the correlation of two groups of particles rather than of two particles. We conclude that even if particle correlations are non-negligible, the procedure remains valid, except that σ is modified by an effective multiplicity in Eq. (2.33), and that one needs to insert a correlation coefficient $(1 + \Lambda(\varphi))$ in the azimuthal correlation (2.45).

(2) Multiplicity in a rapidity window:

The discussion on fluctuations above is based on the Central Limit Theorem, where $M \gg 1$ is required. A Monte Carlo study (Appendix A) shows that if $M > M_1 = 10$ the resulting 2-D distribution is basically a 2-D Gaussian. Without this condition the 2-D functional form can still be extrapolated from the known single particle spectra, but the analytical form will be more complicated. A second limit on the multiplicity is set by the condition to observe a local minima for $dw/v_n dv_n$ at $v_n = 0$. From the condition $\tilde{v}_n/\sigma > \sqrt{2}$ and Eq. (2.38) we get

$$M > M_2 = \langle r^2 \rangle / \langle r \cos(n\phi) \rangle^2. \tag{2.47}$$

The smaller the anisotropy, the larger the critical number M_2. Eq. (2.47) serves as a sufficient condition for the anisotropy parameter $\tilde{v}_n$ to be extracted from the distribution of v_n. However, the simultaneous fitting to v_n distributions of several harmonics does not require this condition.

(3) Event classes and centrality bins:

Global variables like E_T, M or E_Z are used for selecting the impact parameter b. But the correlation between these variables and b has finite width due to fluctuations. To minimize fluctuations, one should optimize the centrality variable, *e. g.*, combine several variables. If event statistics allows, one should have as many centrality bins as possible to achieve "purer" event classes. One could also take into account the additional fluctuations, *e. g.*, by replacing a constant M in one rapidity window with a narrow Gaussian distribution centered at M with standard deviation ΔM. Although an analytical form will be very complicated, the physical picture is clear: in the same event class one replaces a 2-D Gaussian distribution (2.34) with a convolution of many 2-D Gaussians with σ ranging from $\sigma(M - \Delta M)$ to $\sigma(M + \Delta M)$. This will increase the fluctuation parameter, but will alter the anisotropy parameters little as long as ΔM is small. Besides the "normal" fluctuations caused by kinematics and statistics, there is a possible dynamical fluctuation: for events in the same centrality bin, some of the events may remain in the hadronic world, while others may undergo a phase transition to enter the QGP world. This would make the flow parameters $\tilde{v}_n$ not constant anymore in the same centrality bin. In this case we have to revise our concept of "event class" to implement other variables, especially those QGP signatures. A multi-dimensional event-by-event analysis is needed in this case, and will be discussed in Chapter 6.

(4) Condition for simultaneous fitting:

Simultaneous fitting requires all distributions in v_n to have the same fluctuation parameter σ, which is only true if $\tilde{v}_n \ll 1$. Otherwise, we should consider how σ_n is modified by $\tilde{v}_n$. Suppose the n-th harmonic is dominating in the azimuthal distribution, and we have $r(\phi) \simeq (x_0/2\pi)[1 + 2\tilde{v}_n \cos(n\phi)]$ (the x-axis is in the reaction plane). We get $\sigma_n \simeq \sigma(1 + \tilde{v}_n^2)$, and then replace the σ with σ_n to do the simultaneous fitting.

If an anisotropy parameter $\tilde{v}_n$ is really large, we do not have $\sigma_{n;x} = \sigma_{n;y}$ anymore. The 2-D Gaussian distribution (2.34) should be re-written in Cartesian coordinate with different values of $\sigma_{n;x}$ and $\sigma_{n;x}$. The discussion afterwards needs revision, which is doable in principle, but will be very complicated. On the other hand, the two particle azimuthal correlation function (with Fourier expansion as input, see Eqs. (2.29-2.30)) provides an alternative way, and is suitable to analyze larger flow signals. Since it is not limited by M in each rapidity window, one can use finer rapidity windows and p_t bins to study the details of the triple differential cross section. In general, our approach for the flow analysis and the two particle azimuthal correlation are complementary to each other. The former is sensitive to the presence of even a tiny anisotropy as long as the fluctuations are under control (large M in each rapidity window), while the latter is capable of detecting large anisotropies (when the former does not work well) regardless of multiplicity fluctuations. The former is favorable for ultra-relativistic heavy ion collisions, where small anisotropy and large multiplicity are anticipated.

Chapter 3

Experimental Setup and Data Collection

3.1 Apparatus

We briefly go through the experimental setup in this section. Similar write-ups can be found in some of the earlier PhD theses from the E814/E877 Collaboration. I will refer, if necessary, to previous theses for a more detailed description.

The layout of the AGS is displayed in Fig. 3.1. Experiment 877 is in the C5 line as highlighted in the figure. The setup of the experiment is shown in Fig. 3.2, which also defines a right-handed coordinate system with origin at the center of the target, the z-axis in the direction of the incident beam, and y-axis vertically upward. Beams enter from the left hand side, which we will refer to as upstream. The major detectors installed in the initial phase of E877 are listed in the order from upstream to downstream.

Beam counters (BSCI):

Beam scintillators are used to define a valid beam particle entering the apparatus. There are altogether four counters, S1, S2, S3 and S4, and a good beam is defined by the logic of $\bar{\text{S}}1 \times \text{S}2 \times \bar{\text{S}}3 \times \text{S}4$. They also measure the arrival time of each beam ion, and S4 provides the start time (T_0) with a time resolution of 35 ps for time-of-flight measurement. Details can be found in the PhD thesis of B. Hong [50].

Beam vertex detectors (BVER):

Two vertex detectors located between S1 and S3 are used to measure the horizontal position of the beam particle. They are made of 300 μm thick silicon wafers and each detector consists of 320 strips vertically oriented with a pitch of 50 μm. This results in a resolution of the horizontal beam position at the target of approximately 50 μm, and the beam angle about 40 μrad.

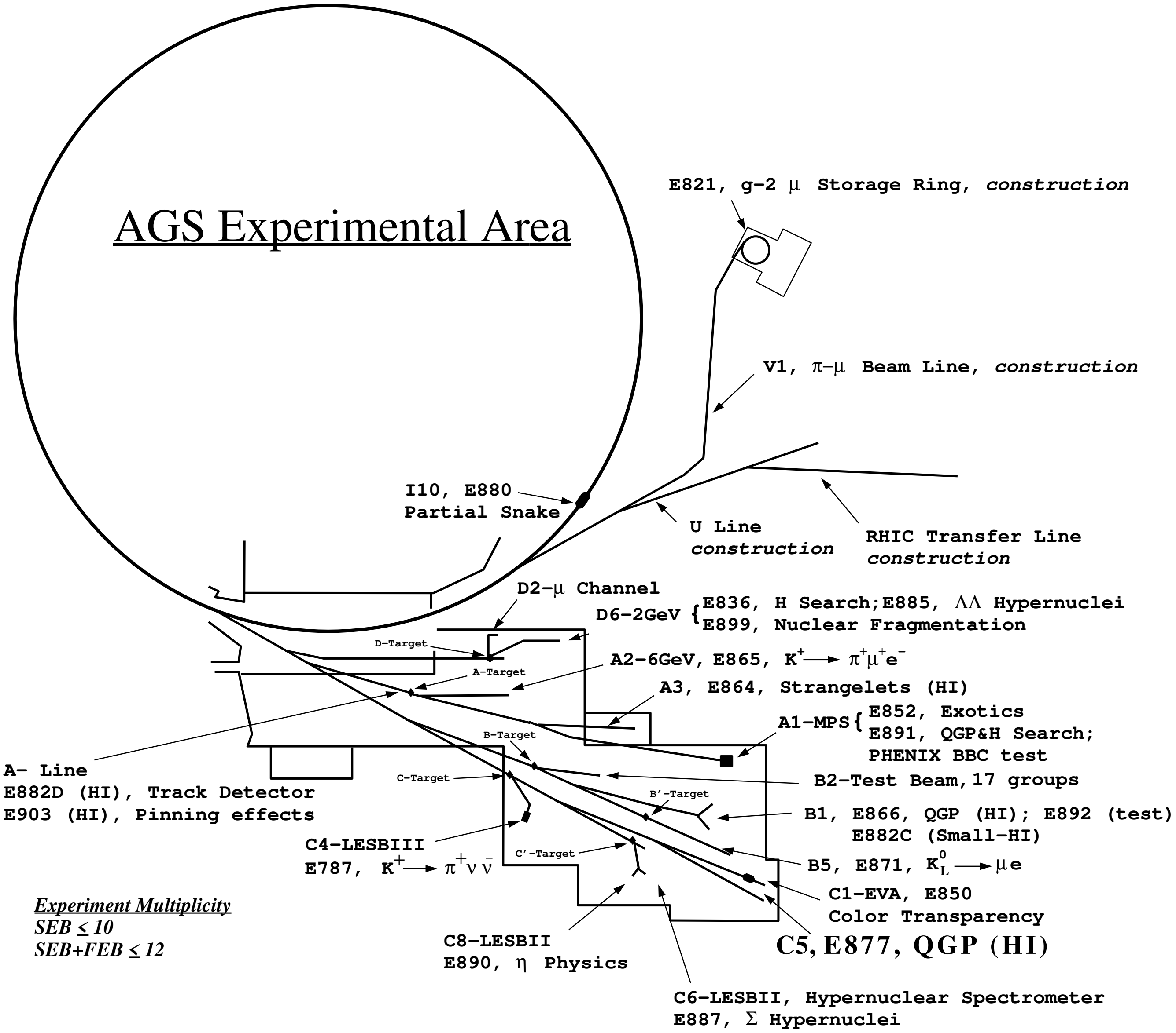

Figure 3.1: Layout of the AGS at BNL, and the location of Experiment 877.

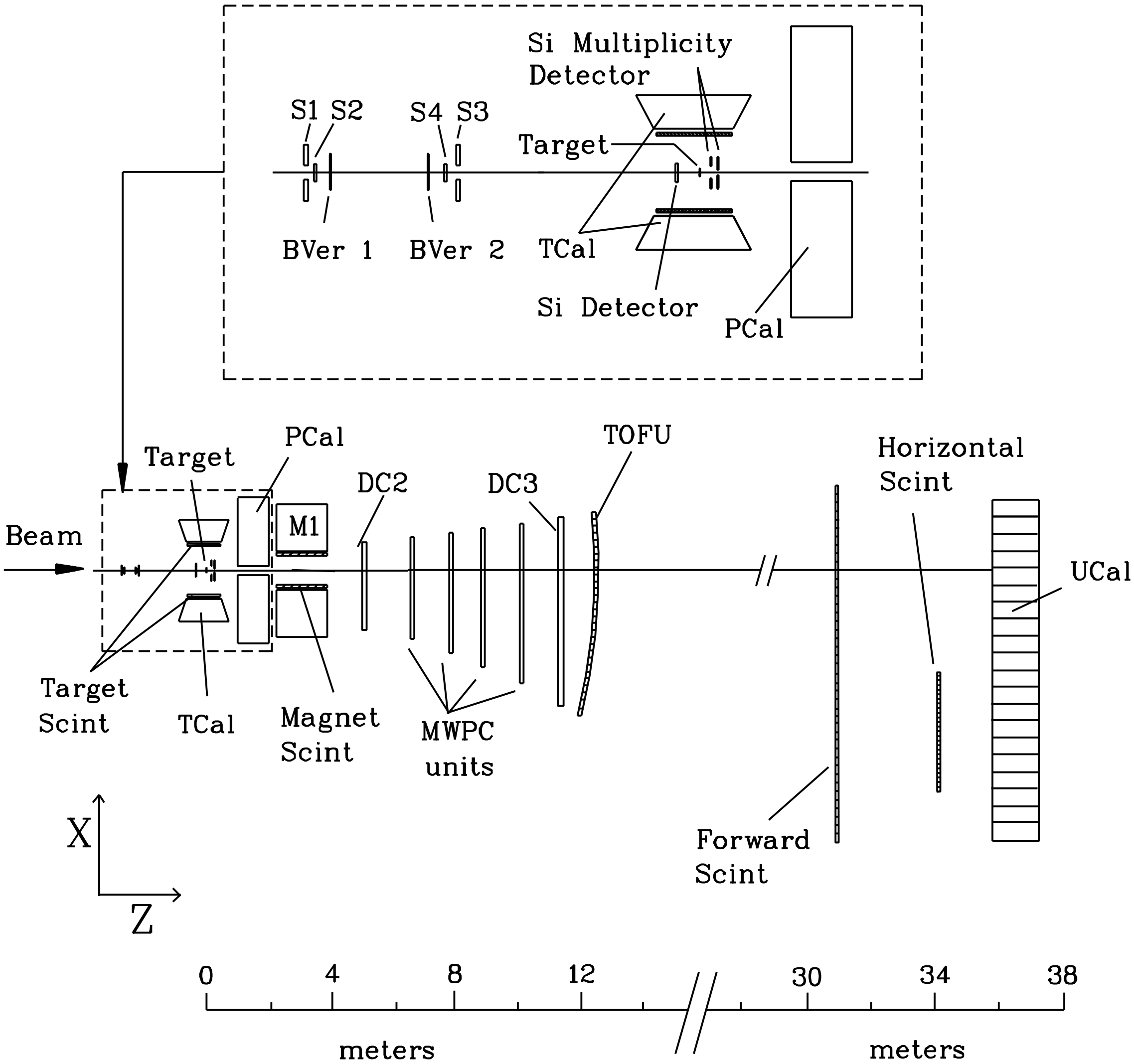

Figure 3.2: Set up of Experiment E877.

Upstream silicon detectors (SILI):

A silicon detector is placed immediately upstream and downstream of the target. SILI measures dE/dx and hence the charge of particles passing through it. It also allows one to reject those particles with charge lower than the charge of the ion beam. Obviously one should not see a charge higher than that of the beam, which can be used as an offline cut.

Target calorimeter (TCAL):

A full description can be found in the PhD thesis of L. Waters [51]. Fig. 3.3 shows a side-view and an end view of TCAL. The TCAL is an electromagnetic calorimeter made of 992 NaI crystals. The crystals are shaped to form an approximately projective geometry with respect to the target. The dimension of the crystals is about 3.6 cm $\times$3.6 cm $\times$13.8 cm. Given the radiation length $X_0 = 2.59$ cm and hadronic interaction lengths $\lambda = 41.4$ cm for NaI, the depth corresponds to about 5.4 radiation lengths, and 0.34 hadronic interaction length. During the 1992 run, the back wall was removed to implement a range telescope detector (TELE) sitting at a backward angle, and the remaining 832 crystals of the up-down-left-right walls were used to measure the energy flow corresponding to 2π coverage with 64 divisions azimuthally and 13 divisions in the beam direction. In this configuration, TCAL detects energy flow in the region of about $48° < \theta < 135°$ in angle and $-0.5 < \eta < 0.8$ in pseudorapidity.

Silicon multiplicity detector (MULT):

The multiplicity detector consists of two disks of 300 μm thick silicon, each segmented into 512 nearly-square pads in η and ϕ space, with roughly the same hit occupancies for each pad [48, 49]. Positioned inside the TCAL, MULT covers a pseudorapidity region $0.87 < \eta < 2.46$, and is designed to detect the multiplicity of charged particles and their distribution $d^2M/d\eta d\phi$.

Participant calorimeter (PCAL):

The PCAL is a lead/iron/scintillator sampling calorimeter. The scintillators are read-out using wave length shifting optical fibers connected on the other end to photo-multipliers. The PCAL measures energy flow in the polar angular region $1° < \theta < 47°$, corresponding to the pseudorapidity range $0.83 < \eta < 4.7$, with a depth of four hadronic interaction length. Fig. 3.4 shows the geometry of PCAL. It is segmented laterally into 8 radial and 16 azimuthal elements and longitudinally into 4 depth layers. The total number of channels is $8 \times 16 \times 4 = 512$. A detailed description of the detector can be found in [52, 53, 54].

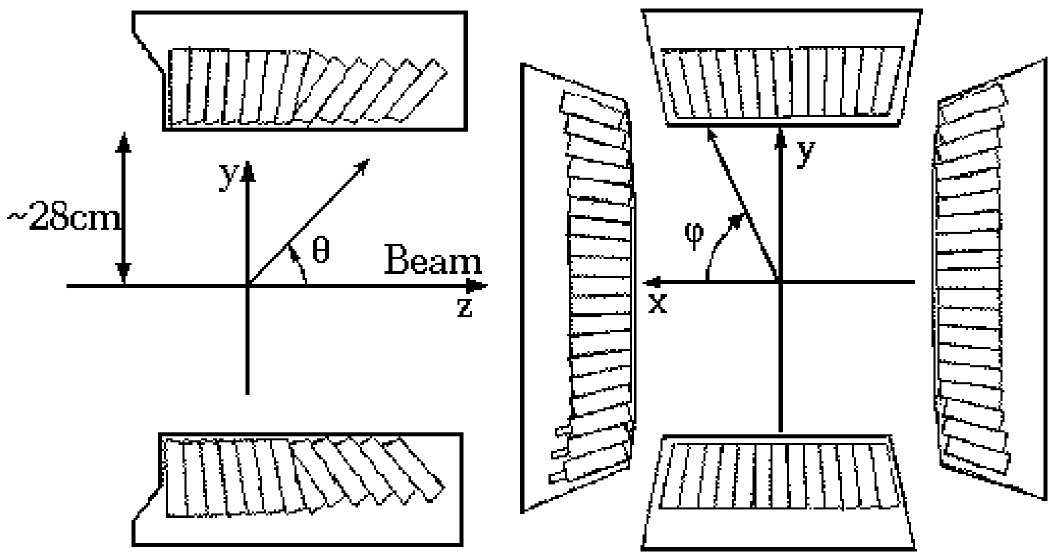

Figure 3.3: Side view (left) and end view (right) of TCAL.

Forward spectrometer:

Particles passing through the central hole of the PCAL are identified with good momentum resolution by the forward spectrometer. It consists of a dipole magnet right after PCAL, two drift chambers (DC2 and DC3), and two walls of scintillation counters (TOFU and FSCI). Both DC2 and DC3 consist of 6 drift planes and one pad plane, providing horizontal (in the magnet band plane) and vertical position measurements, which in turn determine the momentum/charge ratio of the particles. Both TOFU (Time Of Flight Upstream) and FSCI (Forward Scintillators) measure the time of flight of the particles with different resolution and granularity. The combination of the momentum and time of flight identifies particles by their mass. Detailed information can be found in the PhD theses of J. Dee [16] and B. Hong [50].

Uranium calorimeter (UCAL):

This is the last detector down stream, positioned about 35 meters from the target. It is designed to measure the energy of forward particles, especially neutrons, with a resolution of about $\Delta E/E \simeq 50\%/\sqrt{E}$. It has 20 modules lined up horizontally (perpendicular to the beam direction), and each module is segmented into $24 = 2$ (horizontal axis) $\times$ 12 (vertical axis) towers of 10×10 cm^2 cross sectional area. This results in an angular coverage relative

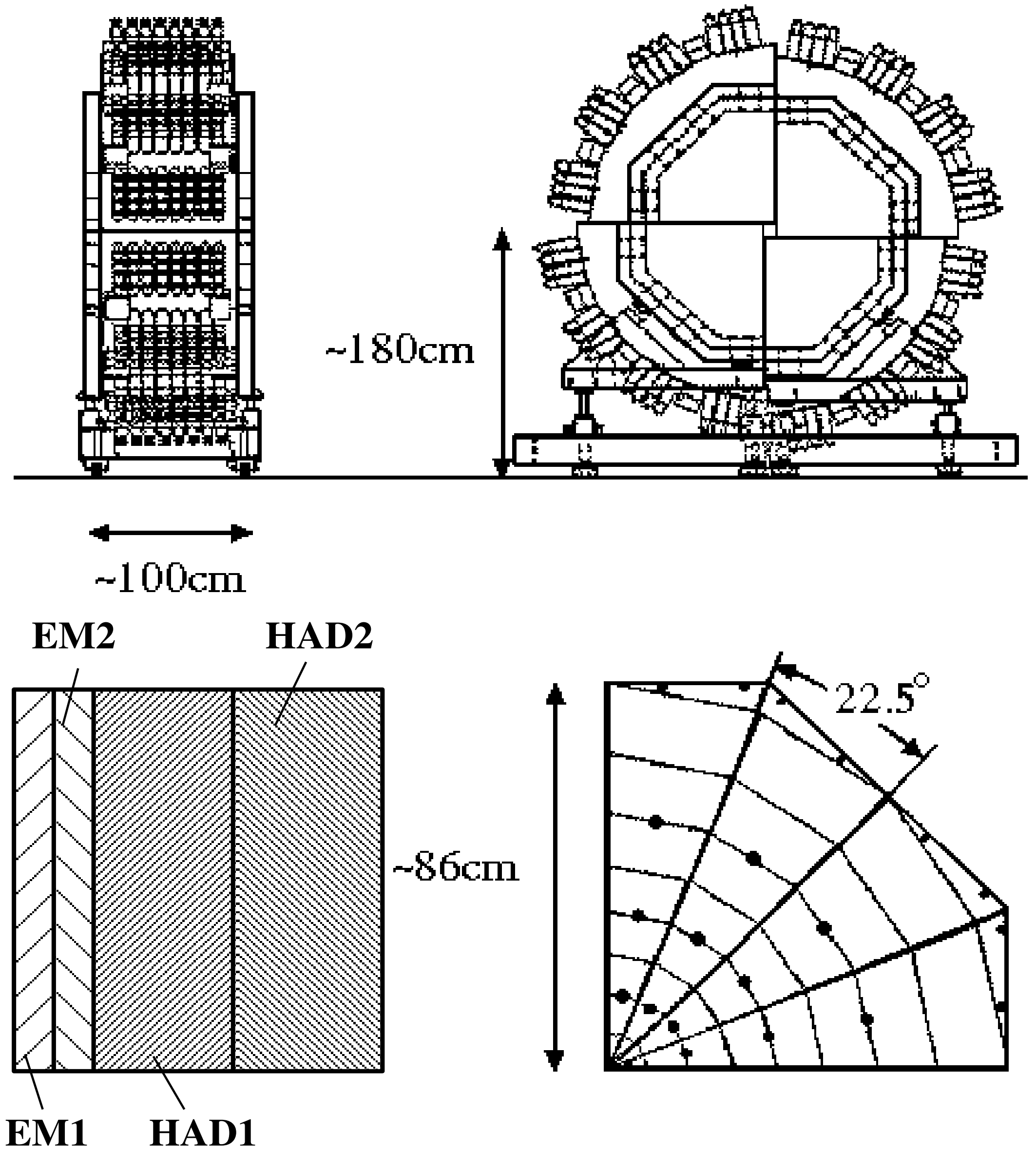

Figure 3.4: Side view (upper-left) and end view (upper-right) of PCAL, and its schematic longitudinal (lower-left) and lateral (lower-right) segmentations.

Table 3.1: Run statistics for the 1992 run.

Target	MT	Al	Cu	Au	Pb	Pb
thickness(g/cm^2)	-	0.242	0.501	0.988	1.158	0.552
No. of events (k)	80	150	100	100	100	40

to the target of $-5.2° < \theta_x < 1.3°$ horizontally and $-0.98° < \theta_x < 0.98°$ vertically. Similar to PCAL, it is also a sampling calorimeter with uranium and iron plates as absorbers interleaved with a total depth of about 6 interaction lengths. The purpose of using uranium is to compensate the energy deposition between hadronic interactions and electromagnetic interactions via the fission of the uranium. The PhD thesis of W. J. Llope [55] provides full information on this detector.

The principal detectors in this thesis are TCAL and PCAL. These two calorimeters plus UCAL cover almost the full solid angle with respect to the target, which is unique among AGS heavy ion experiments.

3.2 Data Collection

Data were collected in the Spring of 1992 with a Gold (Au) beam, the heaviest ion beam available at the AGS. It was a milestone when the AGS delivered a Au beam for the first time on April 25, 1992. And it was an exciting moment when the Au beam was delivered to the E877 beam line on April 26 at 3:00 am. The first E877 Au run lasted for 10 days. In spite of a relatively short run, a large quantity of data was collected. Table 3.1 shows the event statistics for different targets. Here, "MT" stands for an empty target frame used for background determination and subtraction.

Since the average particle multiplicity in Au on Au collision is about a factor of 2.5 higher than in Si on Au collisions, an upgrade of the spectrometer was necessary. This upgrade was not completed for the 1992 run, so that data useful for physics analysis from this run came from the calorimeters and multiplicity detector only. The primary physics goal of this run was to measure the total E_T production and to see how it scales as compared to smaller collision systems. The longitudinal distributions measured with PCAL and TCAL provide information on how $dE_T/d\eta$ behaves as a function of centrality. The event fluctuations can be studied via correlations between different calorimeters. Another goal was to study the azimuthal anisotropy, although it was not known at the time whether a signal would be detectable. For all the above purposes, one requires rather uniform event statistics at all centralities. However, the natural minimum-bias samples gives us more peripheral events than central ones, since $\frac{dN}{db} \propto b$ where b is the impact parameter.

A more uniform distribution can be achieved experimentally by introducing centrality triggers, which discriminate events and selects some of them while rejecting others. During the 1992 run, there were about 20 k beam particles per spill (1.5 sec length every 4 sec) passing the *beam trigger*, which is defined by the logic of $\bar{\mathrm{S}}1 \times \mathrm{S}2 \times \bar{\mathrm{S}}3 \times \mathrm{S}4$. The thickness of the targets listed in Table 3.1 correspond to about 1% of a Au interaction length, which means there were about 200 beam-target inelastic interactions in each spill. A *pre-trigger* requires a minimal energy deposition in PCAL (about 1 GeV) to select these 200 interactions out of 20 k incident beam particles. A *first level trigger* is set to reject an event where another beam particle enters the apparatus within 1 μs after this event. A *second level trigger* is designed to select 50 events per spill, limited by our data acquisition system (see PhD thesis of J. Dee [16] for details of the data acquisition system). A *second level trigger* is designed to do this selection. In this trigger, analog signals from different sectors of the TCAL, PCAL, and MULT are digitized by FERA ADCs (fast analog to digital converters) to form a digital sum which is proportional to the total transverse energy (E_T). We then compare this digital sum with three levels of thresholds, keeping all the events passing the highest threshold, while only keeping a fraction of the events passing the lower thresholds by down-scaling these triggers. Table 3.2 lists down-scale factors, three thresholds and their corresponding cross sections for each of the targets. They were chosen to have the balanced event statistics over the whole range of E_T (centrality), and to have just about 50 events per spill to be recorded on tape.

The calibration of TCAL and PCAL is described in [51] and [52], respectively. The TCAL calibration was done by matching the cosmic ray data with simulations made with the tracking program GEANT (Sec. 4.2.1) to adjust the gain values for each NaI crystal. For PCAL, the absolute scale on the energy measurement was done with muon beams. To maintain the calibration and monitor gain shifts, a Cobalt (^{60}Co) source system is used. The system moves the radioactive source through PCAL and detects the responses from the surrounding channels as a function of the source position.

Table 3.2: Second level trigger thresholds and down-scale factors.

	thresholds, fraction of cross-sections, and down-scale factors					
triggers	TCAL1	TCAL2	TCAL3	PCAL1	PCAL2	PCAL3
MT, Al	15 62%	100 20%	200 3.2%	100 63%	700 15%	1270 3.5%
Cu	15 65%	140 20%	355 3.8%	100 65%	700 19%	1560 3.3%
Au, Pb	15 65%	140 24%	825 3.9%	100 64%	850 17%	2150 3.1%
down-scale	21	6	1	21	6	1

Chapter 4

Data Analysis and Results

4.1 Global Observables and Their Correlation

Before proceeding with the analysis of longitudinal and azimuthal E_T distribution, let us first study the transverse energy distribution in TCAL and PCAL, and the correlation between different global observables.

4.1.1 The transverse energy distributions

TCAL is an electromagnetic calorimeter with about a 5.4 radiation length depth. This corresponds to about one third of the hadronic interaction length. Correction for energy leakage out of the calorimeter depends on the particle composition and energy distribution. Thus, the unfolding of the measured E_T is somewhat model dependent. For more detail see [51]. For this reason, only the measured total TCAL E_T is presented here. The real E_T in the acceptance of TCAL is about twice as much as the measured one. This estimate is obtained from result of GEANT studies (see Sec. 4.2.1).

Fig. 4.1(a) displays the differential cross-sections for E_T production measured in the TCAL for all four targets Al, Cu, Au, and Pb. The data are from pre-triggers and three TCAL E_T triggers (Table 3.2). The cross-section is calculated for each target in each trigger,

$$\frac{d\sigma}{dE_T} = \frac{d}{n_t \cdot B} \frac{dN}{dE_T}, \tag{4.1}$$

where d is the down-scaling factor for this trigger, n_t is the number of target atoms per unit cross sectional area, and B is the number of beam particles. The overall $d\sigma/dE_T$ is obtained after combining all triggers in different E_T regions.

Fig. 4.1(a) shows the corrected $d\sigma/dE_T$ after subtracting the $d\sigma/dE_T$ due to interactions other than those in the target (from the MT runs) calculated with properly normalized beam particles B and the same n_t as for the target being subtracted from. This MT-subtraction is important at low E_T (about 70% at $E_T = 2$ GeV), but negligible for $E_T > 8$ GeV. Since the pre-trigger is not minimum-bias, but corresponds to about 60% of the geometric cross section, events are biased below 4 GeV for Au and Pb targets, and about 3 and 2 GeV for Cu and Al targets, respectively. Below these E_T values, $d\sigma/dE_T$ spectra are lower than the real ones.

Taking a simple geometric model, and neglecting fluctuations, one could naively obtain the impact parameter for each event from any one of the global variables. For E_T we have,

$$\pi b^2 = \sigma(0 \to b) = \int_{E_T}^{\infty} \frac{d\sigma}{dE'_T} dE'_T, \tag{4.2}$$

which yields b as a function of E_T (shown in Fig. 4.1(b)). In reality, fluctuations are present in the anti-correlation between b and E_T. Fig. 4.1(b) does not hold on an event-by-event basis. On average, it is about right for the mid-central collisions, where the fluctuations can go either way. However, for very central collisions, the asymmetric fluctuations result in a smaller calculated b than the real one. For very peripheral collisions the estimated b is also smaller than the real one due to the trigger bias discussed in the last paragraph. The estimated impact parameter b will be used throughout this thesis as a centrality measure, but one should keep in mind that it is really just a measure of the cross section.

Taking events from pre-trigger and three PCAL E_T triggers and following the same procedures, $d\sigma/dE_T$ spectra and b versus E_T for PCAL are obtained and shown in Fig. 4.2. The PCAL E_T here is also the measured quantity without correction for the detector response. The correction can be done by a matrix approach [54], which is one of the main topics of Ref. [52]. The overall leakage correction factor is 1.2–1.3 (comparing to 2 for TCAL), and is less sensitive to the nucleon/pion ratio. Due to its acceptance in pseudorapidity and the smaller leakage, PCAL E_T is about one order of magnitude larger than TCAL E_T, and has smaller relative fluctuations as can be seen from the sharp fall-off of the distribution. Therefore it measures the centrality more accurately.

The shape of the E_T distribution:

As a starting point, it is reasonable to assume the E_T production is proportional to the total excitation energy, *i. e.* the available energy in the c.m.s.

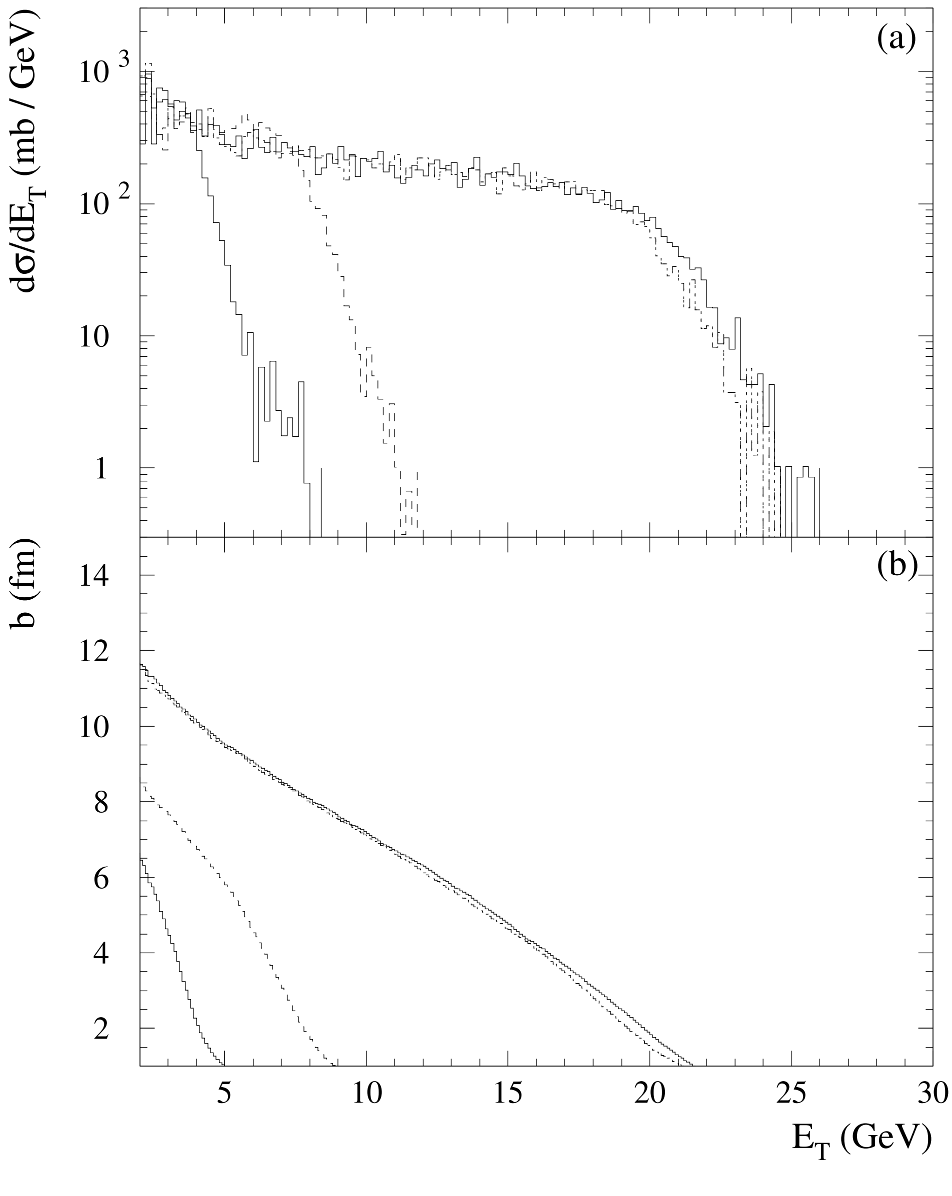

Figure 4.1: (a) The TCAL E_T differential cross-section for Al (dotted line), Cu (dashed-dotted line), Au (solid line), and Pb (dashed line) targets, respectively. (b) Impact parameter b as a function of TCAL E_T for all targets (according to Eq. (4.2) and neglecting fluctuations).

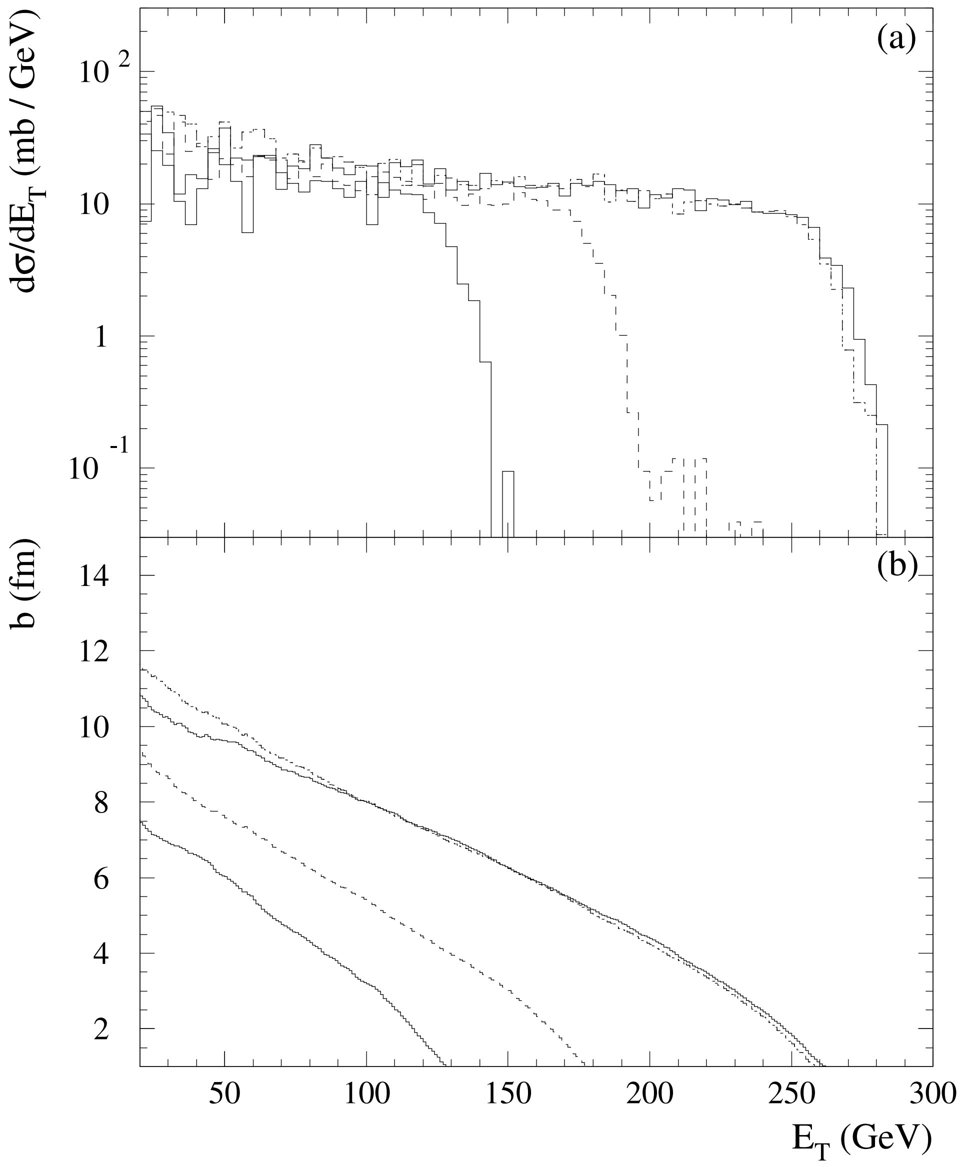

Figure 4.2: (a) The PCAL E_T differential cross-section for Al (dotted line), Cu (dashed-dotted line), Au (solid line), and Pb (dashed line) targets, respectively. (b) Impact parameter b as a function of PCAL E_T for all targets. (according to Eq. (4.2) and neglecting fluctuations)

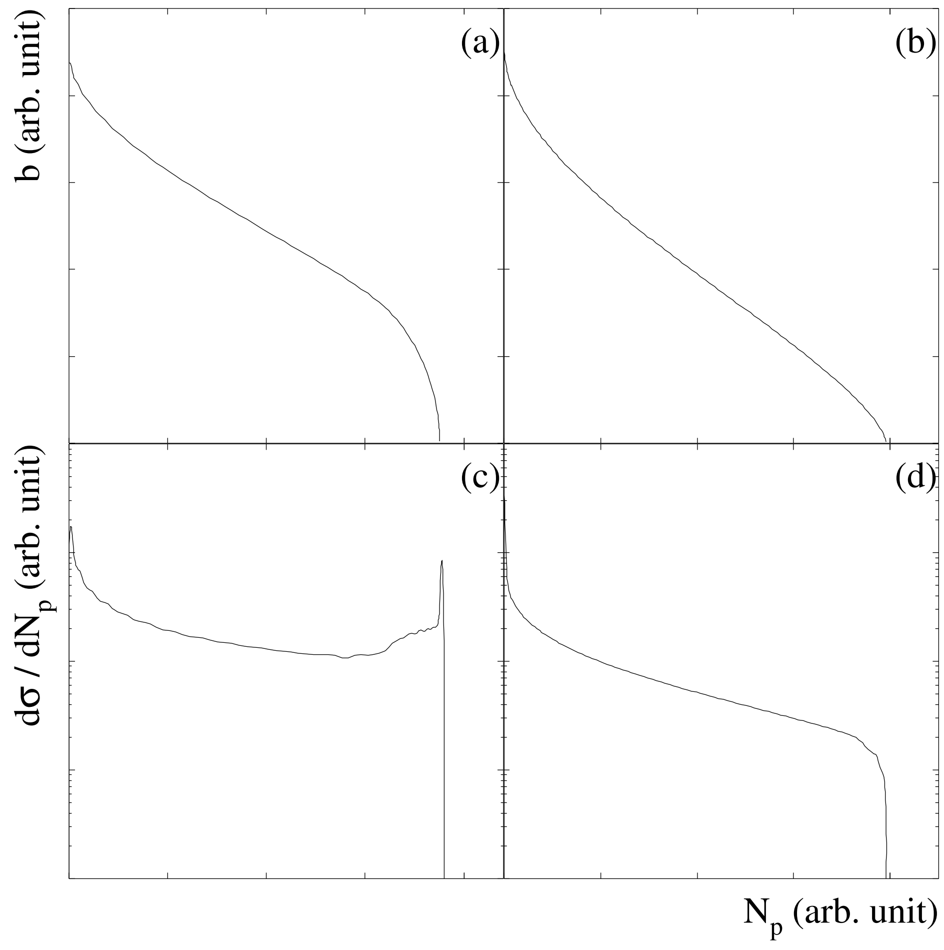

Figure 4.3: The number of participants N_p in a simple geometric model. The top two figures are b versus N_p, and bottom figures show $d\sigma/dN_p$. On the left, one of the radii of the two nuclei is a factor of two larger than the other. The figures on the right are for a symmetric collision system.

$$E^* = E^{\text{c.m.s.}} - m_u(N_b + N_t), \tag{4.3}$$
$$E^{\text{c.m.s.}} = m_u\sqrt{N_b^2 + N_t^2 + 2N_bN_t\gamma_b},$$

where m_u is the nucleon mass, and γ_b is the Lorentz gamma of the beam. The numbers of participating nucleons from the beam and the target for a given centrality are N_b and N_t, respectively. For a symmetric system, $N_b = N_t = N$ and $E^* = m_uN(\sqrt{2+2\gamma_b} - 2)$. The available energy E^* is proportional to the total number of participating nucleons $N_p = 2N$. We now calculate N_p as a function of impact parameter b and use

$$\frac{d\sigma}{dE_T} \propto \frac{d\sigma}{dN_p} = \frac{2\pi b db}{dN_p} \tag{4.4}$$

to obtain the differential cross section in terms of the number of participants. Fig. 4.3 displays the correlation of b and N_p, as well as $d\sigma/dN_p$ for sharp sphere nuclei, for a symmetric ($R_b = R_t$) and an asymmetric system ($R_t = 2R_b$, similar to Si on Au) The shape of the distribution in Fig. 4.3(d) reproduces the general feature of the Au on Au, Pb data. In reality there are fluctuations between E_T and N_p that smears out the tail of the distribution. This causes the peak structure to disappear completely for Au on Al, Cu. This simple geometric model explains qualitatively the shape of the distribution, but the coefficient of the proportionality, or the absolute E_T is unknown.

The total E_T production for central Au on Au collisions:

Since the tail of the E_T distribution reflects not only the E_T production for the most central collisions, but also the fluctuations, it is not straightforward to obtain the E_T production for zero impact parameter events. A way to do this is given by Stachel and Young [4]. The idea is to get the mean transverse energy values E_T^0 for different models at $b = 0$ fm, and then to calculate the cross-sections $\sigma(E_T > E_T^0)$ for minimum-bias distributions. In the data one would then integrate from higher E_T down to the corresponding cross section, and find the E_T that belong to this integration limit. This method only requires that the fluctuations in reality and in models are the same rather than the overall E_T scale. This was done for PCAL and the results are discussed in [14]. A more detailed discussion can be found in the thesis of Z. Zhang [52], from which $E_T^0 = 318$ GeV was deduced for PCAL after correction for leakage. An alternative way based on only experimental data is given in Sec. 4.1.2, which gives $E_T^0 = 38$ GeV for TCAL after correction for leakage (19 GeV before correction, See Table 4.1). Using these numbers and neglecting E_T contributions from $\eta < -0.5$ and $\eta > 4.7$ (see the

$dE_T/d\eta$ distribution in Sec. 4.2), the total E_T production for typical central collisions ($b \simeq 0$ fm) is $E_T^0 \simeq 356$ GeV. What does this number mean? Let us first compare this with the total available excitation energy $E^* = 578$ GeV, which can be computed from Eq. (4.4) with $N_b = N_t = 197$ ($b = 0$ fm). Suppose all particles are emitted isotropically, the total $E_T^{\text{c.m.s.}}$ should simply be $\frac{\pi}{4}E^* = 454$ GeV, which is larger than our measured value 356 GeV. But since E_T is not Lorentz invariant, we should calculate E_T^{lab}, which should be larger than $E_T^{\text{c.m.s.}}$ due to kinematics, but there could also be incomplete stopping. A calculation from a 3-D isotropic fire ball, which assumes full stopping and has a thermal distribution for particles and takes into account energy and baryon number conservation, gives a result $E_T^{\text{lab}} = 514$ GeV [56]. A Landau fire ball model [57], which allows for longitudinal expansion of the system can reproduce the data very well [56]. From the distributions of identified particles there is support for such longitudinal expansion [19]. We conclude that the energy distribution is not isotropic, but rather elongated in the longitudinal direction due to expansion.

Target dependence:

We see from Figs. 4.1 and 4.2 that the larger the target mass number, the more E_T is produced into both the TCAL and PCAL acceptance. However, the relative differences between different targets in TCAL are larger than those in PCAL. When a Au beam hits a smaller target, the c.m.s. frame is moving at a larger rapidity relative to the laboratory frame. Given the fact that TCAL is in the backward hemisphere, while PCAL covers the region around mid-rapidity and the forward hemisphere, the observed target A dependence can be understood qualitatively as due to kinematics. This can been seen even when comparing the Au (A=197) and Pb (A=208) targets. The difference at the tail of the E_T distribution is about 4% for TCAL, and 2% for PCAL, while a simple estimate from the numbers of participants yields about 3%.

A very important message is obtained from a systematic comparison between a light and a heavy symmetric system, *i. e.*, Si on Al and Au on Au, which is discussed in [14] and [52]. It is worthwhile to repeat these numbers to emphasize that the E_T production increases non-linearly as a function of the mass number of the collision system. Using the method quoted above to find the transverse energy for a typical $b = 0$ collision, E_T^0, we found $\frac{E_T^0(\text{Au}+\text{Au})}{E_T^0(\text{Si}+\text{Al})} = 7.9$, while the ratio of the available energy is only $\frac{E^*(\text{Au}+\text{Au})}{E^*(\text{Si}+\text{Al})} = 5.9$. Taking into account the small difference in beam energy and assuming that E_T scales as a power law with respect to the number of participants, $E_T^0 \propto N_p^\alpha$, we find $\alpha = 1.17$. This means the E_T production is a factor of 2.76 larger than anticipated from a simple linear dependence on A for central Au on Au collisions.[1].

4.1.2 The correlations of global variables

E877 has three calorimeters and a multiplicity detector to measure the global variables. It is interesting to see how these different global variables are correlated with one another. We first discuss PCAL E_T versus TCAL E_T. We then present the zero degree energy (E_z) and its correlation with other variables. Finally, a 3-D correlation between TCAL E_T, PCAL E_T, and UCAL E_z is presented. The correlation of E_T and multiplicity is discussed in [49].

TCAL E_T versus PCAL E_T:

Fig. 4.4 shows the correlation between the TCAL E_T and the PCAL E_T for Si on Al and Au on Au collisions. The Si data were taken in 1990 with a beam momentum of 14.6 A·GeV/c. The contour lines in the 2-D histograms are for constant double differential cross sections $d^2N/dE_T^{\mathrm{TCAL}}dE_T^{\mathrm{PCAL}}$. One can immediately see that the fluctuations are much reduced in the Au on Au system as compared to Si on Al. To quantify this, projections are made on the two axes cutting on the other variable in the indicated bands. The positions of the bands are chosen at the energy level that saturates the mean value of the projected distribution on the other axis. At this point $\langle E_T^{\max}\rangle$ should roughly be equal to E_T^0, which is an alternative way to get this value experimentally. We fit Gaussian distributions to the projected distribution, and list the fit parameters in Table 4.1. The relative fluctuations are reduced by a factor of 3.0 for both TCAL and PCAL when going from the light to the heavy system. If the fluctuation is only statistical, one should have $\langle E_T^{\max}\rangle/\sigma \propto \sqrt{M}$, while multiplicity $M \propto N_p$ (the number of participants) to the first order.[2] The expected ratio between the Au on Au and the Si on Al systems is then $19.8/7.4 = 2.7$, just 10% smaller than the factor 3.0 from the data. This small difference could mean that the dynamical fluctuations in Au on Au are reduced due to, *e. g.*, longer life time, better thermalization. There are a few

[1] For central Au on Au collisions, $N_p = 394$, the ratio is $N_p^{1.17}/N_p = 2.76$

[2] We discussed E_T does not scale linearly with the number of participants N_p, but it was found that N_c scales close to linear with N_p[49].

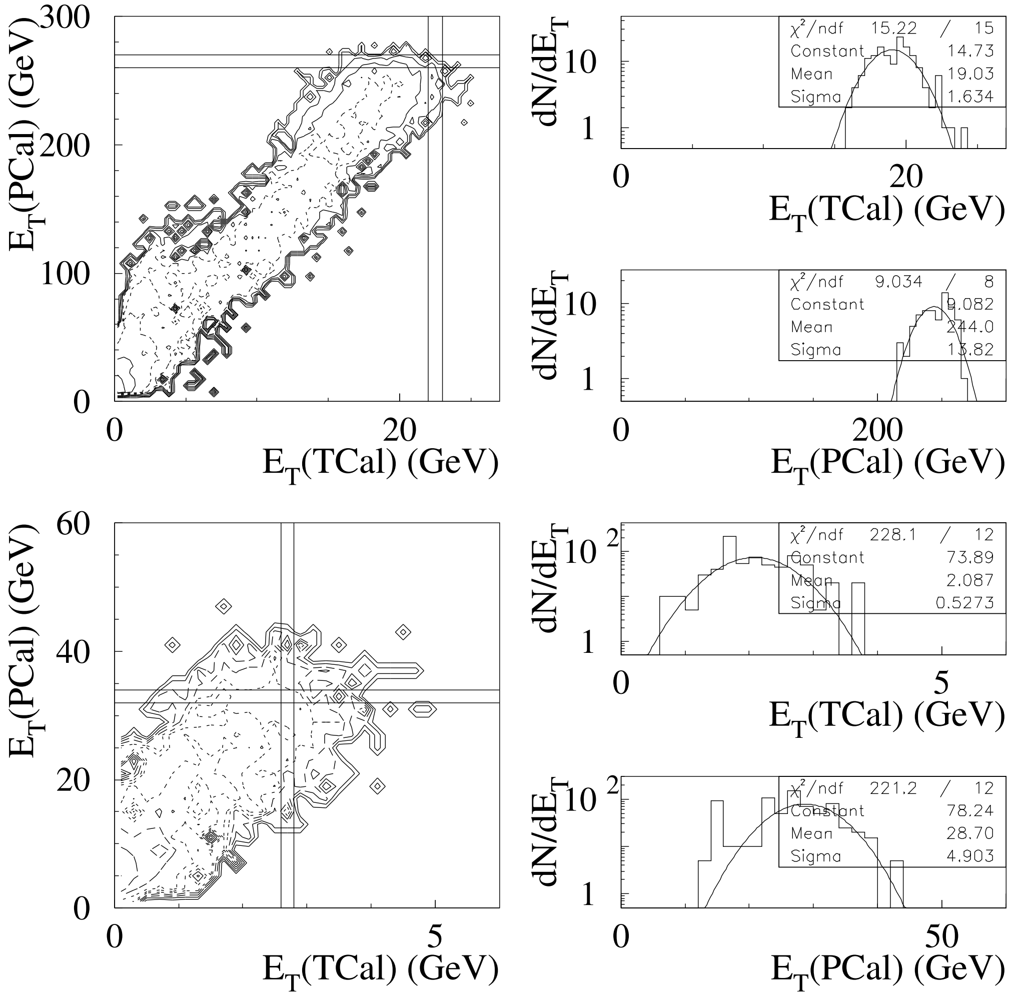

Figure 4.4: Correlation between TCAL E_T and PCAL E_T for the Si on Al (top 3 plots), and Au on Au (bottom) collision systems. The 1-D histograms are the projections of the 2-D histograms cutting on the other variable in the marked bands.

Table 4.1: Mean and standard deviation of E_T distribution for central Si on Al, and Au on Au collisions

	Si + Al		Au + Au	
	TCAL	PCAL	TCAL	PCAL
$\langle E_T^{\max} \rangle$ (GeV)	2.09	28.7	19.0	244
σ (GeV)	0.53	4.9	1.63	13.8
$\langle E_T^{\max} \rangle / \sigma$	3.94	5.86	11.7	17.7
N_p	55		394	
$\sqrt{N_p}$	7.4		19.8	

other possibilities that cannot be excluded entirely at this point. There is an uncertainty in the procedure of the bands selection and projection. The ratio $\langle E_T^{\mathrm{PCmax}} \rangle$ (Au+Au) / $\langle E_T^{\mathrm{PCmax}} \rangle$ (Si+Al) = 8.5 is actually 8% larger than 7.9, obtained by taking the ratio of E_T^0 (see Sec. 4.1.1 and Ref. [14]). This will reduce the above 10% discrepancy to a negligible value (2%). The reason that $\langle E_T^{\max} \rangle$ tends to be larger than E_T^0 may lie in the fact that the correlation between two global variables could be narrower than the correlation between impact parameter and each one of them. For example, two perfect calorimeters covering 2π solid angle backward and forward of mid-rapidity could give a very narrow correlation due to energy and momentum conservation.

Zero degree energy E_z and its correlation with E_T or N_c:

Zero degree energy (E_z) has long been used to evaluate the centrality of the collisions in many heavy ion experiments, *e. g.*, by the E802 collaboration at the AGS, and the WA80 collaboration [58] at the SPS. Fig. 4.5 shows sketch of two collision systems in the laboratory frame at a finite impact parameter. The part of the beam nucleus not shadowed by the target is called beam spectator. It will move approximately straight to zero degrees and deposit in a calorimeter at zero degree an energy $E_z \simeq N_z \cdot (\epsilon_b - m_u)$, where N_z is the number of nucleons in the beam spectator, and ϵ_b is the beam energy per nucleon. If a smaller beam (with radius R_b) collides with a larger target ($R_t > R_b$), there will be no beam spectator presented for $b < R_t - R_b$ (see Si + Au in Fig. 4.5). This corresponds to a fraction $(R_t - R_b)^2/(R_t + R_b)^2$ of total geometric cross section, which is about 10% for Si on Au or Pb. For a symmetric system (or a larger beam impinging on a smaller target), the non-zero N_z (except for symmetric head-on collisions) grows with b and E_z can be

Figure 4.5: Schematic drawings of Si on Au (left) and Au on Au (right) collisions at an impact parameter $b = 2$ fm. Beam spectators are present in the Au on Au collision, but not in Si on Au.

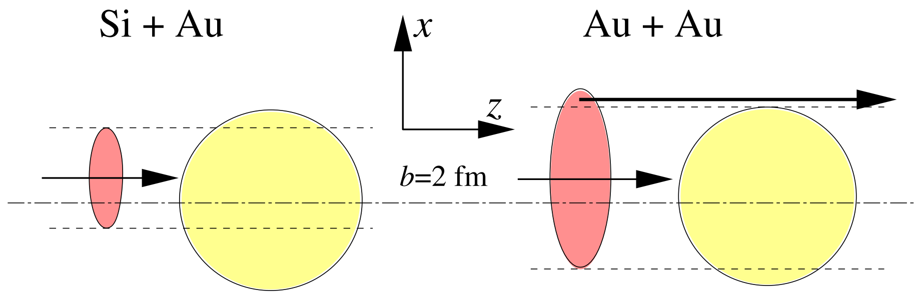

used to measure the impact parameter. This is illustrated in Fig. 4.6, where the cross section distribution of N_z is calculated for two collision systems in the sharp sphere geometric model as used in Fig. 4.3.

We now present the data, the E_z distribution, and its correlation with other global variables, either the charged particle multiplicity (N_c) measured by MULT, or the total transverse energy $E_T = E_T^{\mathrm{TCAL}} + E_T^{\mathrm{PCAL}}$. Figs. 4.7(a) and (b) show dN/dE_z for Si on Pb and Au on Au collisions; Fig. 4.7(c) and (d) display the double differential probability ($dN^2/dE_z dN_c$ and $dN^2/dE_z dE_T$) for Si on Pb and Au on Au. The peak structure in Fig. 4.7(a) around $E_z \simeq 0$ confirms what is shown schematically in Fig. 4.6(a), that is, the top 10% of the geometric cross section corresponds to events that have no beam spectators. On the other hand, the correlation in (c) shows a strong bending towards larger N_c for small E_z, indicating again the poor sensitivity of E_z on centrality for very central collisions. For Au on Au, however, the correlation shown in (d) is much narrower and shows good correlation between E_T and E_z for central collisions. This proves experimentally that E_z is indeed a sensitive variable to gate on centrality for a symmetric system such as Au on Au.

Multi-dimensional correlations between TCAL E_T, PCAL E_T, and UCAL E_z:

We present here the mean value of any one of these three variables as a function of the other two. The purpose of this study is to evaluate the sensitivity to the collision centrality for each of these variables in Au on Au collisions. Fig. 4.8 shows the contour and lego plots for $\langle E_z \rangle$ as a function of TCAL E_T (E_T^{TCAL}) and PCAL E_T (E_T^{PCAL}), $\langle E_T^{\mathrm{TCAL}} \rangle$ as a function of E_T^{PCAL} and E_z, and $\langle E_T^{\mathrm{PCAL}} \rangle$ as a function of E_z and E_T^{TCAL}. Besides the isolated spikes, which are the result of the low statistics in certain region of phase space

Figure 4.6: The cross section $d\sigma/dN_z$, where N_z is the number of beam spectators from the same geometric model as used in Fig. 4.3, for $R_b = 0.5R_t$ (a), and $R_b = R_t$ (b).

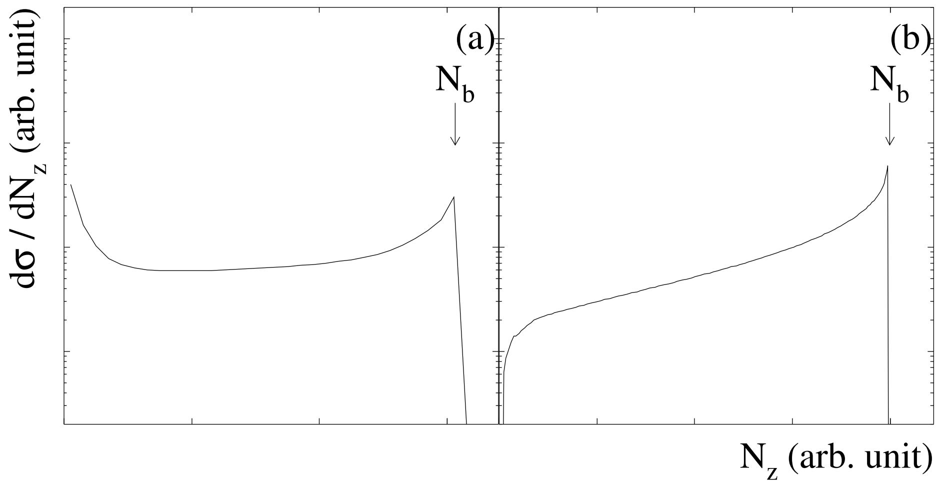

and should be disregarded, the overall shapes reveal a smooth correlation. In both the top and the bottom plots, the contour lines run nearly perpendicular to the $E_T^{\rm PCAL}$ axis for some interval indicating that $E_T^{\rm PCAL}$ is the most sensitive to centrality among them. In the middle plots, the $\langle E_T^{\rm PCAL}\rangle$ contour lines depend on both of the other variables, but change slope such that E_z shows more sensitivity for the most central events. We learned from this study that, due to the acceptance and response of the detectors used, PCAL E_T is the most favorable quantity in determining the centrality. TCAL E_T and UCAL E_z are compatible, but the latter performs better for higher centrality.

4.2 The Longitudinal Distribution

So far, we have presented the inclusive E_T measurement. Now, we turn to the question of how the energy is distributed within the full solid angle. In this section, we discuss the longitudinal distribution, namely, $dE_T/d\eta$. A correction for the energy leakage out of TCAL is considered in order to get the primary $dE_T/d\eta$ spectra from the measured data. The final corrected distributions are combined with response unfolded $dE_T/d\eta$ spectra from PCAL to give the complete pseudorapidity distributions, which are then compared with model calculations. From now on, we will only discuss the Au on Au system.

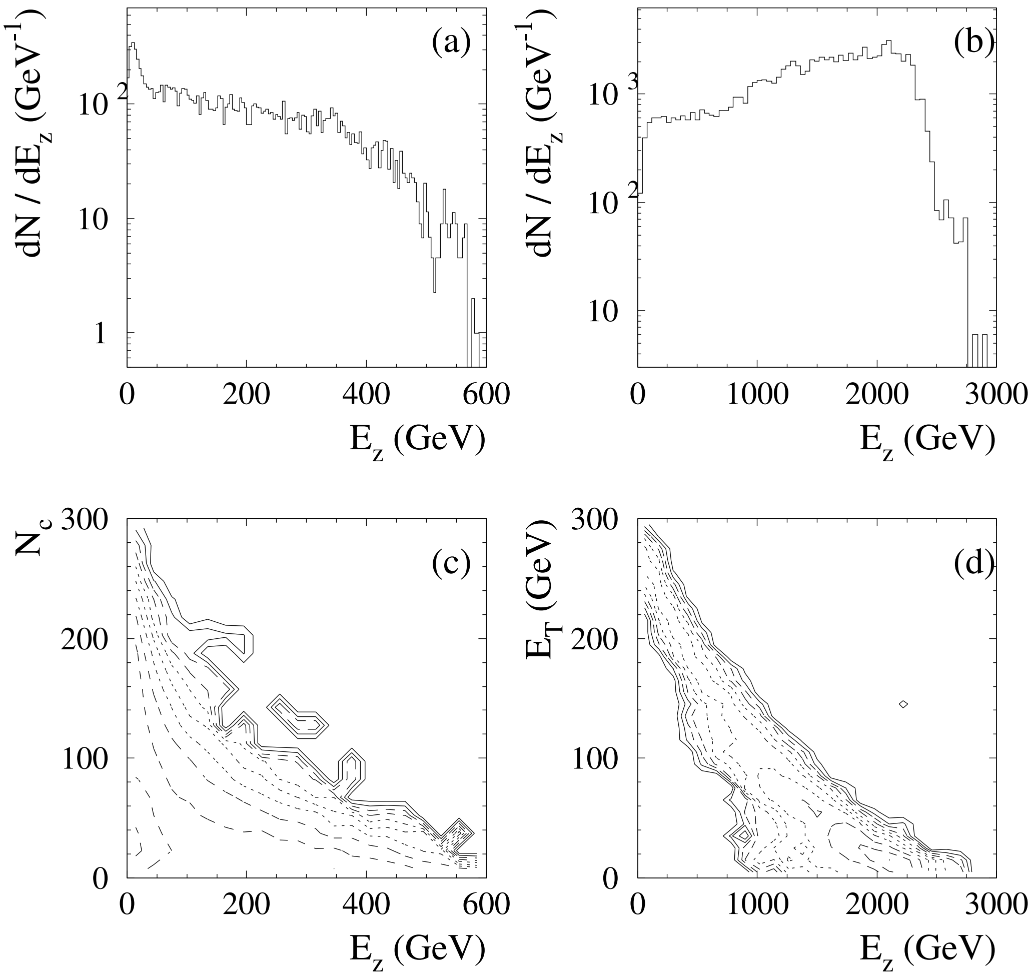

Figure 4.7: The E_z distribution (top) and its correlation with other variables (bottom). Here E_T is the sum of transverse energy measured in TCAL and PCAL. The results are shown for Si on Pb on the left in (a) and (c), and for Au on Au on the right in (b) and (d).

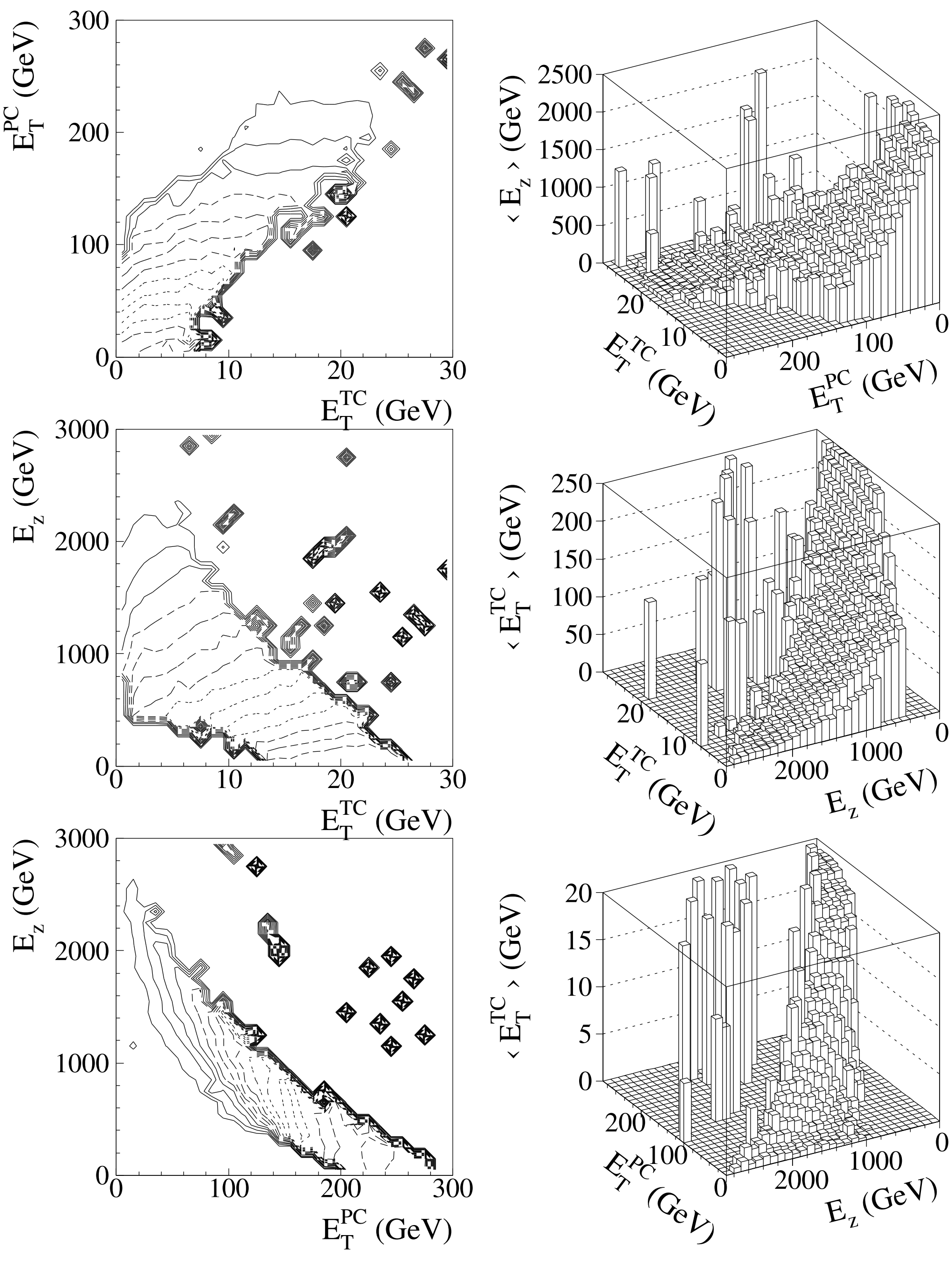

Figure 4.8: Contour (left) and lego (right) plots of $\langle E_z \rangle$ as a function of E_T^{TCAL} and E_T^{PCAL} (top), $\langle E_T^{\mathrm{PCAL}} \rangle$ as a function of E_T^{TCAL} and E_z (middle), and $\langle E_T^{\mathrm{TCAL}} \rangle$ as a function of E_T^{PCAL} and E_z (bottom).

4.2.1 The correction for energy leakage out of the target calorimeter

Waters [51] made extensive simulations for the TCAL with the tracking program GEANT[59]. Based on her work and the E814/E877 GEANT 3.13 framework, an event generator, HIJET [60], which is a super-position of *pp* collision from ISAJET [61], was used to study the detector's response for Au on Au collisions. We generated 16 k minimum-bias events and 8 k events with impact parameter $b < 7.5$ fm, and performed a full shower simulation through all 832 NaI crystals of TCAL. Energy deposition in each crystal is recorded, and the analysis was done the same way as for the data. The main result of the study is summarized in Fig. 4.9. The primary transverse energy from the HIJET into the TCAL acceptance ($E_T^{\rm prim}$) is plotted against the measured transverse energy ($E_T^{\rm meas}$) in (a), while (b) shows the projection of (a) to the horizontal axis, which is the differential cross section $d\sigma/dE_T$meas. Also shown in (b) is the measurement from the experimental data. HIJET over predicts E_T into TCAL acceptance by 30%. We go back to (a) to study the leakage factor. The solid line in (a) has a slope of 2, indicating that the global leakage correction factor integrating over the whole calorimeter is about 2.0 for Au on Au collisions, which is close to the factor 2.07 obtained using HIJET for the Si on Pb collisions [51]. However, the correction factor is not uniform over the pseudorapidity range, and we define a pseudorapidity dependent correction factor as C_η. Fig. 4.9(d) shows C_η as a function of η, which is obtained by taking the ratio of the primary and the measured $dE_T/d\eta$ spectra as shown in (c). These correction factors C_η are obtained for seven bins in measured E_T in TCAL from 0 to 28 GeV (4 GeV bin size). Fig. 4.9(d) shows the result for one bin (20 — 24 GeV), the shapes of C_η in other bins are very similar, with a 10% bin to bin variation in the absolute values. Similar studies done with other models, including FRITIOF [62], ARC [63], and RQMD [64] all give similar results. The differences between models in the same $E_T^{\rm meas}$ bin are within 10%, and contribute to a systematic error in the corrected pseudorapidity distributions. We use C_η from HIJET for the data analysis in the next chapter due to the high statistics.

4.2.2 The transverse energy pseudorapidity distributions

Fig. 4.10 shows the measured and the leakage corrected $dE_T/d\eta$ spectra from TCAL for Au on Au collisions. Table 4.2 lists the bins in the measured E_T for the analysis and an approximate measure of the impact parameter

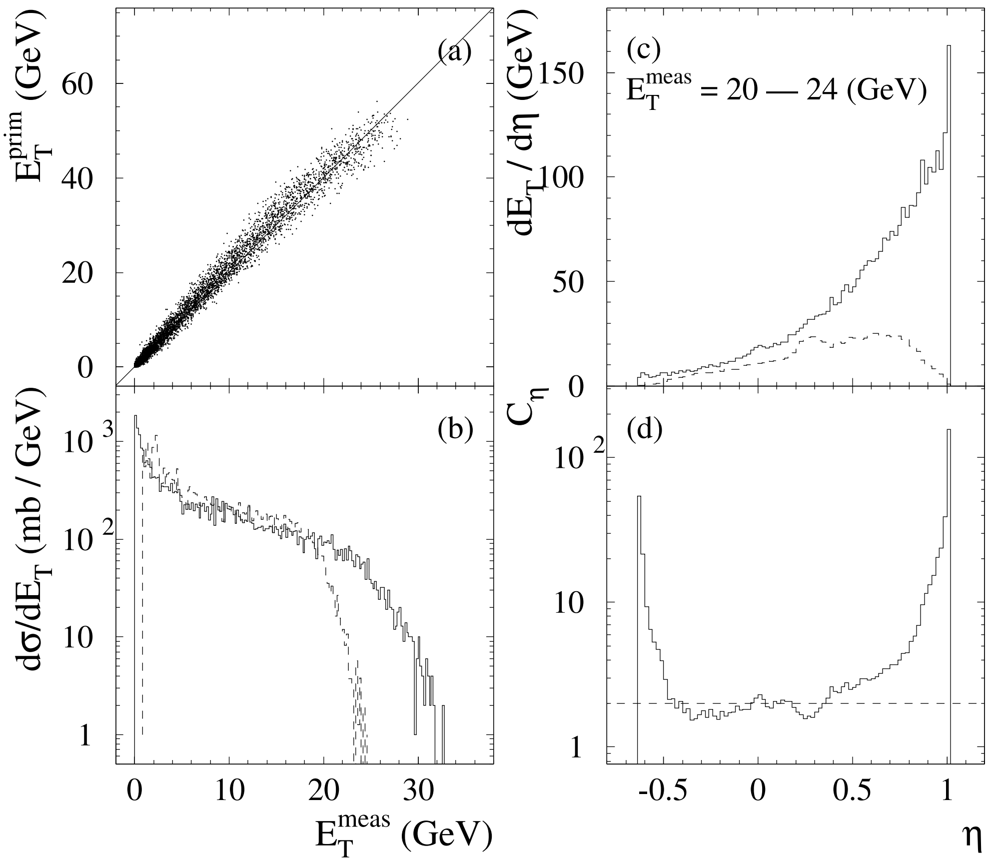

Figure 4.9: TCAL GEANT study with the HIJET event generator. (a) The primary versus the measured E_T in the TCAL acceptance for minimum-bias events. (b) $d\sigma/dE_T$ spectra of the measured E_T from HIJET (solid line), and from experimental data (dashed line). (c) The primary (solid line) and the measured (dashed line) $dE_T/d\eta$ spectra from HIJET, and (d) the energy leakage factor C_η from the ratio of the two spectra in (c). The dashed line in (c) indicates a constant leakage factor of 2. The centrality bin for (c) and (d) is indicated in (c).

Table 4.2: TCAL E_T bins for pseudorapidity distributions.

TCAL E_T bin (GeV)	4–8	8–12	12–16	16–20	20–24	¿24
TCAL $\langle E_T \rangle$ (GeV)	5.8	9.9	14.3	17.8	21.1	25.2
b (fm)	9.2	7.1	5.0	3.0	1.0	0.5
PCAL $\langle E_T \rangle$ (GeV)	70	125	180	230	260	270

obtained from simple geometric considerations as shown in Fig. 4.1(b). The measured $dE_T/d\eta$ spectra have already been corrected for contributions other than from the target by using data from the empty target (MT) runs,

$$E_T(\eta) = \frac{\sum_i^N E_T^i(\eta) - \sum_i^{N^{MT}} E_{TM}^i(\eta)}{N - N^{MT}}, \tag{4.5}$$

where N and N^{MT} are number of events with target and without (MT) properly normalized to beam counts. The measured $dE_T/d\eta$ in each E_T bin is then divided by the leakage correction factor C_η in the same bin to give the leakage corrected $dE_T/d\eta$.

The shape of the leakage corrected $dE_T/d\eta$ spectra (solid lines in Fig. 4.10) shows a systematic change as a function of centrality, *i. e.*, more energies is deposited into the higher η region in higher E_T bins. This observation indicates that the overall $dE_T/d\eta$ spectra get narrow for higher centralities, since we measure $dE_T/d\eta$ in the backward hemisphere for a symmetric system. [3] The structure around $\eta \simeq 0.25$ in both the uncorrected data and GEANT simulation (dashed line in Fig. 4.9(b)) is due to the wedge-shaped crystals located at $\theta \simeq 75°$ (see the side-view of TCAL in Fig. 3.3).

The analysis from PCAL shows that the data are consistent with a simple Gaussian distribution for $dE_T/d\eta$ [52]. The centroid of the Gaussian is very close to $\eta^c = 1.70$ independent of centrality for Au on Au collisions, and the widths (σ_η) varies from 1.15 for peripheral events to 0.75 for the most central events. The $dE_T/d\eta$ spectra from TCAL and PCAL for the same centralities (see Table 4.2) are plotted together in Fig. 4.11. They agree very well with each other at the point where they meet ($\eta \simeq 0.9$), and the TCAL data nicely follow the Gaussian extrapolation from PCAL. The results from HIJET are

[3] In asymmetric collisions the overall $dE_T/d\eta$ spectra also shift as a function of centrality due to kinematics.

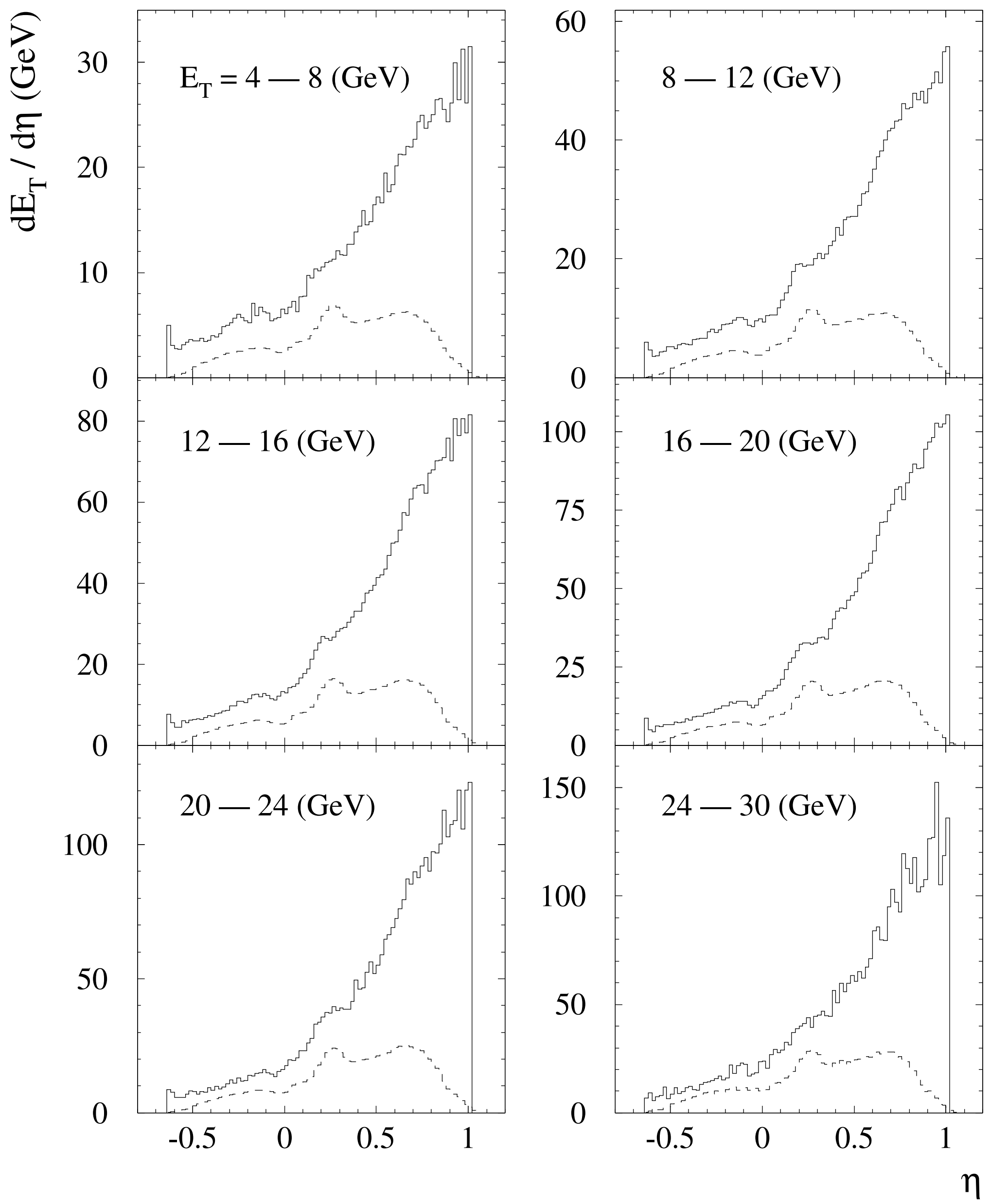

Figure 4.10: The measured and corrected $dE_T/d\eta$ spectra from TCAL for the Au target. The dashed lines are the measured data; the solid lines are corrected with the leakage factors from GEANT using the event generator HIJET.

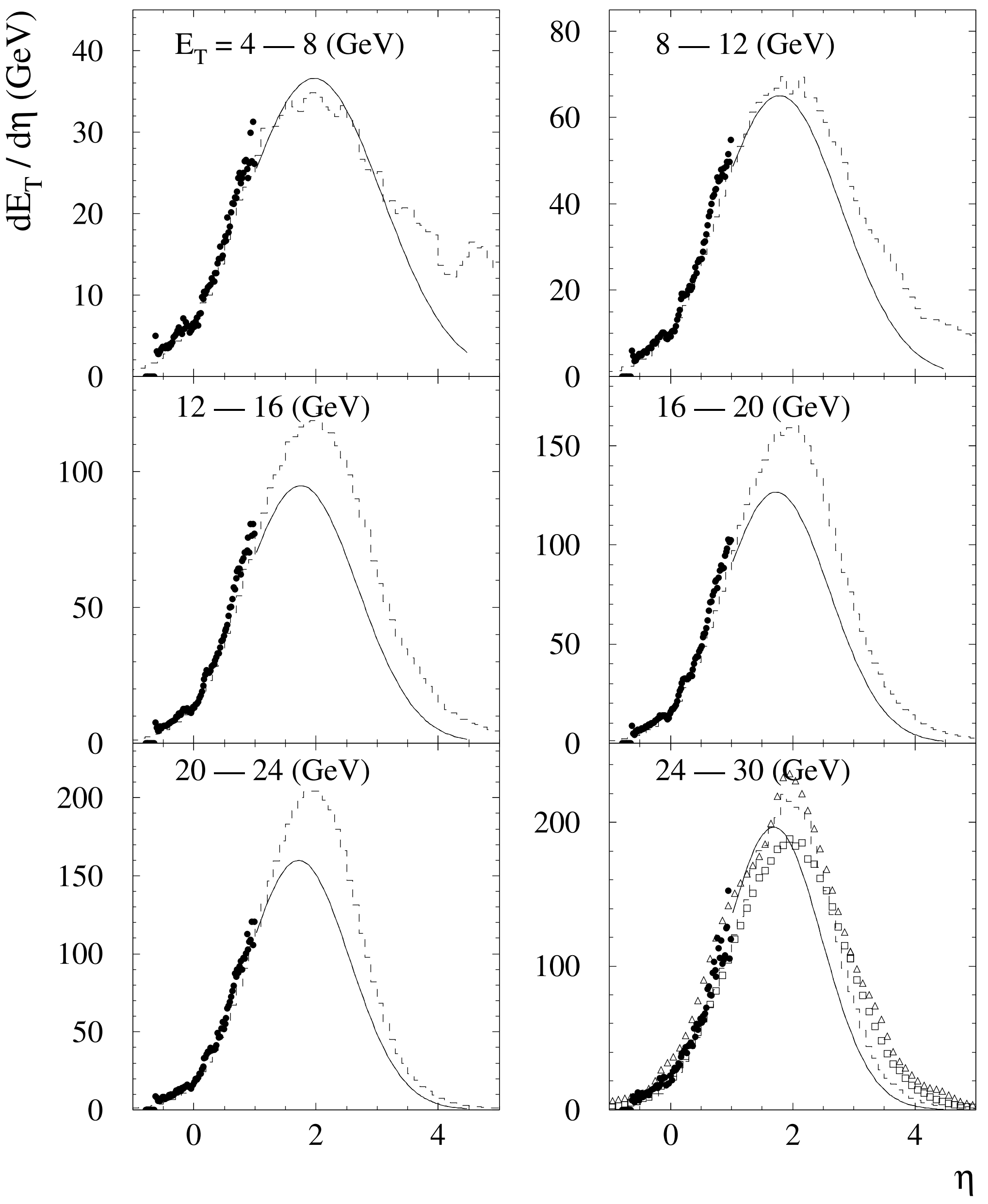

Figure 4.11: The leakage corrected $dE_T/d\eta$ spectra from TCAL (solid circles) and PCAL (solid lines). The primary spectra from HIJET (dashed lines) are shown in different centrality bins. Model calculations from ARC (triangles) and RQMD (squares) are shown in the highest E_T bin.

Table 4.3: The centroids and widths of Gaussian fits to $dE_T/d\eta$ spectra of data, HIJET, ARC, and RQMD.

	Data	HIJET	ARC	RQMD
η^c	1.70	1.85	1.93	1.88
σ_η	0.75	0.83	0.95	0.99

compared with the data in every centrality bin. It is apparent that HIJET over predicts the overall E_T production when requiring TCAL E_T to agree with the data. Also shown in the highest centrality bin are the calculations from ARC and RQMD. Spectra from all models are more forward peaked and wider than the data. The centroids and widths of Gaussian fits to all the models in the highest centrality bin are listed in Table 4.3. It is surprising that these sophisticated models, which successfully reproduce many aspects of spectra of identified particles fail to better reproduced the global observable that integrates all the information from identified particles, and the reason is not yet clear.

4.3 The Azimuthal Distributions

We now turn to the central part of this thesis – the analysis of the azimuthal distributions of the transverse energy. The main results of this analysis have been summarized in Ref. [65], where we demonstrate the observation of anisotropic event shapes and directed sideward flow for the first time in ultra-relativistic heavy ion collisions. This section will present the data analysis in detail. We first discuss the performance of our detectors, TCAL and PCAL, on an individual channel basis. The azimuthal analysis is presented in Sec. 4.3.2, there we emphasize a special correction procedure which is necessary due to lack of perfect azimuthal symmetry in the geometry and response of detectors. The fitting procedure and the results are given in Sec. 4.3.3. Azimuthal correlations between different pseudorapidity are presented in Sec. 4.3.4. Finally, in Sec. 4.3.5, the interpretation of the fit parameters is addressed.

4.3.1 The azimuthal gain equalization

The goal of the analysis was to detect the azimuthal anisotropy to the level of a few percent. To achieve this, the azimuthal response of our principal

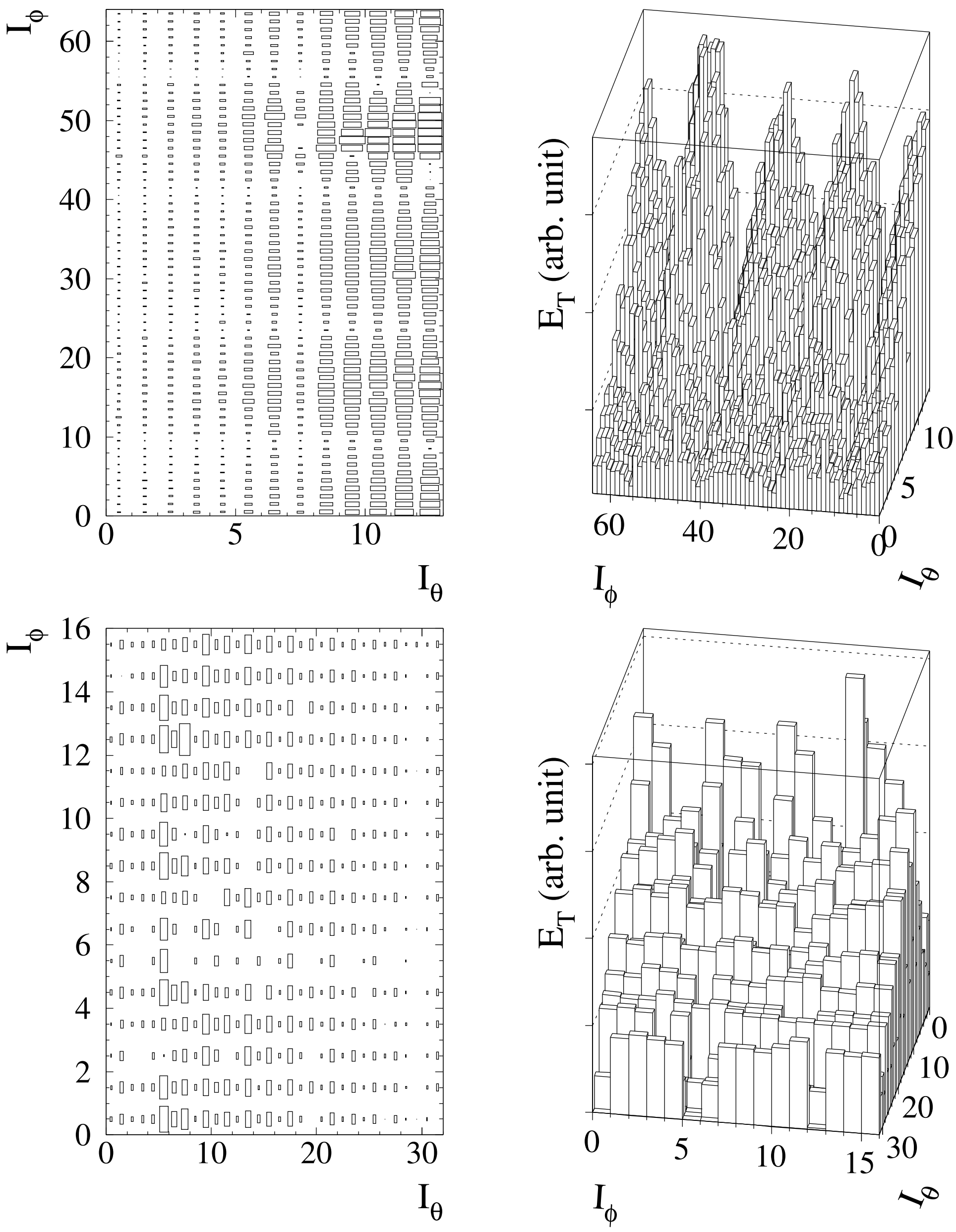

Figure 4.12: Averaged energy deposition in each channel of the TCAL (top) and PCAL (bottom) for $100 < E_T < 300$ GeV. The size of the boxes (left plots) is proportional to the averaged energy measured in that channel.

Table 4.4: List of problematic channels in PCAL

dead	I_z	1	1	1	1	1	1	1	1	1	1	1	1	1	1	1
	I_r	1	1	1	2	2	3	3	3	4	4	5	5	5	6	7
	I_ϕ	3	6	7	6	7	3	6	7	6	7	1	3	6	6	6
	I_z	1	1	1	1	1	2	2	2	2	2	2	2	2	2	2
	I_r	7	8	8	8	8	1	1	2	3	4	4	4	5	5	6
	I_ϕ	7	1	6	7	13	3	6	6	8	5	7	11	6	14	6
	I_z	2	2	2	3	3	3	3	3	3	3	3	3	3	4	
	I_r	6	7	8	1	3	3	4	4	4	4	4	8	8	7	
	I_ϕ	10	6	6	15	6	8	6	9	10	11	12	6	16	5	
bad gain	I_z	1	1	1	2	2	2	3								
	I_r	2	3	7	7	7	4	2								
	I_ϕ	10	10	4	4	1	2	3								
	G	4	6	2	3	8	2	10								

detectors, PCAL and TCAL, has to be uniform. Fig. 4.12 shows the energy deposition in each individual channel averaged over all events that fell into the $100 < E_T^{\mathrm{PCAL}} < 300$ GeV bin. If the sizes $\Delta\eta$ and $\Delta\phi$ of each cell are the same, these plots are equivalent to $d^2E/d\phi d\eta$, in which case a flat azimuthal (ϕ) distribution is expected for every η bin (θ). In our case, the geometry of TCAL and PCAL produces a pattern of regular structure in the energy distributions along the I_ϕ axes.[4] Smooth distributions are expected if every channel is gain equalized properly. Individual bad channels were identified if their energy level differs largely from the neighboring channels. For these channels, an inverse ratio between their energy level to the averaged energy level of the azimuthal neighboring channels is defined as "gain factor" (G). We call a channel "dead" if $G > 20$, and in this case it is excluded from the data analysis. Only a few such channels were found in TCAL, while forty-four of them were found in PCAL, listed in Table 4.4. If a gain factor of a channel falls in $0 < G < 20$, it is called "bad gain". Seven channels with "bad gain" were found, and were restored to normal energy level by multiplying the original energy with G (see Table 4.4). If a large number azimuthal neighboring channels were found "dead", all channels in this azimuthal ring were removed

[4] I_ϕ is the index number in azimuth. I_ϕ=1—64 for TCAL, and 1—16 for PCAL. I_θ is the index number in polar angle, with I_θ=1—13 for TCAL, and 1—32 for PCAL for the 8 polar angles in each of the 4 depth sections.

Table 4.5: Centrality bins selected by the PCAL E_T, the corresponding impact parameters, the mean E_T in the three pseudorapidity intervals, and the magnitude of the MT subtraction.

PCAL E_T bin (GeV)	$\langle E_T \rangle \pm r.m.s.$ (GeV)	b (fm)	$\langle E_T \rangle \pm r.m.s.$ (GeV) in three η intervals			MT %
			$(-0.5, 0.8)$	$(0.83, 1.85)$	$(1.85, 4.7)$	
$40 - 60$	48.8 ± 5.7	10.15	3.24 ± 1.52	14.6 ± 3.9	32.8 ± 4.6	63
$60 - 80$	69.5 ± 5.8	9.13	5.21 ± 1.77	23.2 ± 4.9	44.3 ± 5.0	49
$80 - 100$	89.8 ± 5.8	8.40	7.10 ± 1.78	32.2 ± 5.3	55.0 ± 5.3	39
$100 - 120$	109.7 ± 5.8	7.66	8.79 ± 1.82	41.5 ± 5.2	65.0 ± 5.4	25
$120 - 140$	129.8 ± 5.7	6.95	10.51 ± 1.87	51.1 ± 5.5	74.7 ± 5.5	13.5
$140 - 160$	149.9 ± 5.9	6.26	12.09 ± 1.86	61.1 ± 5.6	84.2 ± 5.4	3.2
$160 - 180$	169.8 ± 5.8	5.56	13.63 ± 1.91	71.5 ± 5.6	92.8 ± 5.2	1.6
$180 - 200$	189.8 ± 5.7	4.60	15.18 ± 1.94	82.5 ± 5.9	101.0 ± 5.2	1.3
$200 - 220$	211.2 ± 5.6	3.79	16.75 ± 1.91	94.6 ± 5.8	109.5 ± 4.9	0.04
$220 - 240$	229.7 ± 5.8	2.89	18.03 ± 1.91	106.3 ± 5.9	115.5 ± 4.8	0.01
$240 - 260$	248.9 ± 5.6	1.72	19.08 ± 1.82	119.0 ± 5.9	121.1 ± 4.5	0.03
$260 - 280$	265.0 ± 4.3	0.57	19.40 ± 1.67	130.4 ± 5.3	125.1 ± 4.3	0.00

from the analysis. Two cases were found like this. In the ring of $I_z = 3$ of the PCAL (HAD1) and $I_r = 4$, there are four consecutive dead channels (I_ϕ=9—12). To preserve the azimuthal symmetry, all channels in this ring ($I_z = 3$, $I_r = 4$, and I_ϕ =1—16) were removed from the analysis.

After these procedures, there still exists azimuthal asymmetry in our detectors, due to geometry and channels removed from the analysis, and a further correction has to be made to the constructed Fourier coefficients.

4.3.2 The global correction of the Fourier coefficients

From our discussion in Chapter 2, it was clear that narrow centrality bins are crucial to the success of the Fourier analysis of the azimuthal E_T distributions. The bin size should be chosen to be as narrow as is allowed by the statistics. In this analysis, PCAL E_T was used to sort events into 12 bins, each 20 GeV wide, from 40 to 280 GeV. The width of the pseudorapidity intervals also has to be chosen such that the multiplicity (M) is large enough in each of the intervals. In an initial study, it is safer to have wider η intervals. The detailed η dependence will be lost for wider intervals, but the sensitivity to the azimuthal asymmetry will be enhanced. Following these considerations, we decided to cut the entire η acceptance into three windows. The whole TCAL was chosen as the backward window ($-0.5 < \eta^b < 0.8$). PCAL was cut into two parts, the middle window ($0.83 < \eta^m < 1.85$), and the forward window ($1.85 < \eta^f < 4.7$). Table 4.5 summarizes our choices for the centrality bins and the η windows. The mean E_T in each η window from the data is given, and will be used our discussion later. Also listed in the table are the centralities for each bin, and the percentage of the background subtraction from the empty target frame measurement.

For each event, Fourier coefficients x_n, y_n (up to $n = 4$) were calculated according to

$$x_n = \sum_\nu \epsilon_\nu \cos(n\phi_\nu)/\sum_\nu \epsilon_\nu, \tag{4.6}$$

$$y_n = \sum_\nu \epsilon_\nu \sin(n\phi_\nu)/\sum_\nu \epsilon_\nu, \tag{4.7}$$

which differ from Eq. (2.24-2.25) only by a normalization factor, $E_T = \sum_\nu \epsilon_\nu$. The index ν in Eq. (2.24-2.25) runs over all particles in a given rapidity window, while here ν is the index of the detector cells in the window. The results after summation would be the same for both cases. At the end of tape scanning, we obtained a twenty-seven dimensional array[5] for about 80,000 events from three PCAL E_T triggers.

Before we follow the procedure discussed in Chapter 2 to calculate the amplitude of the Fourier coefficients $v_n = \sqrt{x_n^2 + y_n^2}$, let us examine the 2-D distribution $d^2N/dx_n dy_n$. For a perfect detector, we expect a circular contour distribution around the origin, which results in a flat distribution in $dN/d(n\psi_n)$ ($n\psi_n = \arctan(y_n/x_n)$), since the reaction plane is randomly oriented around the beam axis. On the other hand, any azimuthal asymmetry in the detector will distort the $d^2N/dx_n dy_n$ distribution, and $dN/d(n\psi_n)$ will no longer be flat. If the distortions are small, they can be corrected safely by taking out the Fourier coefficients of the $dN/d(n\psi_n)$ distribution to flatten it on average. I call this procedure "global correction" since it is done not on an event-by-event basis, but on the event-averaged sample. Fig. 4.13 shows the "global correction" in two steps for $d^2N/dx_2^f dy_2^f$ (the second harmonic in the forward window η^f) in the E_T bin 200—220 GeV. Fig. 4.13 (a) and (b) shows the original 2-D and azimuthal distributions, in which a significant azimuthal asymmetry can be seen. In the first step, we find the mean value of the 2-D distribution,

[5]There are nine variables in each η window, four pairs of Fourier coefficients for $n = 1$—4, and a value for E_T.

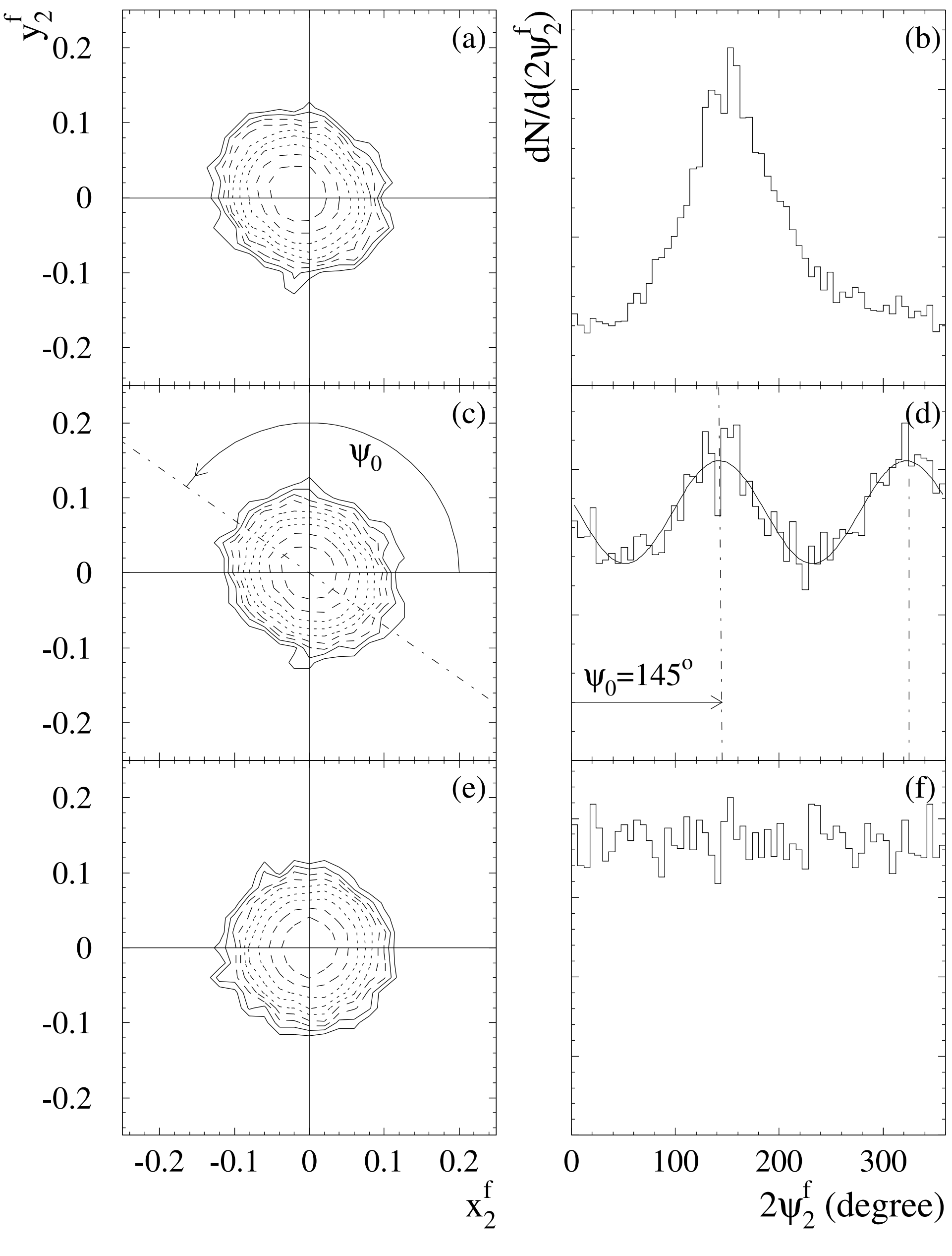

Figure 4.13: The 2-D and azimuthal distributions of the Fourier coefficients x_2^f and y_2^f. Both the raw (a, b) and corrected distributions (c—f) are shown to illustrate the correction procedure. See text for details.

$(\bar{x}_2, \bar{y}_2)$, and then shift the origin to this point (as shown in Fig. 4.13(c)). This effectively zeroes the first moment of the $dN/d(2\psi_2)$ distribution, but now a second moment becomes apparent in the new $dN/d(2\psi_2^f)$ distribution (shown in Fig. 4.13(d)). In the second step, we remove the second moment. We find the long axis of the 2-D distribution by fitting the distribution (d) with $1 + \gamma \cos[2(2\psi_2^f - \psi_0)]$, where ψ_0 is the orientation of the long axis (marked by the dashed-dotted lines in (c) and (d)), and then project the 2-D distribution onto the long and short axes to obtain the width of the distributions ($\sigma_l > \sigma_s$). Finally, we normalize the width to the average, $(\sigma_l + \sigma_s)/2$, which effectively squeezes the long axis and stretches the short axis, and thereby takes out the second moment. Figures (e) and (f) are the final 2-D and azimuthal distributions, where now azimuthal symmetry is restored. In principle, we can apply this procedure to higher moments of the $dN/d(2\psi_2)$ distribution, but since all the azimuthal distributions appear to be flat, we did not go beyond the second moment.

The same two-step global correction procedure was carried out for other harmonics, d^2N/dx_1dy_1, d^2N/dx_3dy_3, and d^2N/dx_4dy_4, and in every η window and centrality bin. Due to the many (10%) problematic channels in PCAL, this correction procedure is the most important step in the data analysis, without which it would not be possible to proceed further.

The corrected $d^2N/dx_1^f dy_1^f$ distributions for every centrality bin are shown in Fig. 4.14. A ring-shaped distribution with a minimum at the origin of the 2-D distributions is visible in the six of the mid-centrality bins (100—220 GeV). This observation proves the existence of the first harmonic anisotropy in the forward window; as discussed in Sec. 2.4, the minimum at the origin is a sufficient but not necessary condition, and would appear only if the condition $\tilde{v}_1^f/\sigma^f > \sqrt{2}$ is fulfilled. No such a minimum is observed for any other harmonics in all three η windows. But the anisotropy parameters can nevertheless be extracted with the simultaneous fitting procedure.

4.3.3 Fitting the data with anisotropy parameters

Distributions $dN/v_n dv_n$ in the three η windows and the twelve centrality bins were generated and fitted with Eq. (2.35). Each fit is done to all four distributions (n =1—4) simultaneously with four parameters, $\tilde{v}_n$ ($n = 1, 2, 4$) and σ. Since dN/v_3dv_3 always gives the narrowest Gaussian-like distribution consistent with $\tilde{v}_3 = 0$, we assume $\tilde{v}_3 = 0$ to reduce the number of free parameters. Since we have a symmetric collision system, we would also expect $\tilde{v}_3$ to be zero.

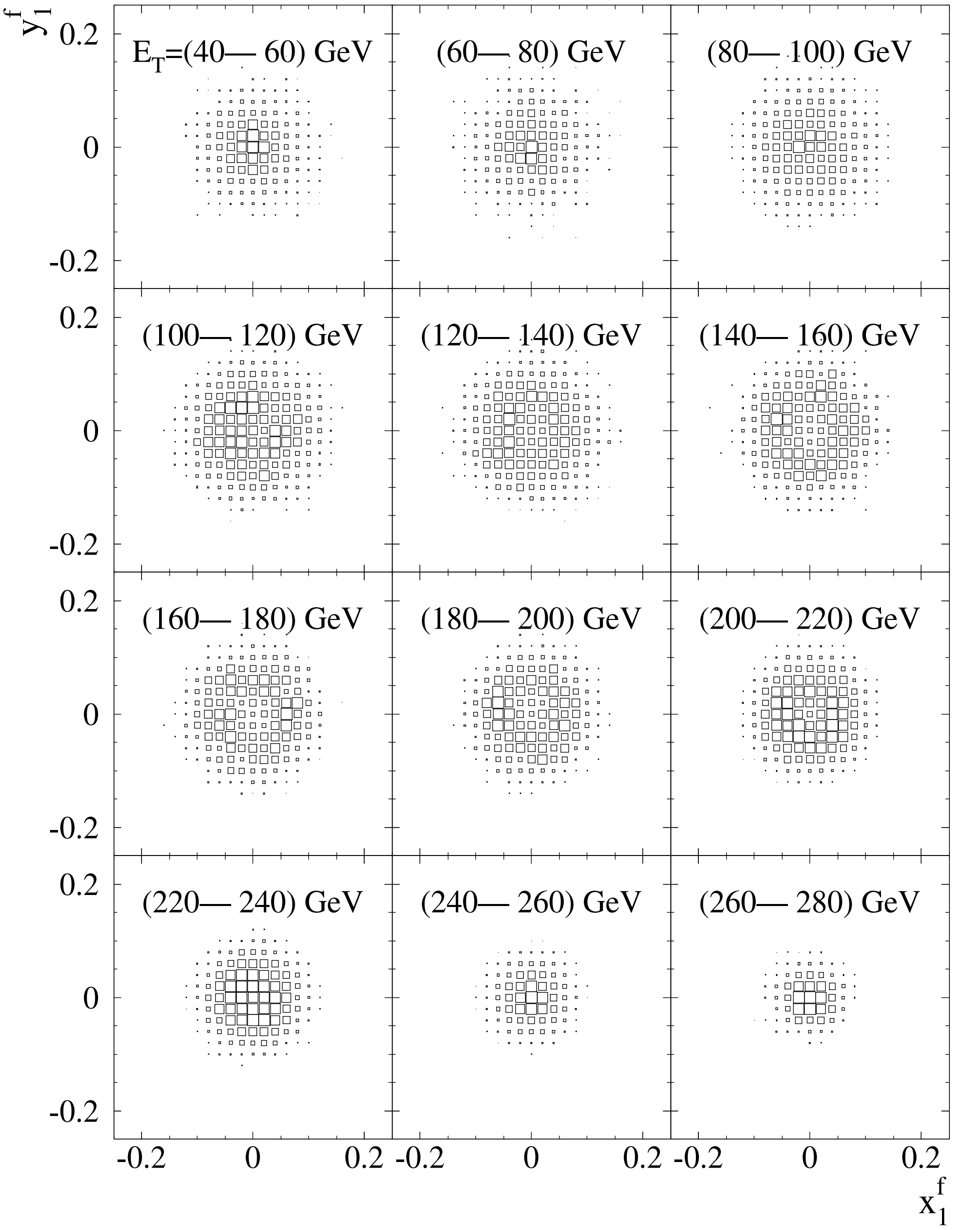

Figure 4.14: The corrected 2-D distributions $d^2N/dx_1^f dy_1^f$ for different centrality bins. The size of the boxes is proportional to the number of events with a given x_1^f, dy_1^f.

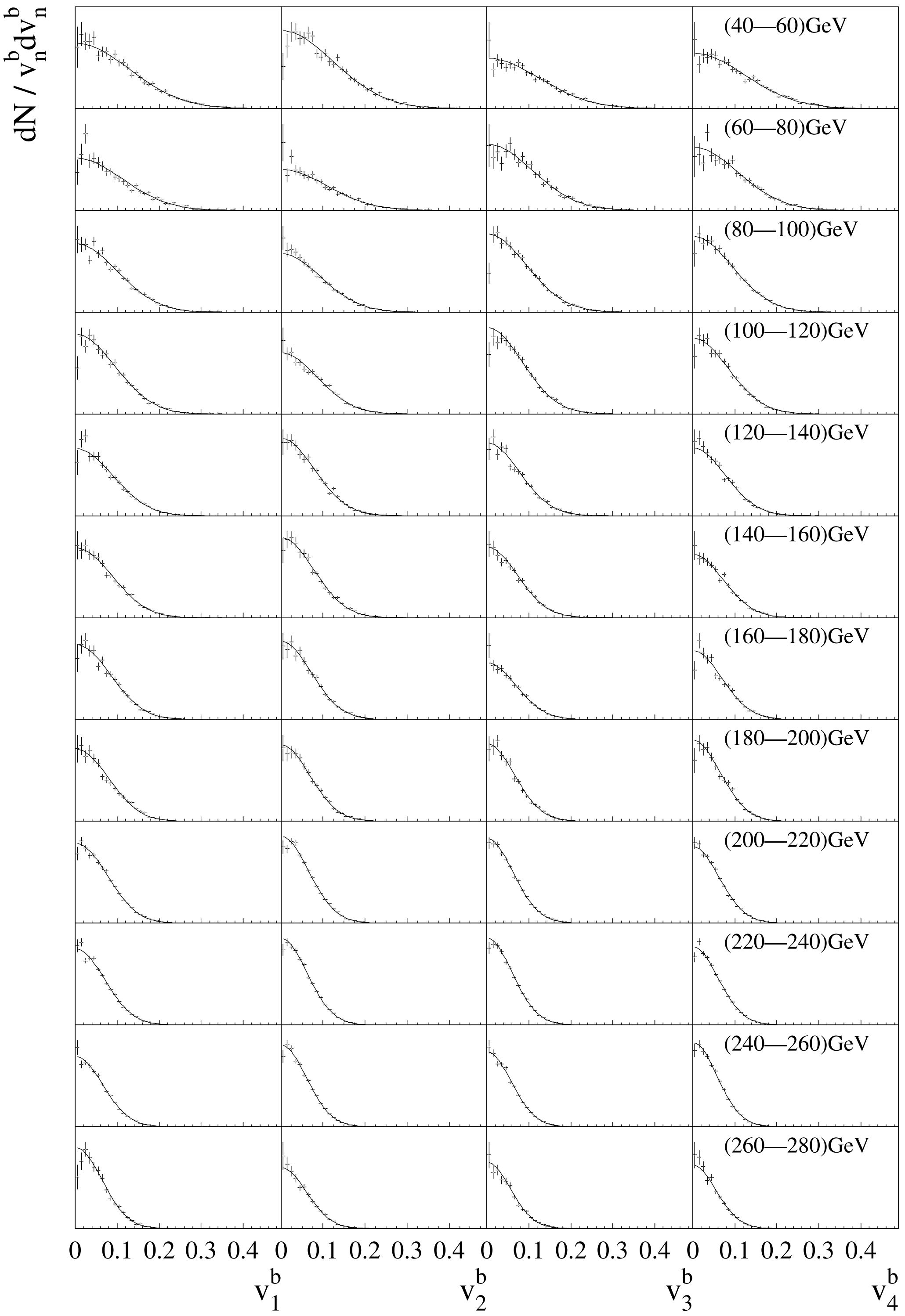

Figure 4.15: Distributions of the amplitude of the Fourier coefficients in η^b.

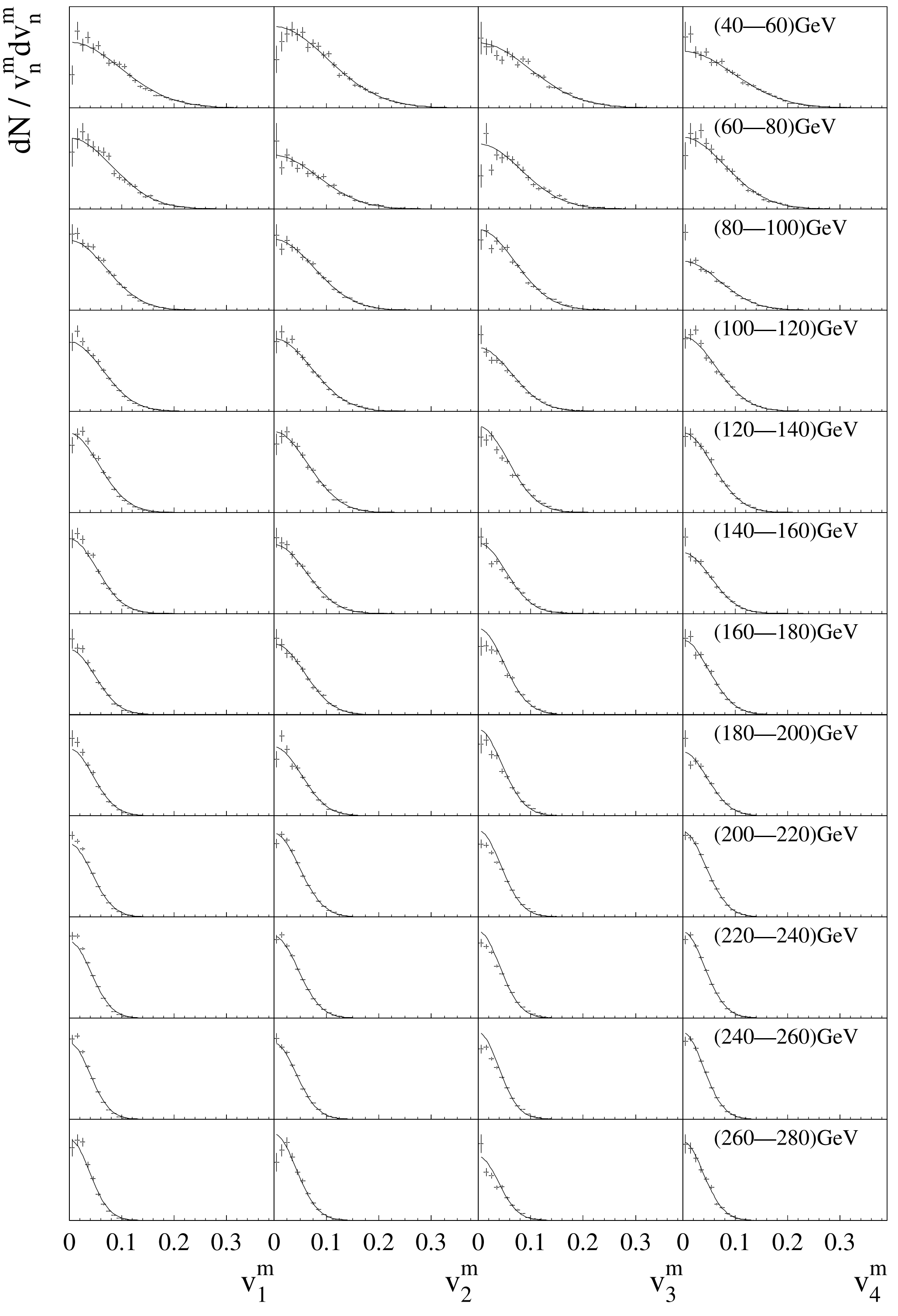

Figure 4.16: Distributions of the amplitude of the Fourier coefficients in η^m.

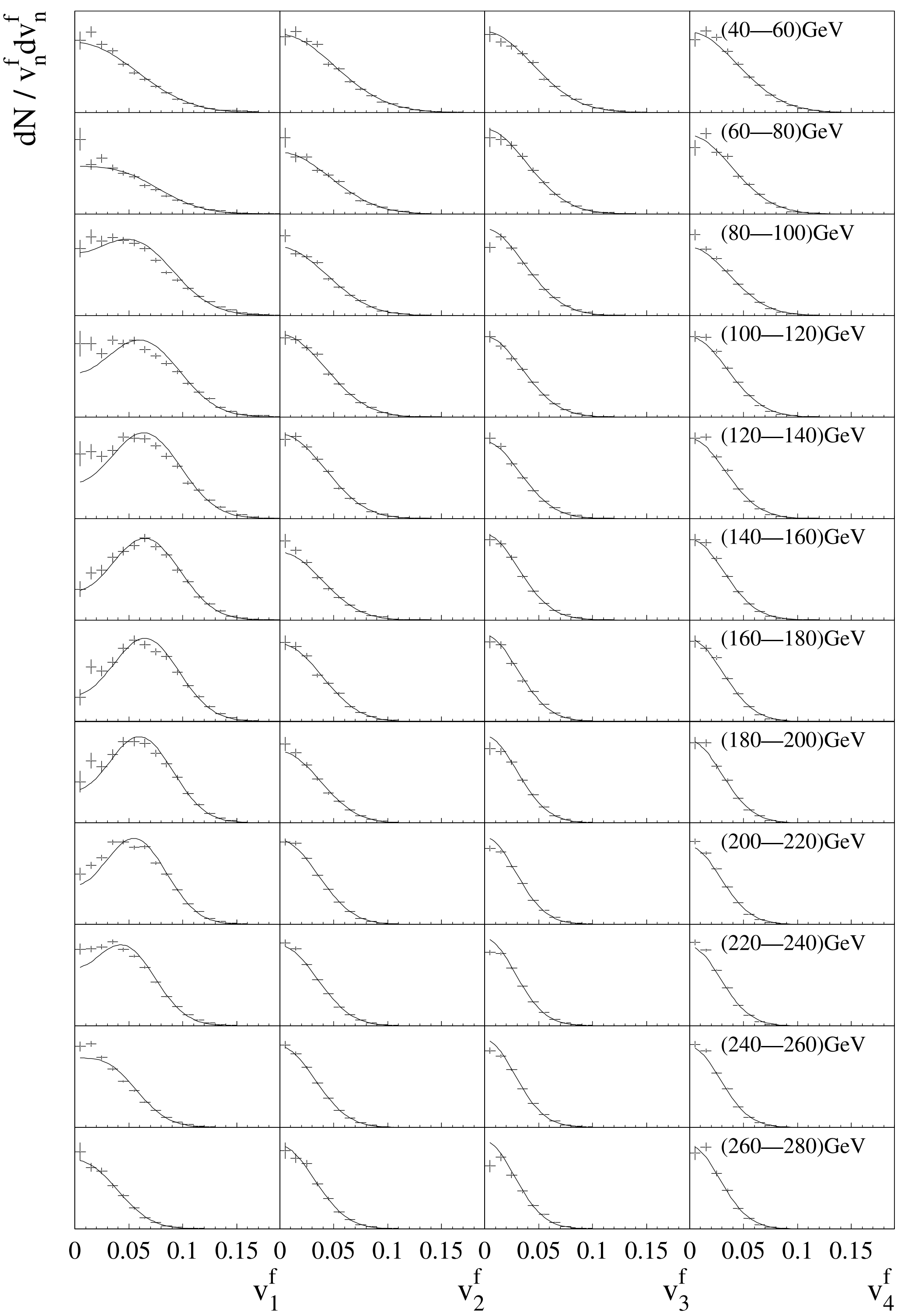

Figure 4.17: Distributions of the amplitude of the Fourier coefficients in η^f.

Table 4.6: Anisotropy and fluctuation parameters as a function of centrality, in the η^b window. Errors are statistical. The last column displays the reduced χ^2 of the fit.

E_T bin (GeV)	$\tilde{v}_1(\times 100)$	$\tilde{v}_2(\times 100)$	$\tilde{v}_4(\times 100)$	$\sigma(\times 100)$	χ^2
$40-60$	4.39 ± 0.70	0.03 ± 0.91	0.01 ± 0.65	12.42 ± 0.06	0.88
$60-80$	4.04 ± 0.62	2.86 ± 0.83	0.08 ± 2.56	10.74 ± 0.55	0.95
$80-100$	4.33 ± 0.35	1.40 ± 1.06	0.05 ± 1.12	9.35 ± 0.04	0.99
$100-120$	5.31 ± 0.27	2.69 ± 0.49	0.01 ± 0.56	8.37 ± 0.04	1.20
$120-140$	5.59 ± 0.24	2.62 ± 0.45	0.02 ± 0.56	7.66 ± 0.04	1.13
$140-160$	5.84 ± 0.22	3.63 ± 0.32	0.00 ± 0.20	7.22 ± 0.04	0.89
$160-180$	5.59 ± 0.22	2.72 ± 0.40	0.00 ± 0.61	6.86 ± 0.04	0.93
$180-200$	5.29 ± 0.21	2.70 ± 0.39	0.01 ± 0.34	6.51 ± 0.04	0.91
$200-220$	5.21 ± 0.10	2.83 ± 0.16	0.01 ± 0.09	6.19 ± 0.02	1.42
$220-240$	4.34 ± 0.10	1.93 ± 0.20	0.00 ± 0.23	5.99 ± 0.02	1.14
$240-260$	3.80 ± 0.12	2.29 ± 0.19	0.01 ± 0.19	5.76 ± 0.02	1.15
$260-280$	3.85 ± 0.26	3.04 ± 0.32	0.00 ± 0.01	5.54 ± 0.05	0.91

Figures 4.15, 4.16, and 4.17 display the distributions $dN/v_n dv_n$ for data and the fits to Eq. (2.35) in the three η windows. The fit parameters and the reduced χ^2 of each fit are listed in Tables 4.6, 4.7, and 4.8. The resulting statistical errors from the fit are shown as well. These numbers clearly show a large anisotropy of the first harmonic in both the backward and forward windows. We will discuss these fit parameters further in Sec. 4.3.5.

4.3.4 Azimuthal correlations

After the "global correction" described in Sec. 4.3.2, the azimuthal distributions $dN/d(n\psi_n)$ are flat for each harmonic, in every η window and E_T bin. However, as discussed in Chapter 2, we would expect a correlation event-by-event between the angles ψ_n in different η windows if flow is present in these windows. Fig. 4.18(a) shows the 2-D correlation between ψ_1^b and ψ_1^f in the PCAL E_T bin 200—220 GeV. The azimuthal distributions of all events in this E_T bin $dN/d\psi_1^f$ (b) and $dN/d\psi_1^b$ (c) are flat, but a strong correlation is seen both in the 2-D plot (a), where a valley lies in the diagonal direction ($\psi_1^b = \psi_1^f$), and in the distribution $dN/d\Delta\psi_1^{bf}$ ($\Delta\psi_1^{bf} \equiv \psi_1^b - \psi_1^f$), which peaks at 180°. It shows that the sideward flow in the backward and forward windows goes in the opposite direction. This correlation is found in all of the centrality

Table 4.7: Anisotropy and fluctuation parameters as a function of centrality, in the η^m window. Errors are statistical. The last column displays the reduced χ^2 of the fit.

E_T bin (GeV)	$\tilde{v}_1(\times 100)$	$\tilde{v}_2(\times 100)$	$\tilde{v}_4(\times 100)$	$\sigma(\times 100)$	χ^2
$40 - 60$	0.03 ± 0.87	4.06 ± 0.47	0.00 ± 1.67	9.73 ± 0.05	1.14
$60 - 80$	0.01 ± 1.24	2.93 ± 0.59	0.00 ± 1.00	8.08 ± 0.05	1.30
$80 - 100$	0.01 ± 0.30	4.15 ± 0.21	0.01 ± 2.83	6.91 ± 0.03	1.60
$100 - 120$	0.00 ± 0.28	4.28 ± 0.19	1.10 ± 0.68	6.18 ± 0.03	1.23
$120 - 140$	0.00 ± 0.36	4.03 ± 0.18	0.67 ± 0.94	5.58 ± 0.03	1.97
$140 - 160$	0.01 ± 0.22	4.00 ± 0.17	1.24 ± 0.47	5.15 ± 0.03	1.80
$160 - 180$	0.00 ± 0.13	3.84 ± 0.15	1.60 ± 0.34	4.76 ± 0.03	1.81
$180 - 200$	0.00 ± 0.61	3.30 ± 0.16	1.57 ± 0.30	4.42 ± 0.03	2.19
$200 - 220$	0.00 ± 0.26	2.84 ± 0.08	1.32 ± 0.16	4.21 ± 0.01	5.07
$220 - 240$	0.00 ± 0.08	2.64 ± 0.08	1.03 ± 0.18	4.02 ± 0.01	6.21
$240 - 260$	0.00 ± 0.11	2.24 ± 0.09	1.05 ± 0.18	3.84 ± 0.01	6.18
$260 - 280$	0.00 ± 0.23	2.39 ± 0.18	1.37 ± 0.32	3.76 ± 0.03	2.18

Table 4.8: Anisotropy and fluctuation parameters as a function of centrality, in the η^f window. Errors are statistical. The last column displays the reduced χ^2 of the fit.

E_T bin (GeV)	$\tilde{v}_1(\times 100)$	$\tilde{v}_2(\times 100)$	$\tilde{v}_4(\times 100)$	$\sigma(\times 100)$	χ^2
$40 - 60$	4.00 ± 0.12	3.09 ± 0.14	0.00 ± 0.14	4.37 ± 0.02	2.01
$60 - 80$	5.30 ± 0.12	3.03 ± 0.16	0.00 ± 0.31	3.86 ± 0.03	1.66
$80 - 100$	6.42 ± 0.07	2.82 ± 0.09	0.00 ± 0.23	3.61 ± 0.02	4.32
$100 - 120$	7.05 ± 0.07	2.83 ± 0.09	0.00 ± 0.36	3.41 ± 0.02	2.72
$120 - 140$	7.25 ± 0.07	2.90 ± 0.09	0.00 ± 0.17	3.21 ± 0.02	3.03
$140 - 160$	7.27 ± 0.06	2.65 ± 0.09	0.00 ± 0.69	3.10 ± 0.02	1.75
$160 - 180$	7.22 ± 0.07	2.67 ± 0.09	0.00 ± 0.06	3.00 ± 0.02	1.91
$180 - 200$	6.75 ± 0.07	2.56 ± 0.10	0.01 ± 0.16	2.92 ± 0.02	1.68
$200 - 220$	6.25 ± 0.03	2.38 ± 0.05	0.00 ± 0.20	2.83 ± 0.01	6.82
$220 - 240$	5.31 ± 0.03	2.28 ± 0.04	0.00 ± 0.06	2.80 ± 0.01	8.08
$240 - 260$	3.89 ± 0.04	2.00 ± 0.06	0.01 ± 0.07	2.77 ± 0.01	5.68
$260 - 280$	2.76 ± 0.10	1.97 ± 0.12	0.00 ± 0.08	2.74 ± 0.02	1.82

windows, as shown in Fig. 4.19, where $dN/d\Delta\psi_1^{bf}$ spectra are plotted for all twelve centrality bins. To quantify this correlation, we take the ratio

$$R = \frac{N(|\Delta\psi_1^{bf} - \pi| < \pi/2)}{N(|\Delta\psi_1^{bf} - \pi| > \pi/2)} \tag{4.8}$$

as indicated by differently shaded areas in Fig. 4.18(d). The ratio R depends strongly on the centrality, as shown in Fig. 4.20(a). It reaches its maximum for intermediate centrality, and approaches one (implying azimuthal isotropy in one or both windows) for peripheral and the most central collisions. On the other hand, assuming the observed correlation is only due to flow presented in the η^b and η^f windows (not due to other correlations, *e. g.*, momentum conservation), we could calculate the azimuthal correlation from Eq. (2.45) from the known anisotropy and fluctuation parameters, $\tilde{v}_1^b$, σ_b, $\tilde{v}_1^f$ and σ_f. The ratio R calculated using these parameters is also plotted in Fig. 4.20 (histogram). The good agreement between the measured and calculated R proves that the observed backward and forward correlation is entirely consistent with the extracted flow in the two windows. Another way to quantify the correlation is shown in Fig. 4.20, where (b) is plotted the r.m.s of the distribution in Fig. 4.19 (solid squares) and the same quantity from the calculation (solid histogram). The calculated reaction plane resolution from the backward (dotted line) and forward (dashed line) window is also shown. The dashed-dotted line is the r.m.s of a flat distribution between 0 and 2π. The best resolution is about 70° and 27° for the backward and forward window, respectively, and is found around mid-centrality.

The above discussion validates the more commonly used approach, *i. e.*, to determine the reaction plane from one detector (2π azimuthal coverage is required), and measure the particle distribution in another (2π azimuthal coverage is not required) relative to the measured reaction plane without introducing a bias. The E877 collaboration has in the meantime done this type of analysis, and preliminary results were obtained on nucleon and pion azimuthal distributions in the forward spectrometer [66], on detailed transverse energy flow for narrow η bins [67], and on the charged particle multiplicity azimuthal distribution $d^2N_c/d\phi d\eta$ distributions measured by the MULT detector [68] relative to the reaction plane determined using TCAL.

Another strong correlation appears between the orientation of the second harmonic in the η^m window ψ_2^m and the orientation of the first harmonic in the η^f window ψ_1^f. We define the angle difference as $\Delta\psi_{21}^{mf} \equiv \psi_2^m - \psi_1^f$, and present its distribution in Fig. 4.21 for different centrality bins. Peaks located near 0° and 180° indicate that the long axis of the ellipse in the η^m window lies in

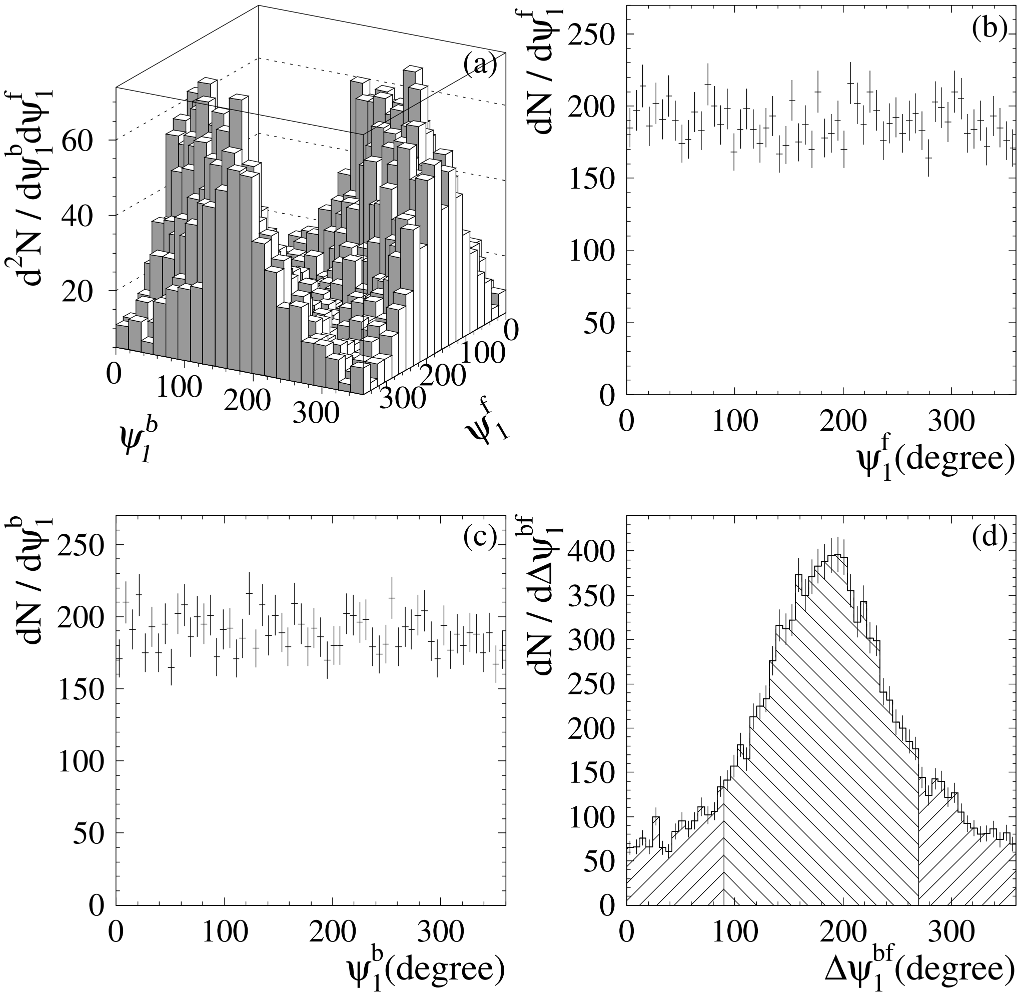

Figure 4.18: Distribution of the flow angles of the first harmonic for events with 200—220 GeV E_T^{PCAL} in the backward and forward pseudorapidity windows η^b (b) and η^f (c). The 2-D correlation is plotted in (a), and (d) is the distribution of the reaction plane angle difference. The hatched regions indicate the boundaries used to calculate the ratio R defined in Eq. (4.8).

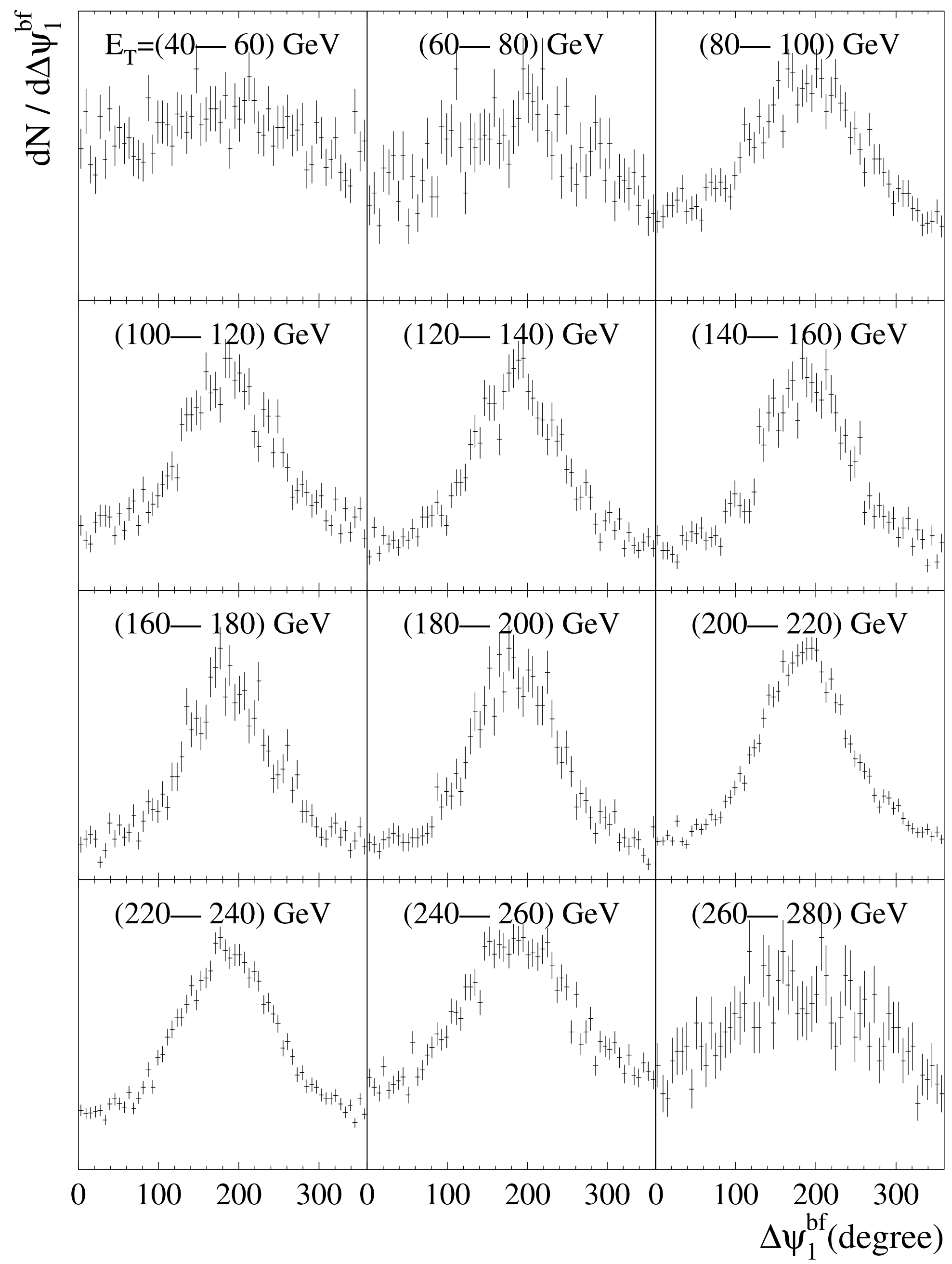

Figure 4.19: The difference between the flow angles of the first harmonic in backward and forward window for different centrality bins.

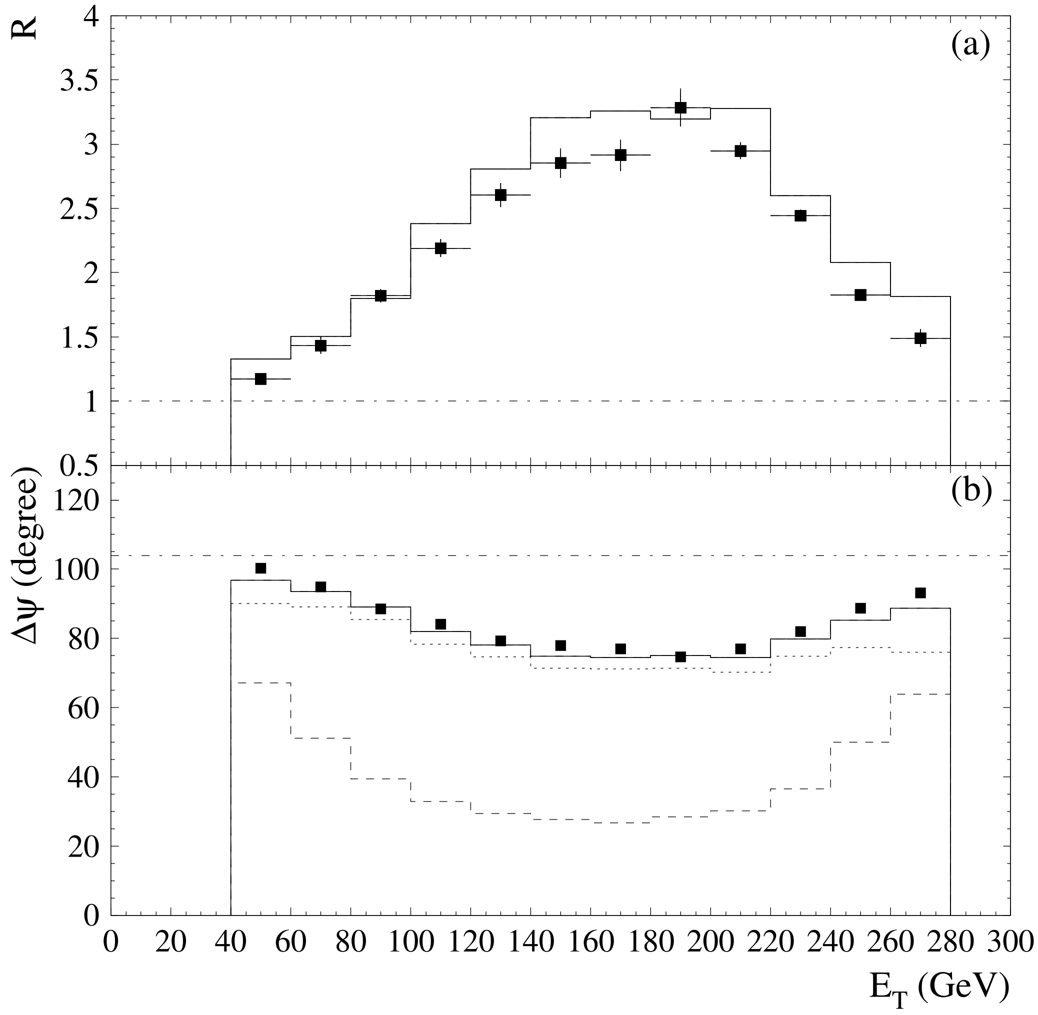

Figure 4.20: (a) Backward-forward flow angle correlation factor R, from the data (squares) and from the calculation (solid histogram) using the anisotropy and fluctuation parameters, $\tilde{v}_1^b$, $\tilde{v}_1^f$, σ_b, and σ_f. (b) The r.m.s of the angular distribution $dN/d\Delta\psi_1^{bf}$ from the data (squares) and from the calculation (solid histogram). The reaction plane resolution is also calculated for the backward window (r.m.s of $dN/d\psi_1^b$, dotted line), and the forward window ($r.m.s.$ of $dN/d\psi_1^f$, dashed histogram). The dashed-dotted lines indicate the result from a flat distribution.

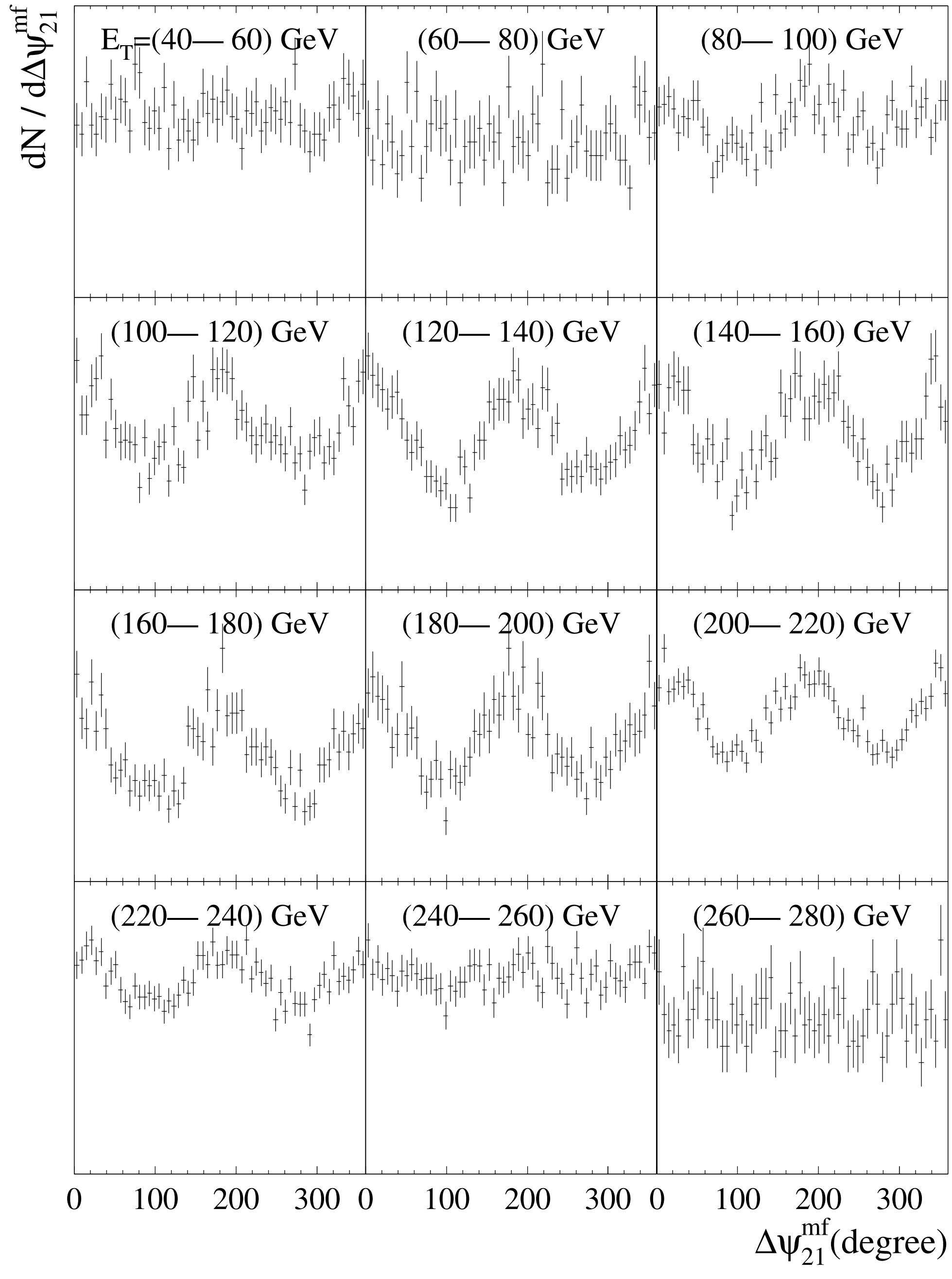

Figure 4.21: The difference between the orientation of the second moment in the η^b window and the first moment in the η^f window for different centrality bins.

the reaction plane. This observation is in contrast to the observed squeeze-out flow [47] in intermediate energy heavy ion collisions, where particles at mid-rapidity are preferentially emitted perpendicular to the reaction plane. We can at present not exclude that the elliptic distribution is a residue of the sideward flow integrated over a wide η window ($0.8 < \eta^m < 1.85$), where in fact the phase of ψ_1 changes by 180°. This will be investigated further with narrower pseudorapidity windows in an analysis using the reaction plane determined by TCAL (see above).

4.3.5 Discussion

In this section, we discuss the fit parameters, and address a few technical issues in the flow analysis.

The anisotropy parameters:

Fig. 4.22 plots the anisotropy parameters listed in Tables 4.6—4.8. The shape parameters of each moment in the backward (a) and forward windows (c) are similar. In both windows, $\tilde{v}_1$ appear to be the largest, indicating a dominating anisotropy in the first harmonic or sideward flow pointing back-to-back between the two η windows (as discussed in the azimuthal correlation in Sec. 4.3.4), and reaching a maximum around mid-centrality. The second moment $\tilde{v}_2$ is small but non-zero in these two η windows, while $\tilde{v}_4$ is consistent with zero. In the mid pseudorapidity window the first moment is consistent with zero, somewhat unexpected because the pseudorapidity window covers mid-rapidity but is actually not symmetric around mid-rapidity. We address this further when we discuss the selection of the η bins. The second moment in this window, $\tilde{v}_2^m$, appears to be the largest, corresponding to an elliptical event shape, but, as indicated above, this could be the residue from the first moment and the pseudorapidity integration. A small but non-zero forth moment is an indication that more complicated event shapes could be formed in this window. To give a clearer physical picture, we construct the azimuthal E_T distribution according to Eq. (2.28), which becomes, in our case,

$$\begin{aligned} r'(\phi) \equiv \frac{\pi}{E_T}\frac{dE_T(\phi)}{d\phi} &= 0.5 + \sum_{n=1}^{4} \tilde{v}_n \cos n(\phi - \tilde{\psi}_n) \\ &= 0.5 + \sum_{n=1}^{4} \tilde{v}_n \cos[n(\phi - \psi_r) - l\pi] \end{aligned} \tag{4.9}$$

where $\tilde{\psi}_n$ is the orientation of the anisotropy, and ψ_r is the reaction plane angle, and their relation is given by Eq. (2.31). There is an ambiguity in $l = 0$

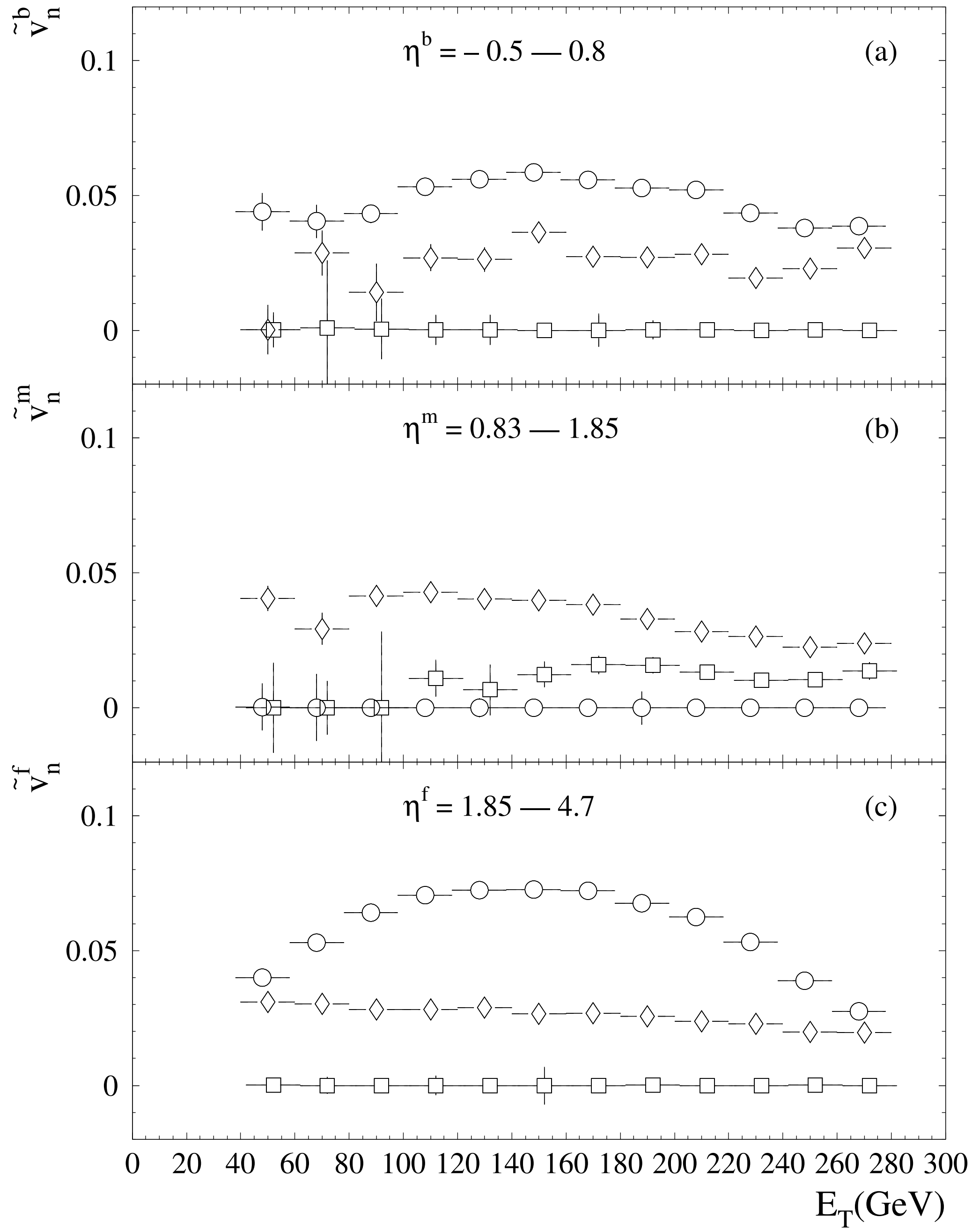

Figure 4.22: Anisotropy parameters $\tilde{v}_1$ (circle), $\tilde{v}_2$ (diamond) and $\tilde{v}_4$ (square) in the three pseudorapidity windows plotted as function of centrality selected by PCal E_T.

or 1, but it can be resolved from the azimuthal correlations after assigning ψ_r to be, *e. g.*, the sideward flow direction (ψ_1^f)in the forward pseudorapidity window. The normalized azimuthal E_T distribution in all three η windows are,

$$\begin{aligned} r'(\phi')^b &= 0.5 - \tilde{v}_1^b \cos(\phi') + \tilde{v}_2^b \cos(2\phi') + \tilde{v}_4^b \cos(4\phi'), \\ r'(\phi')^m &= 0.5 + \tilde{v}_1^m \cos(\phi') + \tilde{v}_2^m \cos(2\phi') + \tilde{v}_4^m \cos(4\phi'), \\ r'(\phi')^f &= 0.5 + \tilde{v}_1^f \cos(\phi') + \tilde{v}_2^f \cos(2\phi') + \tilde{v}_4^f \cos(4\phi'), \end{aligned}$$

where $\phi' = \phi - \psi_r$, and the last term in the first and third equations as well as the second term of the the second equation do not contribute. The results are shown in Fig. 4.23 for different E_T bins and the three pseudorapidity windows. Note the vertical range of the plots is $0.41 < r' < 0.61$, to better visualize the shape of the distribution. These plots are of the same type as those in Fig. 2.3—2.5, which were shown to illustrate a few possible *scenarios* for azimuthal distributions. We can now tell, from the plots in Fig. 4.23, how the transverse energy is distributed azimuthally in *reality* for 11.4 A·GeV/c Au on Au collisions. This is one of the main results in this thesis.

The fluctuation parameters:

One can wonder about the consistency of the results shown in Fig. 4.22 and Fig. 4.20. Fig. 4.22 shows a shallow maximum in the sideward sideward flow around $E_T = 150$ GeV, while the azimuthal correlation R between the forward and backward windows' sideward flow maximizes around $E_T = 190$ GeV, indicating that at this E_T the best resolution for the reaction plane can be achieved. Why are the maxima at different E_T? The answer is in the fluctuation parameter σ. In Chapter 2, we showed the reaction plane resolution depends on the parameter $\tilde{\chi}_1 = \tilde{v}_1/\sigma$ (see Eq. (2.39) and Fig. 2.8). For a consistency check, $\tilde{\chi}_1^b$ and $\tilde{\chi}_1^f$ are plotted in Fig. 4.24(b), and the fluctuation parameters σ_b, σ_m, and σ_f, are shown in (a). The peak positions in (b) (210 GeV for $\tilde{\chi}_1^b$, and 170 GeV for $\tilde{\chi}_1^f$) give a combined maximum at ~190 GeV, consistent with the position of the maximum in Fig. 4.20.

Fig. 4.25 presents σ versus E_T, E_T here is the transverse energy measured in the same η window where σ is obtained (see Table 4.5). All three sets of data have a similar shape, and can be fitted by the functional form

$$\sigma = \frac{\alpha'}{\sqrt{E_T}}. \tag{4.10}$$

The fit parameters for the different η windows are $\alpha'_b = 0.25$, $\alpha'_m = 0.40$, and $\alpha'_f = 0.28$.

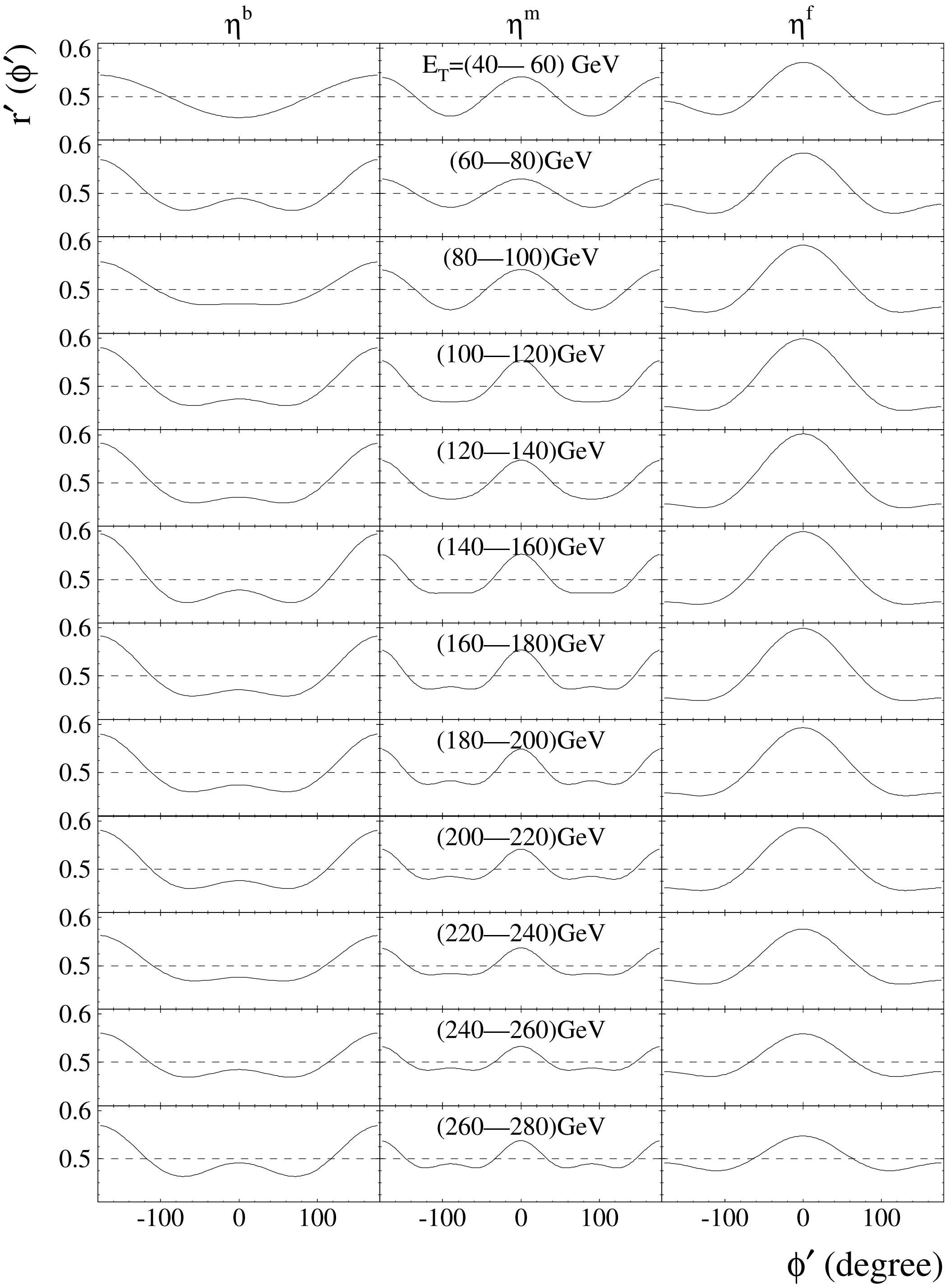

Figure 4.23: The normalized azimuthal distribution $r' = \dfrac{\pi}{E_T}\dfrac{dE_T(\phi')}{d\phi'}$ for different centrality bins and the three pseudorapidity windows.

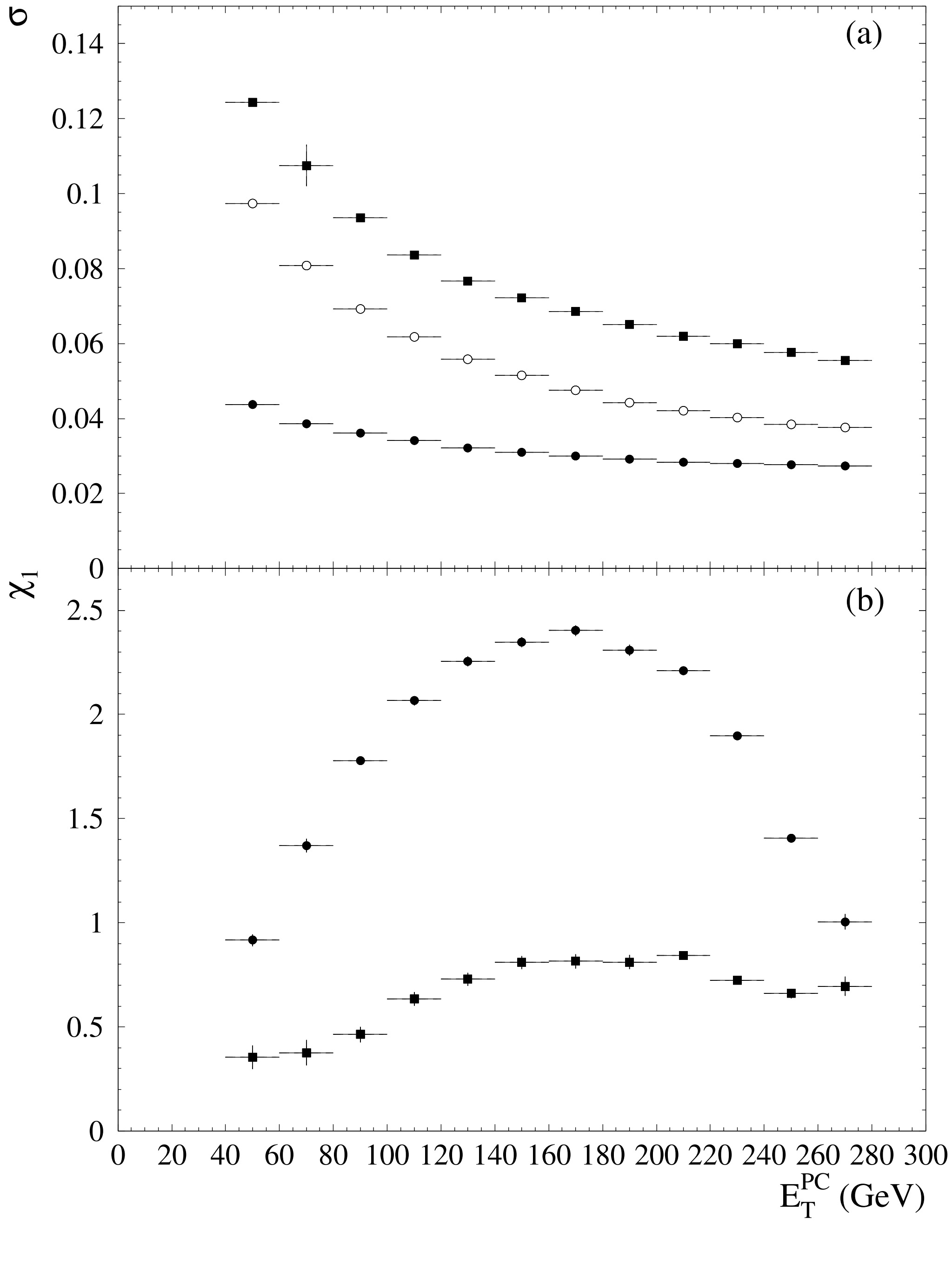

Figure 4.24: Fluctuation parameters, σ (a), and the ratio between anisotropy and fluctuation parameters, $\tilde{\chi}_1 = \tilde{v}_1/\sigma$ (b), as a function of PCAL E_T in the η_b (solid square), η_m (open circle), and η^f (solid circle) windows.

Figure 4.25: Fluctuation parameters, σ, as a function of measured E_T in the same η windows, for backward (solid square data with a dashed line fit), middle (open circle with a dashed-dotted line fit), and forward (solid circle with a dotted line fit).

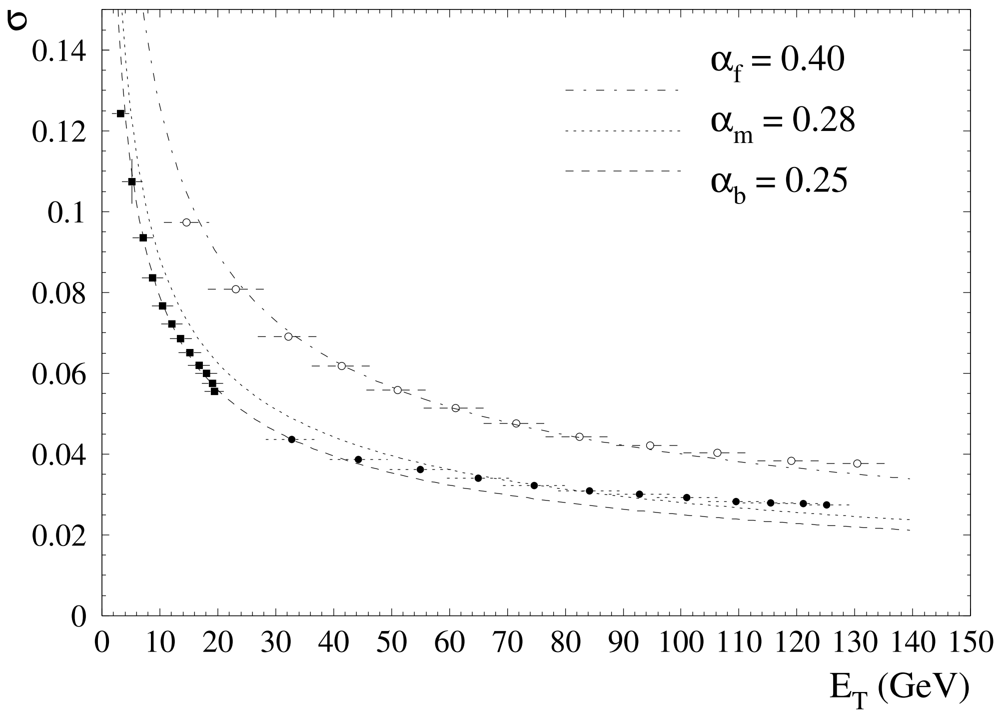

In Chapter 2, we derived the fluctuation parameter σ such that

$$\sigma^2 = \frac{\alpha}{\sqrt{M}}, \text{ where } \alpha \equiv \sqrt{\frac{\langle \epsilon_t^2 \rangle}{2\langle \epsilon_t \rangle^2}}, \tag{4.11}$$

if the particles in the (pseudo)rapidity window are independent, and the anisotropy is small. If Eq. (4.11) holds, we will get E_T per-particle to be $E_T/M = \alpha'^2/\alpha^2$. Since we do not know the single particle transverse energy ϵ_t, we can only make an estimate on the value of α. Study shows that α depends only on the *shape* of the ϵ_t distribution. A Gaussian distribution yields $\alpha = \sqrt{\pi}/2 \simeq 0.886$, and an exponential gives $\alpha = 1.0$. The real distribution is expected to be in between these two, and we take the average $\alpha \simeq 0.94$ to get $E_T/M = 0.071$ GeV, 0.181 GeV, and 0.089 GeV, in η^b, η^m, and η^f window respectively. From preliminary data of E866 [69] we see that at mid-rapidity the number of protons about equals $(n_{\pi^-} + n_{\pi^+})/2 = n_{\pi^0}$. Knowing the proton to neutron ratio in Au, assuming $n_{K^+}/n_{\pi^+} = 0.23$ [69] and neglecting other charged particles, we get $M/N_c \sim 1.77$. This would give for the mid-pseudorapidity window from the fluctuations $E_T/N_c = 0.32$ GeV. The measured E_T per-charged particle (E_T/N_c) from our experiment [49] is about 0.7 GeV in the η^m window, which is a factor of two larger than what we have estimated from the fluctuation in the E_T azimuthal distributions without taking into account the detector response. If confirmed by future analysis, this could mean that the particles in each of the η window are distributed more uniformly in E_T than it is expected from an independent random distribution.

The pseudorapidity intervals:

As discussed in Sec. 4.2.2, the centroid of the $dE_T/d\eta$ spectra is 1.7 for all centralities. From a naive symmetry consideration, one would expect to observe the strongest sideward flow in the η^b window, rather than in η^f, and some sideward flow in η^m orienting to the same direction as the flow angle in η^b window. This does not agree with the experimental results, and the reason is two-fold.

(1) Leakage fluctuations severely limit the size of the flow effect in the TCal (covering η^b) and also are important for large angles in the PCal (corresponding to the lower part of the η^m interval). On the other hand, the η^f interval is well covered with minimal leakage fluctuations.

(2) Since we used pseudorapidity windows, there is no longer symmetry around mid-rapidity. In particular, the particle mix (nucleon/pion ratio) changes significantly over the η coverage. As shown below, this ratio becomes

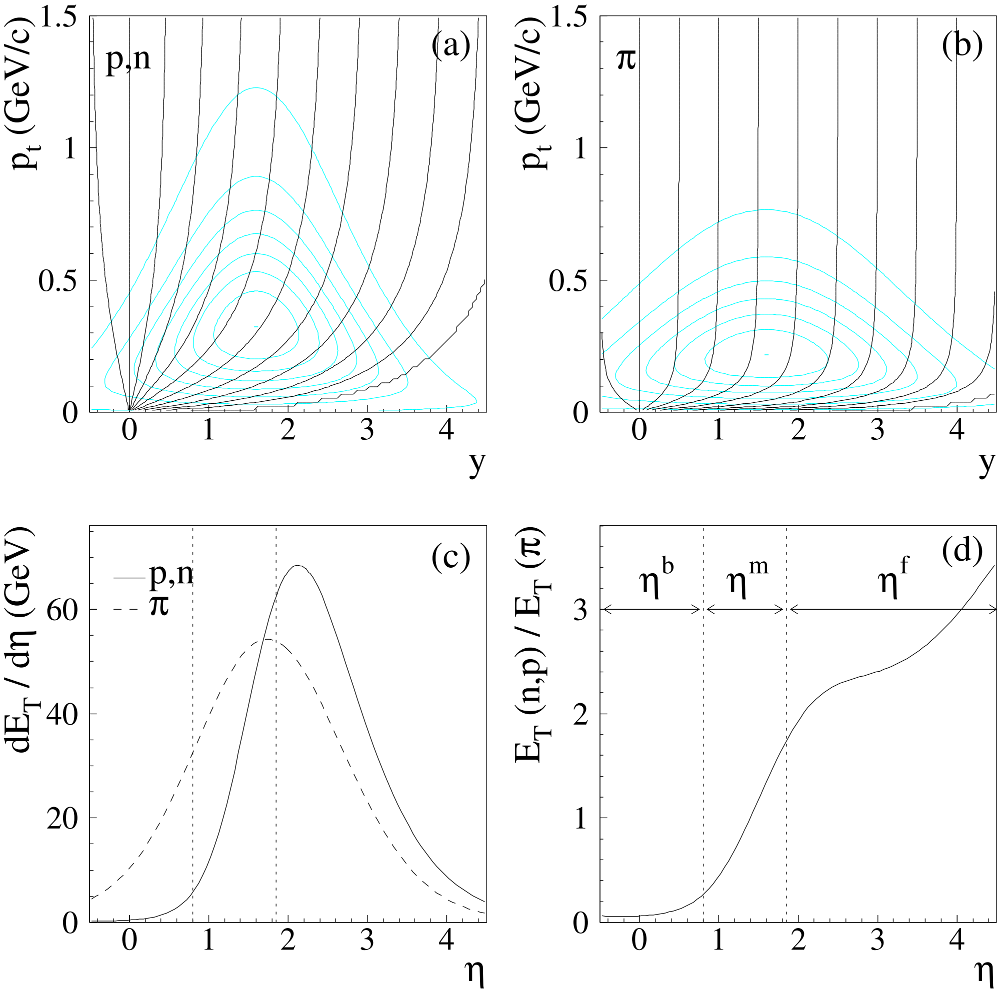

Figure 4.26: Contours of pseudorapidity intervals ranging from -0.5 to 5.0 (solid lines, with equal steps of 0.5) for nucleons (a) and pions (b) are plotted in p_t and y space. Dotted contour lines represent the particle density distributions given by Eq. (4.12). $dE_T/d\eta$ spectra for nucleons (solid line) and pions (dashed line) are shown in (c), and (d) shows the ratio of the two.

Table 4.9: Gaussian parameters used in a thermal parameterization (Eq. (4.12)) for nucleon and pion spectra.

	nucleons		pions	
	height	σ	height	σ
A_B	10.0	1.5	10.0	2.0
T_B (GeV)	0.15	1.0	0.14	2.0

very small for $\eta < 1$. As we now know the sideward flow is carried mainly by nucleons [66], so the particle ratio is important for the magnitude of the flow effect observed in the inclusive global observable. Therefore, the expected larger nucleon-pion ratio in the η^f window will be important for the large flow effect observed in this interval. The particle ratios as a function of η can be worked out from various models. A more straight forward, yet intuitive argument is given next.

Fig. 4.26 shows contours of constant pseudorapidity (solid lines) in the phase space of p_t versus y, and the parameterized d^2M/dp_tdy distribution (dashed contour lines) for nucleons (a), and pions (b). We employed a thermal parameterization [16],

$$\frac{d^2M}{dp_tdy} = A_B(y)p_tm_t\exp(-\frac{m_t}{T_B(y)}), \tag{4.12}$$

where the rapidity dependence of the normalization factor $A_B(y)$ and the "temperature" $T_B(y)$ are both assumed to be Gaussian centered around $y_{\text{c.m.s.}} = 1.6$ [16]. Table 4.9 lists the parameters used in Eq. (4.12). We then calculate particle's transverse energy $\epsilon_t(p_t, y, m)$ according to

$$\epsilon_t = \epsilon\sin\theta = \epsilon\frac{p_t}{p} = \frac{m_t\cosh y}{\sqrt{m_t^2\cosh^2 y - m^2}}p_t, \tag{4.13}$$

where m is the mass, $m_t = \sqrt{m^2 + p_t^2}$ is the transverse mass, and y is the rapidity of the particle. For nucleons and some other particles only the kinetic energy is measured experimentally, which gives

$$\epsilon_t = (\epsilon - m)\sin\theta = \sqrt{\frac{m_t^2\cosh y - m}{m_t^2\cosh y + m}}p_t, \tag{4.14}$$

Fig. 4.27 plots $\epsilon_t(p_t, y)$ for nucleons and pions.

Figure 4.27: Single particle transverse energy ϵ_t as a function of p_t and y calculated for nucleons and neutral pions according to Eq. (4.14) and, respectively.

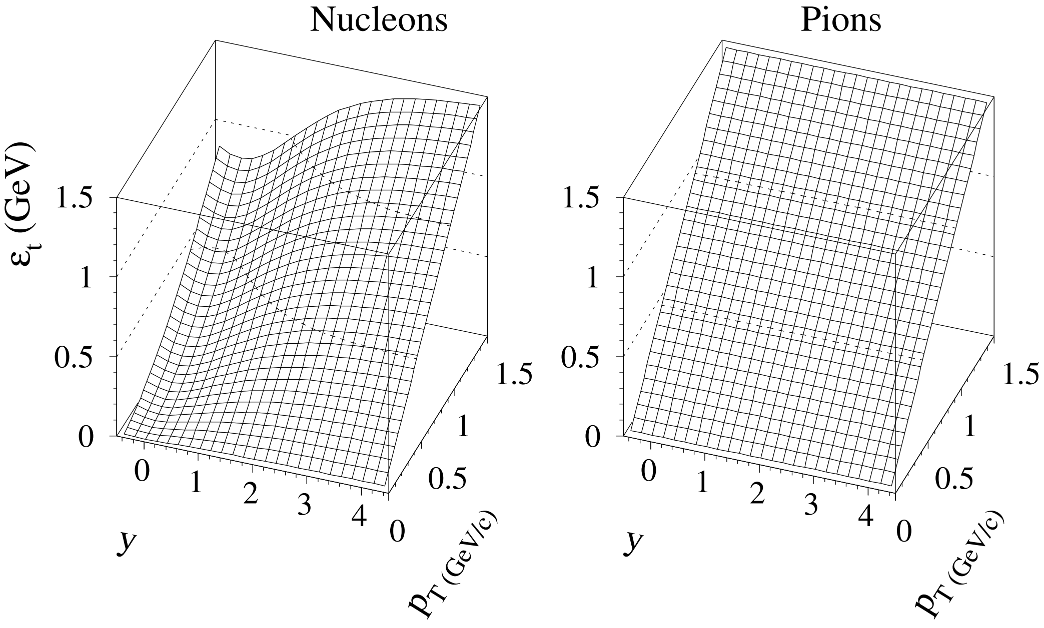

We then project the ϵ_t weighted with the density distributions (4.12) onto the η bins to obtain the $dE_T/d\eta$ distribution for nucleons and pions as shown in Fig. 4.26(c). The ratio between the two is shown in (d). The averaged $E_T(n,p)/E_T(\pi)$ ratios in the backward, middle, and forward windows are 0.13, 1.0, and 2.3 , respectively. The absolute value depends on the parameterization and normalization, but the relative shift between $dE_T/d\eta$ spectra for nucleons and pions is due to the kinematics, and remains qualitatively the same for any reasonable parameterization. Since we expect pions to have less flow or even "anti"-flow (the opposite direction of nucleon flow), the overall transverse energy flow should be reduced in the η^b window, whereas enhanced in the η^f window.

Beam angles and systematic errors:

The typical beam spot on our target is about 2 mm in diameter, small enough to be neglected for the energy flow measurement. But since the ion beam is focused on our target with a quadrapole magnet, most of the ions hit the target at an angle relative to the z-axis. This could cause an artificial azimuthal asymmetry of importance to the flow analysis. In the E877 setup,

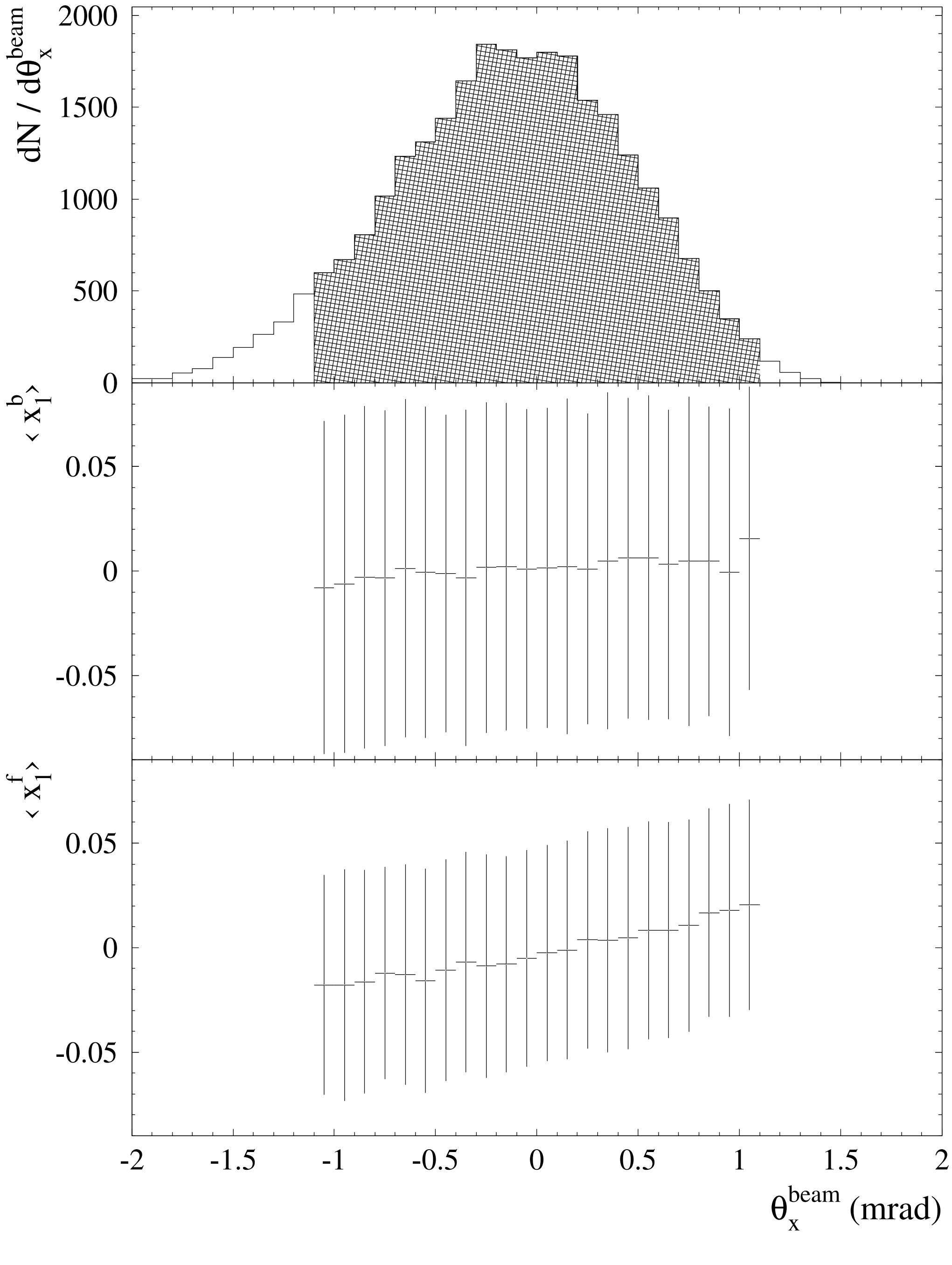

Figure 4.28: The horizontal beam angle θ_x^{beam} distribution (a), and averaged x_1 over many events in the backward (b) and forward window (c) as a function of this angle.

the beam angle is measured by the BVER horizontally (in the x—z plane). Fig. 4.28(a) shows the typical distribution of beam angles, with a small offset of about 0.1 mrad, and a width of about 0.6 mrad. An additional cut was made to eliminate events with a wide beam angle $|\theta_x^{beam}| > 1.1$ mrad. The Fourier coefficients can be examined as a function of the beam angle to see if there is any correlation. As one would expect, only the x-component of the first harmonic, x_1, shows a weak dependence. Fig. 4.28(b) and (c) show the averaged x_1 over many events versus beam angle θ_x^{beam} for the backward and forward windows. The $\langle x_1 \rangle$ difference between $\theta_x^{beam} = \pm 1.0$ mrad is about 0.01 for the backward window, and about 0.03 for the forward window. Since we do not measure the beam angle in vertical y-axis, θ_y^{beam}, we do not perform an event-by-event correction. We attribute this to a systematic error for the first harmonic. Taking the beam width of 0.6 mrad, the overall $\langle x_1 \rangle$ shift from beam angle is negligible for the backward window, and less than 0.01 for the forward window. This is smaller than the $r.m.s.$ of the x_1^f distribution, which is about the sum of the anisotropy parameter $\tilde{v}_1^f$ and the fluctuation parameter σ^f. The fluctuations in beam angles will smear the 2-D $d^2N/dx_1^f dy_1^f$ further (see Fig. 4.14). For the ring-shaped distributions around mid-centrality bins, beam fluctuations enlarge the value of σ^f, but have little effect on $\tilde{v}_1^f$ (because the fluctuations can go either inside the ring and outside the ring, and the maxima in the 2-D plots are barely changed). The other distributions in lower and higher centrality bins are widen by the beam fluctuations, but the simultaneous fitting will result larger values $\tilde{v}_1^f$ than the real ones. This effect is stronger for the most central collisions where $\sigma^f \simeq 0.4$. The value of 0.01 is safe to be used as a systematic error for $\tilde{v}_1^f$. The other major systematic error comes from the "global correction" procedure discussed in Sec. 4.3.2. Monte Carlo studies show that "global correction" modifies the original input anisotropy parameters within ten percent, which is the dominating systematic error for all the other anisotropy parameters.

A general argument can be gleaned from the discussion about the beam angles. For flow measurements, it is preferable to use a detector sitting at a large polar angle ($\theta \gg \theta^{beam}$) to minimize possible artifacts from beam angles. For example, it is especially dangerous to use a zero degree detector ($\theta \sim \theta^{beam}$) to measure the reaction plane unless the beam angle is measured and corrected event-by-event, or the effect is understood quantitatively and accounted for in the analysis.

Chapter 5

Model Calculations: Cascade and Hydrodynamics

In this chapter, we examine two types of model calculations, and compare their predictions to the observed azimuthal anisotropic event shapes. These two models represent two opposite approaches to relativistic heavy ion collisions. In the cascade approach, a nucleus-nucleus collision is described microscopically by individual nucleon-nucleon or parton-parton collisions. It was understood at the early stage of the heavy program many years ago that the "re-scattering" process must be taken into account to explain the experimental data. "Re-scattering" means the particles produced by direct collisions between the projectile and target nucleons may re-interact with or re-scatter from other particles. As consequences of "re-scattering", the stopping power is increased, and thermal and chemical equilibrium is achieved to relatively higher degree.

On the other hand, the hydrodynamical approach treats nuclei as liquid drops colliding with each other. It starts from macroscopic equations, including the energy-momentum and baryon number conservation, and an equation of state (EOS) reflecting the property of the matter under study. The initial conditions, such as energy density and source size, can be either input parameters, or the result of the proper treatment of shock wave caused by the collision. The system evolves according to these constraints, and expands until the density is lower than a critical density (usually half or one third of normal nuclear matter density), and then the momentum distributions of fluid cells are treated as the distributions of the final freeze-out particles with an additional thermal motion imposed on top of the flow motion.

In the first section, we discuss RQMD, one of the cascade models commonly used in the field. We then turn to an ideal one-fluid hydrodynamical model in the second section. In the last section, based on the comparison between experimental results and the model calculations, we address the key physics issue – the nature of the observed flow.

5.1 The Relativistic Quantum Molecular Dynamics Model

There are many references describing RQMD [64, 70]. The basic idea of the model is the following. The motion of hadrons is treated classically and relativistically. Two hadrons are allowed to scatter at a c.m.s. distance $d \leq \sqrt{\sigma/\pi}$ where σ is the cross section. Particle production is the result of the decay of excited resonances produced in inelastic collisions. Lower mass resonances decay according to the branching ratios from known experimental data, where the mean lifetime is given by the inverse of their mass width. The decay of higher resonances is based on a string fragmentation scheme [71], with parameters such that the experimentally observed particle multiplicities, transverse momentum and rapidity distributions are reproduced. Only data from hadron-hadron collisions are used to constrain the parameters of the model. In addition, a repulsive mean-field acting between nucleons can be switched on as an option [72].

Transverse energy flow:

We ran the RQMD (version 1.08 without mean-field) cascade model for 11.4 A·GeV/c Au on Au collisions, and obtained 4000 minimum-bias events, and additional central events including 300 events with $b < 5$ fm, and 500 events with $b < 1$ fm. To make a quantitative comparison with the transverse energy flow from the experiment, the RQMD events were filtered using a fast detector simulation program, PROPHET [73] with parameters optimized for the PCAL [74]. Unlike the standard GEANT [59] program, which explicitly follows the track of every secondary particle as the shower develops, PROPHET speeds up the simulation by parameterizing the longitudinal and lateral shower profile.

Fig. 5.1 shows the anisotropy parameters, $\tilde{v}_n$ ($n = 1, 2, 4$) from RQMD (lines) and from data (symbols) in the middle and forward η windows. The most dramatic discrepancy between the model and data is in the first harmonic, $\tilde{v}_1$, in the η^f window, where for semi-central collisions the amplitude of sideward flow in RQMD is about a factor of two smaller than in the data. This discrepancy is linked to the fact that the model exhibits a large "anti"-flow for pions (see discussion next), which cancels in part the nucleon-flow, and

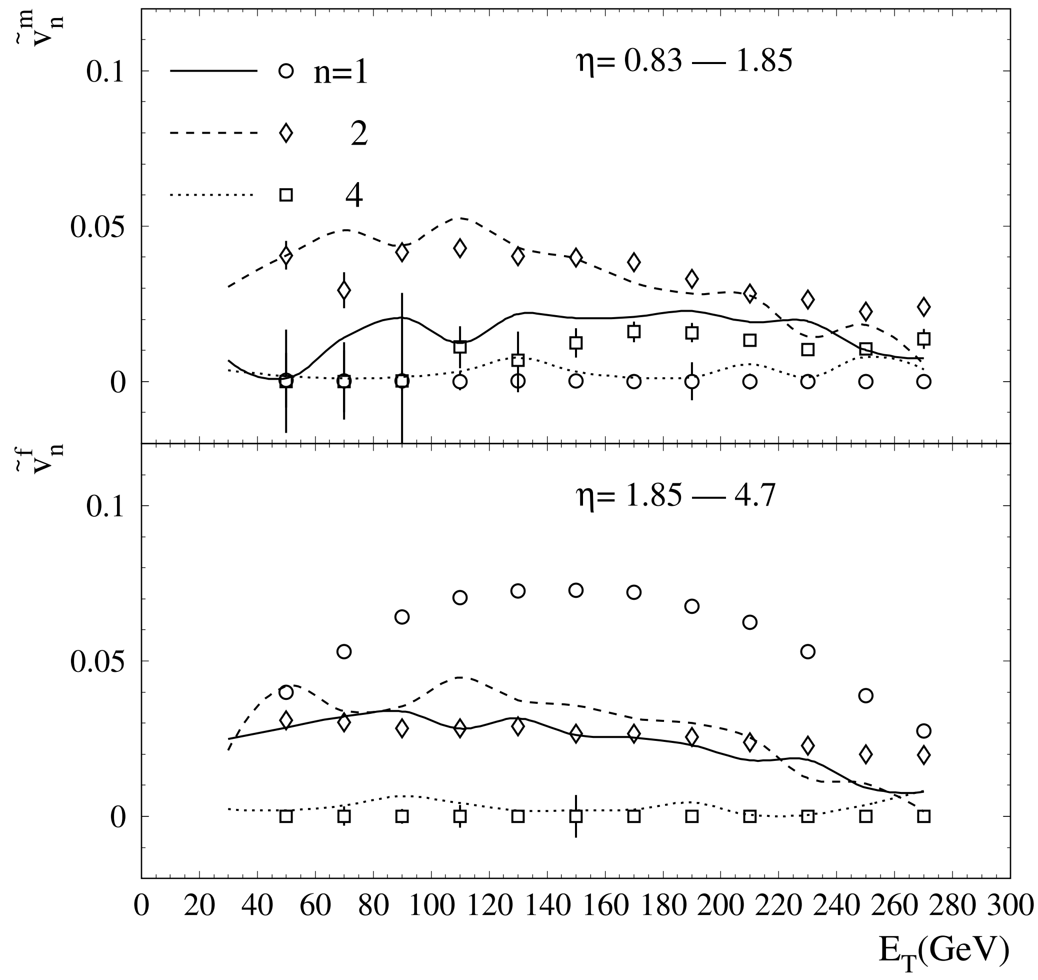

Figure 5.1: Anisotropy parameters $\tilde{v}_n$ ($n = 1, 2, 4$) from RQMD (various lines), and from data (various symbols) in the η^m and η^f windows as a function of centrality. For RQMD, centrality is determined by selecting evens with same cross section as in data.

therefore the overall magnitude of the sideward flow is reduced. There is a good agreement for the second harmonic in both η windows. The combination of the first and second harmonic suggests a larger nucleon-flow and less pion "anti"-flow in the data as compared to the model, which is also indicated by our preliminary results from the spectrometer [66]. Other differences are found for $\tilde{v}_1$ and $\tilde{v}_4$ in the η^m window. As we discussed before $\tilde{v}_1^m \simeq 0$ in data may be a consequence of the detailed balance between nucleons and pions due to their abundance and flow amplitude in the η^m window, which is not quite reproduced by RQMD. Also, RQMD gives $\tilde{v}_4$ consistent with zero, while in the data we find small but finite values. The non-zero higher moments could be the indication of hydrodynamical behavior. We will discuss this more in Sec. 5.2.

Nucleon and pion flow:

To understand the reason for the discrepancy in the transverse energy sideward flow ($\tilde{v}_1$) between RQMD and the data, we look into nucleon, and pion flow, and the net flow in RQMD in terms of a Fourier analysis of the transverse energy and transverse momentum azimuthal distributions. Fig. 5.2 presents the first moment $\tilde{v}_1$ calculated from ϵ_t as a function of pseudorapidity with a narrower bin size ($\Delta\eta = 0.4$) at different centralities. Note that, in contrast to the data, the opposite pion and nucleon flow leads to a vanishing first moment $\tilde{v}_1$ in the backward pseudorapidity window where experimentally a strong flow signal is observed (Fig. 4.22). Similarly, Fig. 5.3 presents $\tilde{v}_1$ calculated from p_t as a function of rapidity ($\Delta y = 0.4$) at different centralities. In both cases, pions exhibit strong "anti"-flow going in the opposite direction of the nucleon-flow, and reducing the overall flow, which mostly goes along with the nucleon-flow, but flips direction in some (pseudo)rapidity bins. The higher Fourier coefficients are all consistent with zero, except the second harmonic (Fig. 5.4) for which small values beyond statistical fluctuations are found over a large rapidity range, and in most of the centrality bins.

RQMD with a mean-field potential results a much smaller pion "anti"-flow, and also produce flow for other particle species, including an interesting squeeze-out phenomenon for anti-protons and anti-clusters [75]. RQMD with a mean-field gives a better agreement with our preliminary pion data [66]. Due to the large amount of computing time required to get events of RQMD with a mean-field, we have not been able to make a comparison to our data.

Collision dynamics:

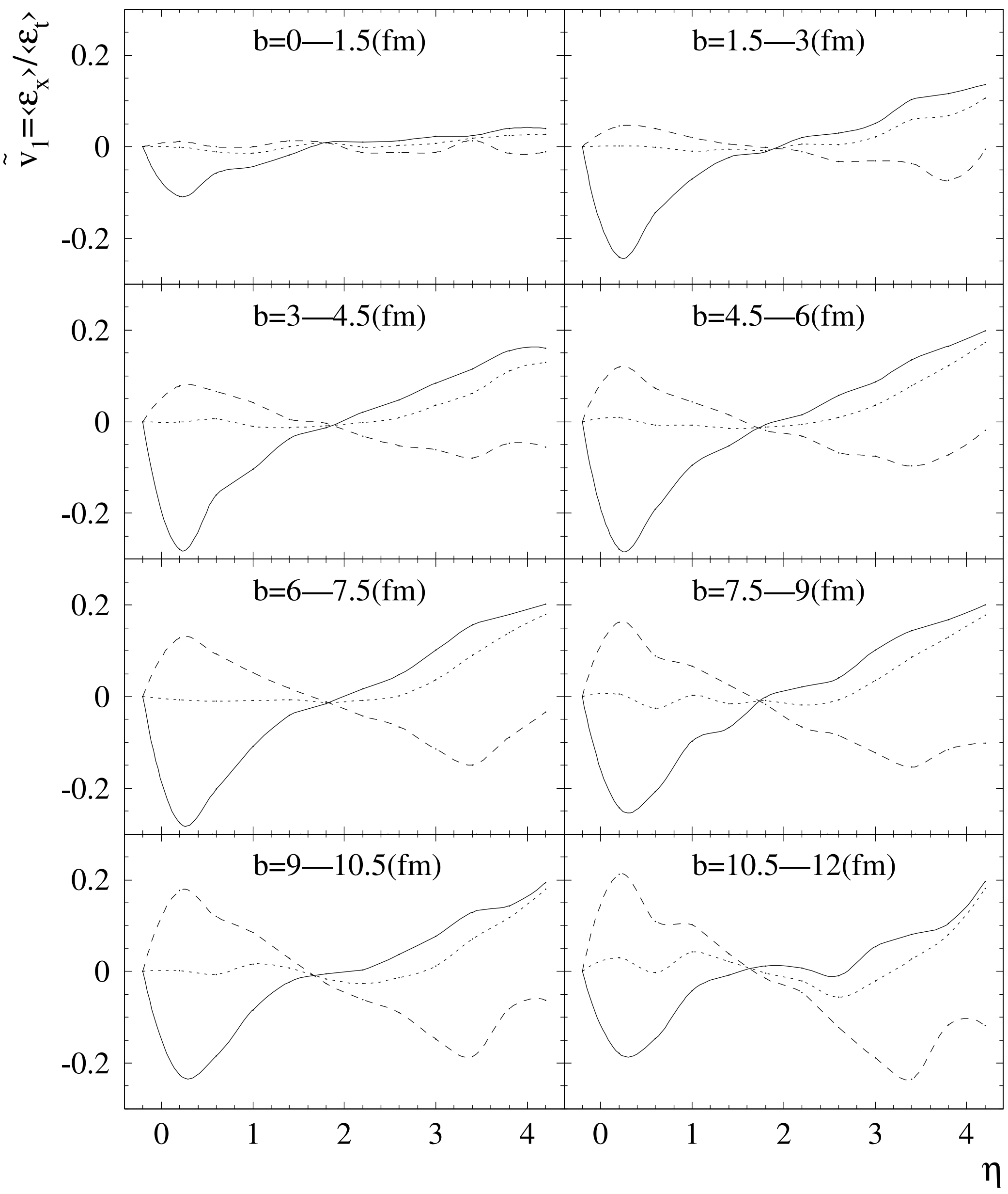

Figure 5.2: The pseudorapidity and centrality dependence of sideward transverse energy flow for nucleons (solid lines), pions (dashed lines), and all particles (dotted lines) from RQMD.

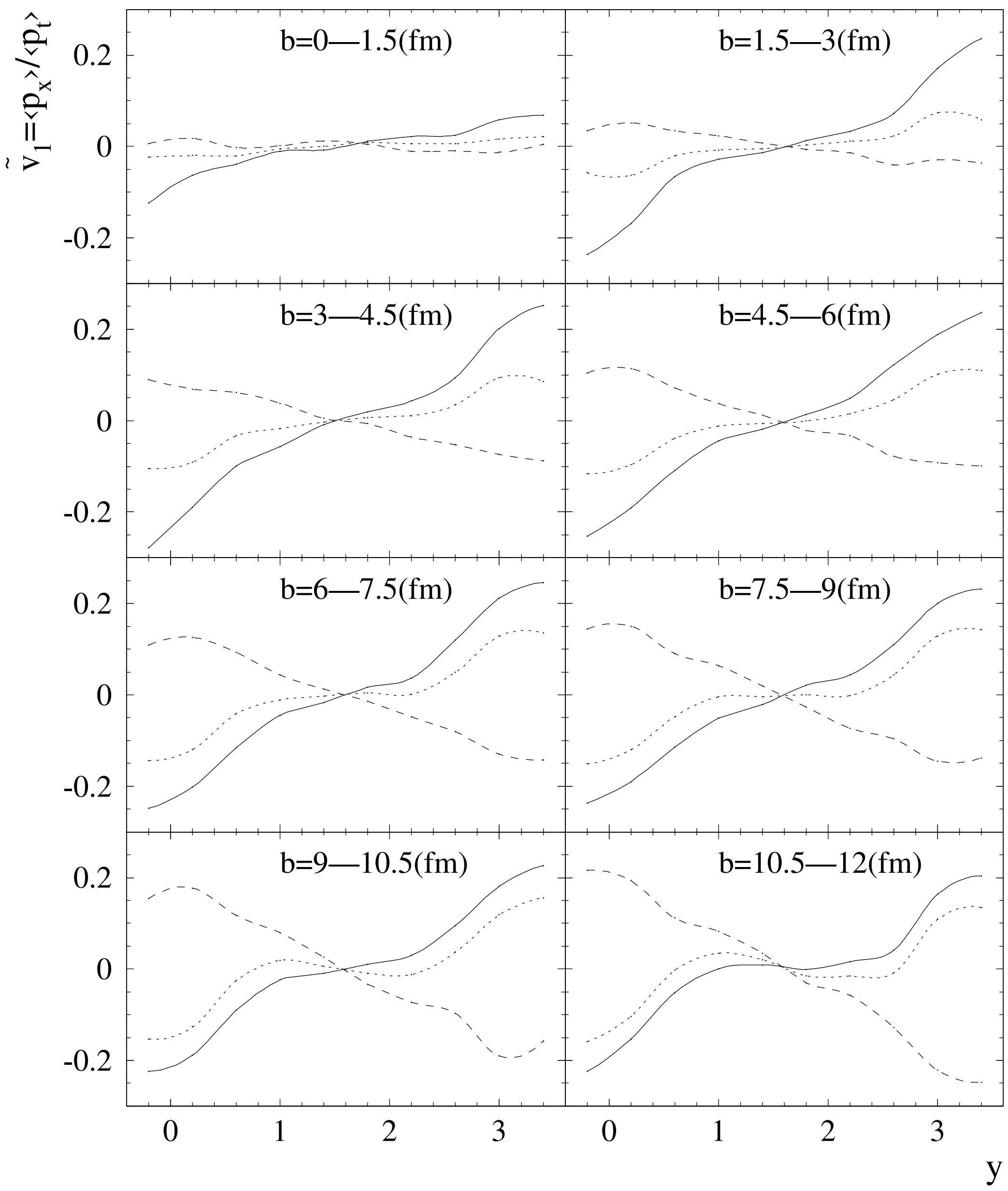

Figure 5.3: The rapidity and centrality dependence of the sideward momentum flow for nucleons (solid lines), pions (dashed lines), and all particles (dotted lines) from RQMD.

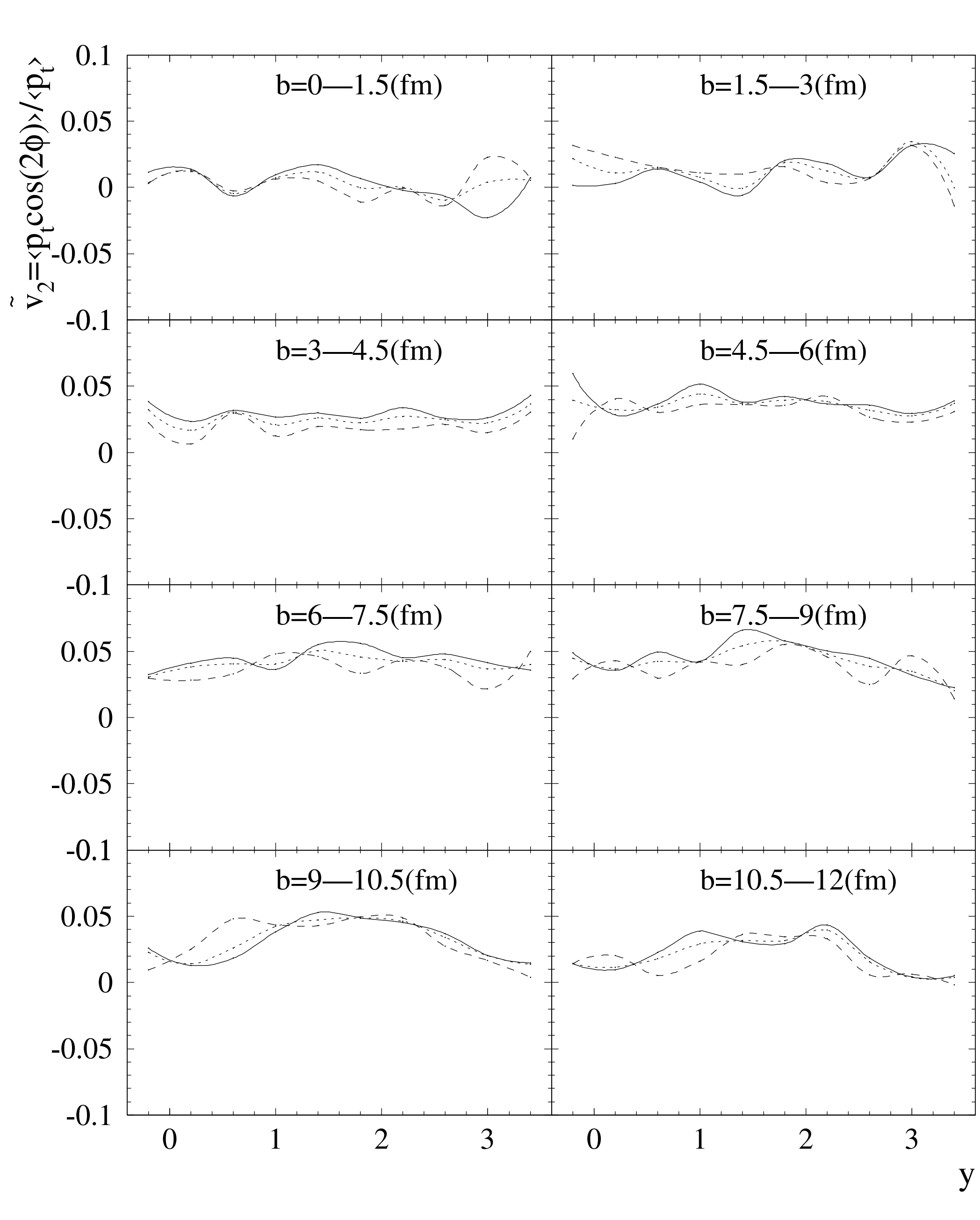

Figure 5.4: The rapidity and centrality dependence of the second harmonic in azimuthal transverse momentum distribution for nucleons (solid lines), pions (dashed lines), and all particles (dotted lines) from RQMD.

A convenient feature of cascade models is that, one can check the collision history to study the dynamics. This is generally assumed to be more realistic than in the hydrodynamic models since real particles, instead of the fluid elements in hydrodynamical models, are present from the beginning of the collision to the end at freeze-out. A study with RQMD model predicted high baryon density of up to ten times the normal nuclear density at times of about 5 fm/c in Au on Au collisions at the AGS energy [77]. Our interest here is the azimuthal distribution as a function of time. Next we show a series of snap shots of spatial and momentum distributions. We distribute our events into nine centrality bins (1.5 fm bin size, starting from 0), slice rapidity to twelve windows ($\Delta y = 0.4$, between -0.8 and 4.0), and cut the collision time into twenty intervals (2 fm/c intervals, from 0 to 40 fm/c). Figs. 5.5 and 5.6 show the transverse spatial (x—y plane, and x-axis lies in the reaction plane) and momentum (p_x and p_y) distributions for nucleons (top) and pions (bottom). The centrality bin is $6 < b < 7.5$ fm, the rapidity window is $0.8 < y < 1.2$, and all twenty time intervals are shown. The distortion of the spatial distribution is obvious: both nucleons and the produced pions are moving in the opposite direction of the impact parameter in the backward rapidity window. The averaged drift velocity is about 0.2 c (obtained by dividing the mean shift in x by the time interval). This will have little effect on the momentum measurement, but will have a big effect on the source size measurement from HBT [20]. The preliminary results of a recent E877 two-pion correlation analysis actually show a small dependence of the source size parameter on the reaction plane angle [78]. In RQMD, this distortion comes from the geometric azimuthal asymmetry of the colliding nuclei at finite impact parameter, and is transformed to an asymmetry in the momentum distribution via space-momentum correlations. The stronger the correlation, the larger the flow or collectivity, and the more asymmetry is introduced in the final momentum distribution, which is the experimental observable. The momentum distribution shown in Fig. 5.6 shows a much smaller asymmetry than the spatial distribution. Nevertheless, systematic shifts to the negative direction (opposite to $\mathbf{b}$ in the backward rapidity) are visible starting from the forth time interval ($t > 6$ fm/c), and remain for the rest of the time intervals (top plots of Fig. 5.6). This is much reduced for pions, but small shifts can be seen in the same direction as nucleons towards the end of the collision. It is interesting that even in its cascade mode, RQMD does show certain collectivity between particles. The smaller pion "anti"-flow observed in data could be the result of a stronger collective motion between nucleons and pions than what we shown here in RQMD.

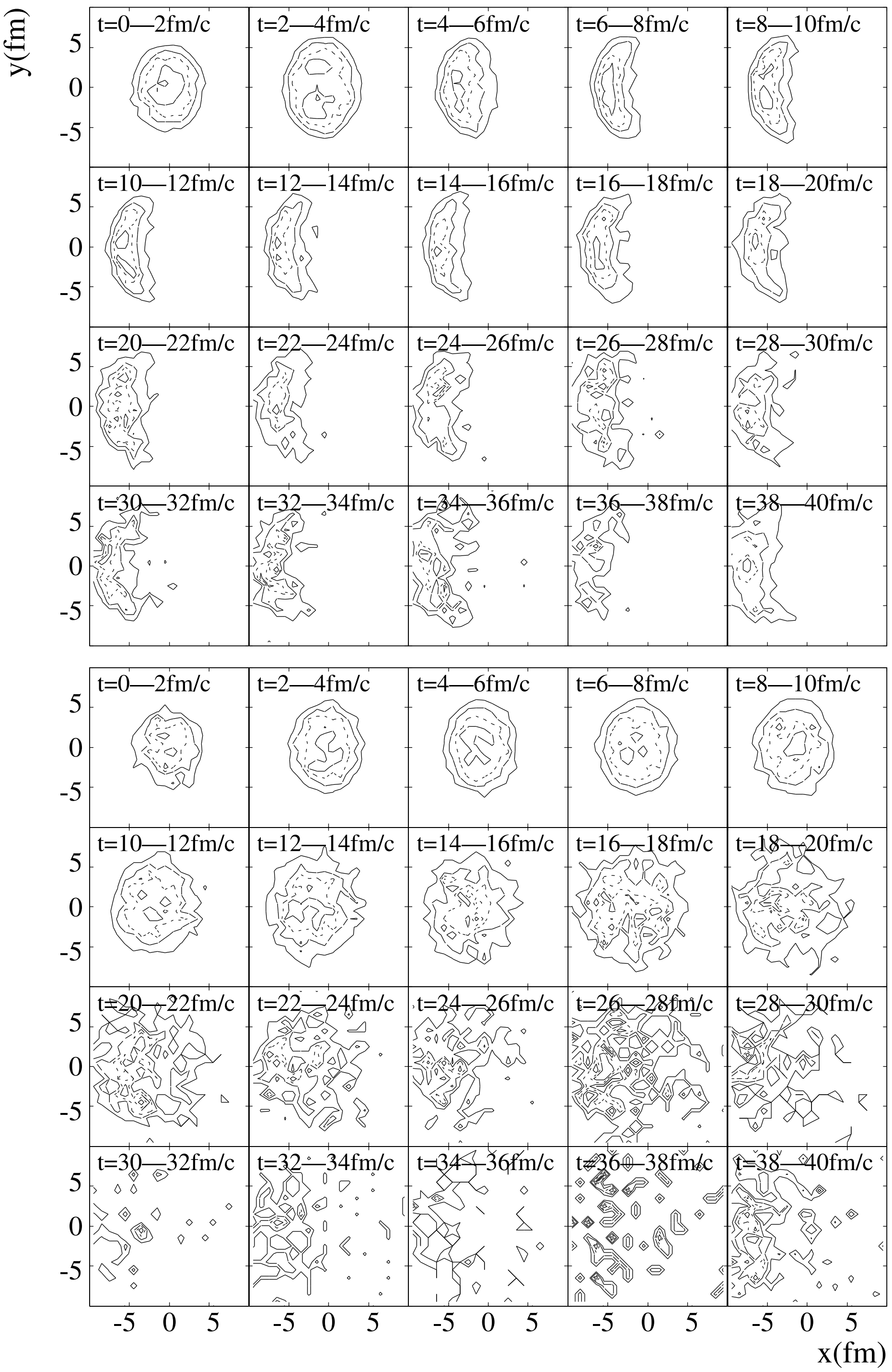

Figure 5.5: Spatial distributions $d^2M/dxdy$ for nucleons (top) and pions (bottom) in centrality bin $6 < b < 7.5$ fm and rapidity window $0.8 < y < 1.2$. The inner most contours are about factor of 10 above the outer most ones.

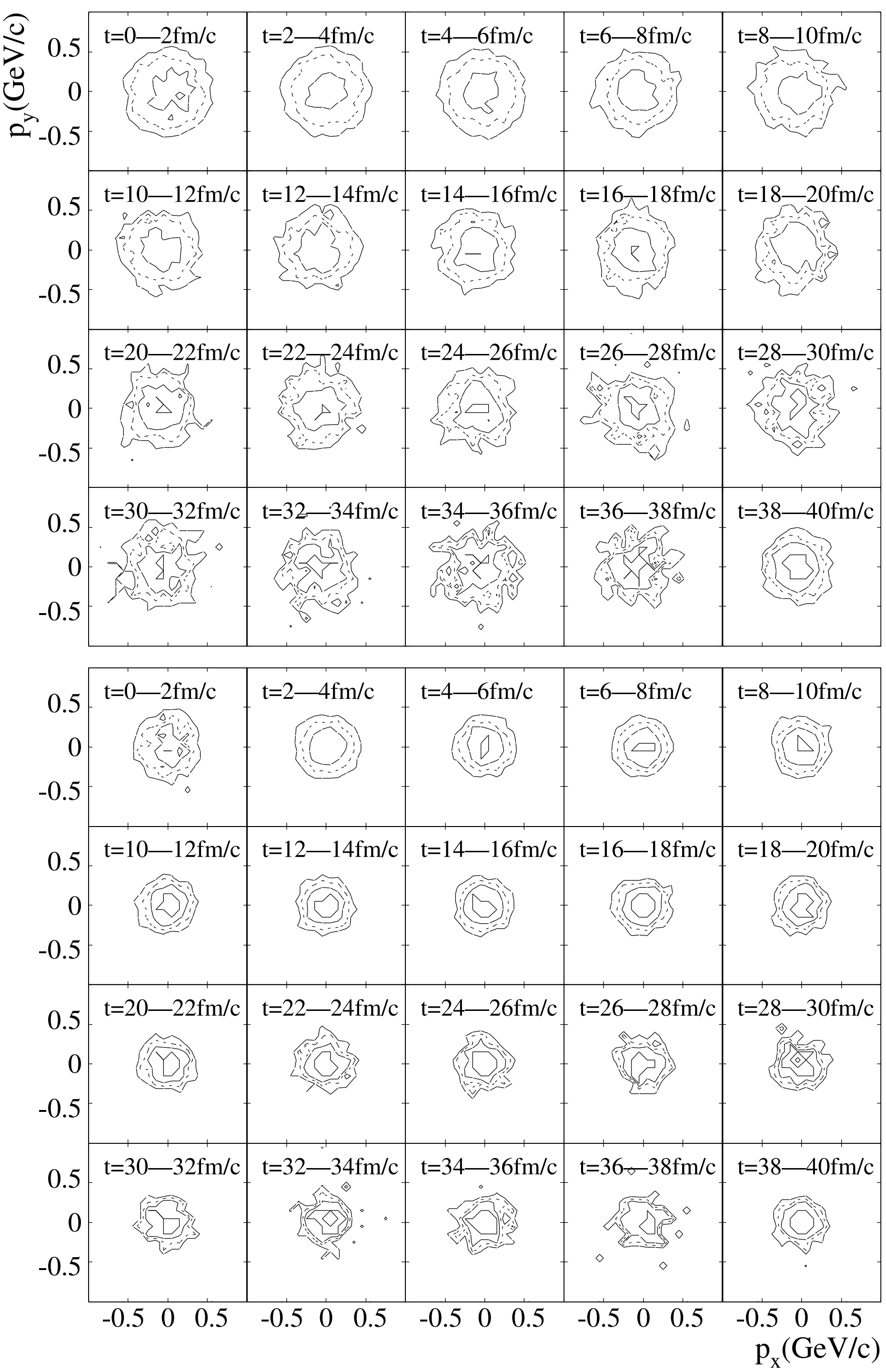

Figure 5.6: Momentum distributions $d^2M/dp_x\,dp_y$ for nucleons (top) and pions (bottom) in centrality bin $6 < b < 7.5$ fm and rapidity window $0.8 < y < 1.2$. The inner most contours are about factor of 10 above the outer most ones.

5.2 An Ideal Relativistic One-fluid Hydrodynamical Model

Hydrodynamical calculations successfully anticipated and confirmed collective flow effects in heavy ion collisions at BEVALAC energy [24, 28]. In the past few years, numerous calculations have been done for AGS energies [79, 80], and they all predicted the presence of flow. Here, we consider an ideal relativistic one-fluid hydrodynamical model developed by the Frankfurt group [81, 82].

It starts from 3+1–dimensional (3-D space and time) equations of energy-momentum and total charge (baryon) conservation. To match the number of equations to the number of variables, the EOS is given as the last input, which is chosen differently for the hadronic phase and the QGP phase. For the QGP phase, the MIT bag EOS [83] is employed, while the hadronic phase is described by a version of the σ-ω–model for a interacting hadron gas [84]. Gibbs' conditions of phase equilibrium are used at the phase boundary to match the two equations of state. A complete EOS is obtained by this matching, containing pure phases and a region where two phases are mixed (mixed phase), and the order of the phase transition is first order by construction. Based on these equations, the whole collision, including the propagation of the shock wave, the compression and expansion, is calculated numerically step by step in small time and space intervals. QGP clusters can be formed wherever and whenever the energy and baryon densities are sufficient.

Katscher [85] calculated twelve Au on Au events with beam momentum 11.4 $A\cdot$GeV/c at twelve impact parameters corresponding to the twelve PCAL E_T bins in our data analysis (see Table. 4.5). For each impact parameter, calculations were done for two scenarios, either to preserve the hadronic phase through out the collisions (called hadronic scenario in the following discussion), or to allow the formation of a QGP (called QGP scenario). This model does not include particle production, but simply puts the available energy into nucleon kinetic energy, and gives the nucleon density distribution in 3-D momentum space. This simplification causes a big discrepancy between the prediction of this model and the data for global variables, such as multiplicity and total E_T. Therefore, these events are not filtered with our detector response, and only the primary distributions were used in the following flow analysis. We first show the transverse energy flow, and then look into detailed transverse momentum distributions. Finally, a signature for the QGP phase transition is briefly discussed.

Transverse energy flow:

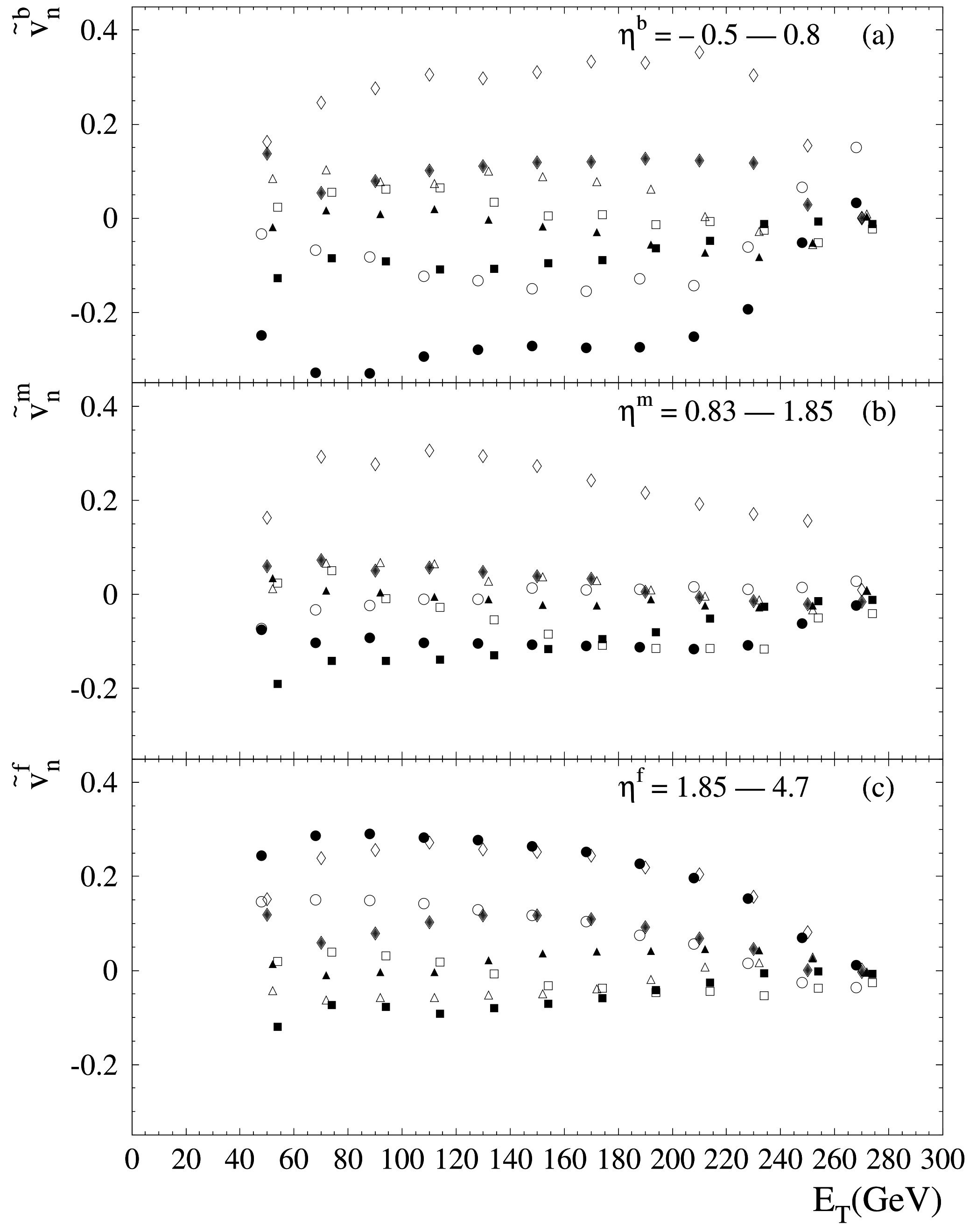

Figure 5.7: Anisotropy parameters $\tilde{v}_1$ (circle), $\tilde{v}_2$ (diamond), $\tilde{v}_3$ (triangle), and $\tilde{v}_4$ (square) in the three η windows plotted as a function of centrality. Solid symbols are for the hadronic scenario, and open symbols for the QGP scenario.

Katscher's events [85], we performed a Fourier analysis of the transverse energy in each of the three η windows as used in the data analysis. Fig. 5.7 shows the calculated anisotropy parameters with or without the formation of a QGP as a function of centrality. The E_T here is not the PCAL E_T from this calculation, but the equivalent E_T corresponding to the same centrality. We calculated the Fourier coefficients $\tilde{v}_n = \langle \epsilon_t \cos(n\phi) \rangle / \langle \epsilon_t \rangle$ for n =1, 2, 3, and 4, where ϵ_t and ϕ are the transverse energy and azimuthal emission angle relative to the reaction plane. Unlike in the data analysis, where only the absolute values of $\tilde{v}_n$ are obtained, and the sign is given by the azimuthal correlation, here the positive or negative sign is obtained directly from the calculation, which reflects the relative orientation of the n-th anisotropy to the reaction plane. The first harmonic in the backward and forward windows from both sets of calculations (the hadronic and QGP scenarios) shows qualitatively the same trend as the experimental data. Namely they show a back-to-back correlation, both reach their maximum around mid-centrality, and decrease for peripheral and the most central collisions. Both $\tilde{v}_1^b$ and $\tilde{v}_1^f$ over-predict the experimental data shown in Fig. 4.22, especially the hadronic scenario. The second harmonics, $\tilde{v}_2$, are very large and lie in the reaction plane for the QGP scenario in all three η windows, whereas small but non-zero for hadronic scenario. The non-zero forth harmonic and the smallest but sometimes non-zero third harmonic indicate the existence of complicated event shapes.

Transverse momentum flow:

We now go further with our Fourier analysis to find out the details of the transverse momentum azimuthal distribution as a function of rapidity. Fourier coefficients $\tilde{v}_n = \langle p_t \cos(n\phi) \rangle / \langle p_t \rangle$ up to $n = 4$ were calculated and are shown in Figs. 5.8 and 5.9 as a function of rapidity at different impact parameters for the hadronic and QGP scenario. Unlike in the RQMD calculations, where the higher moments are all consistent with zero, here all the moments are quite large. The structures in these plots are not from statistical fluctuations, because the hydro-calculation is deterministic, namely for a given model (EOS) and a given system (beam energy, impact parameter) the result of the calculation is pre-determined. Small errors due to the finite step size in the numerical calculation are expected, but are much smaller than these structures reflecting the dynamics of the collision. Take, *e. g.*, the first moment; the detailed rapidity dependence is far from a straight line or a smooth function, and in some cases reverses going to the opposite direction as one would have expected.

What we presented here are the azimuthal p_t distributions. One would like to know if the azimuthal distributions are the same in different p_t regions.

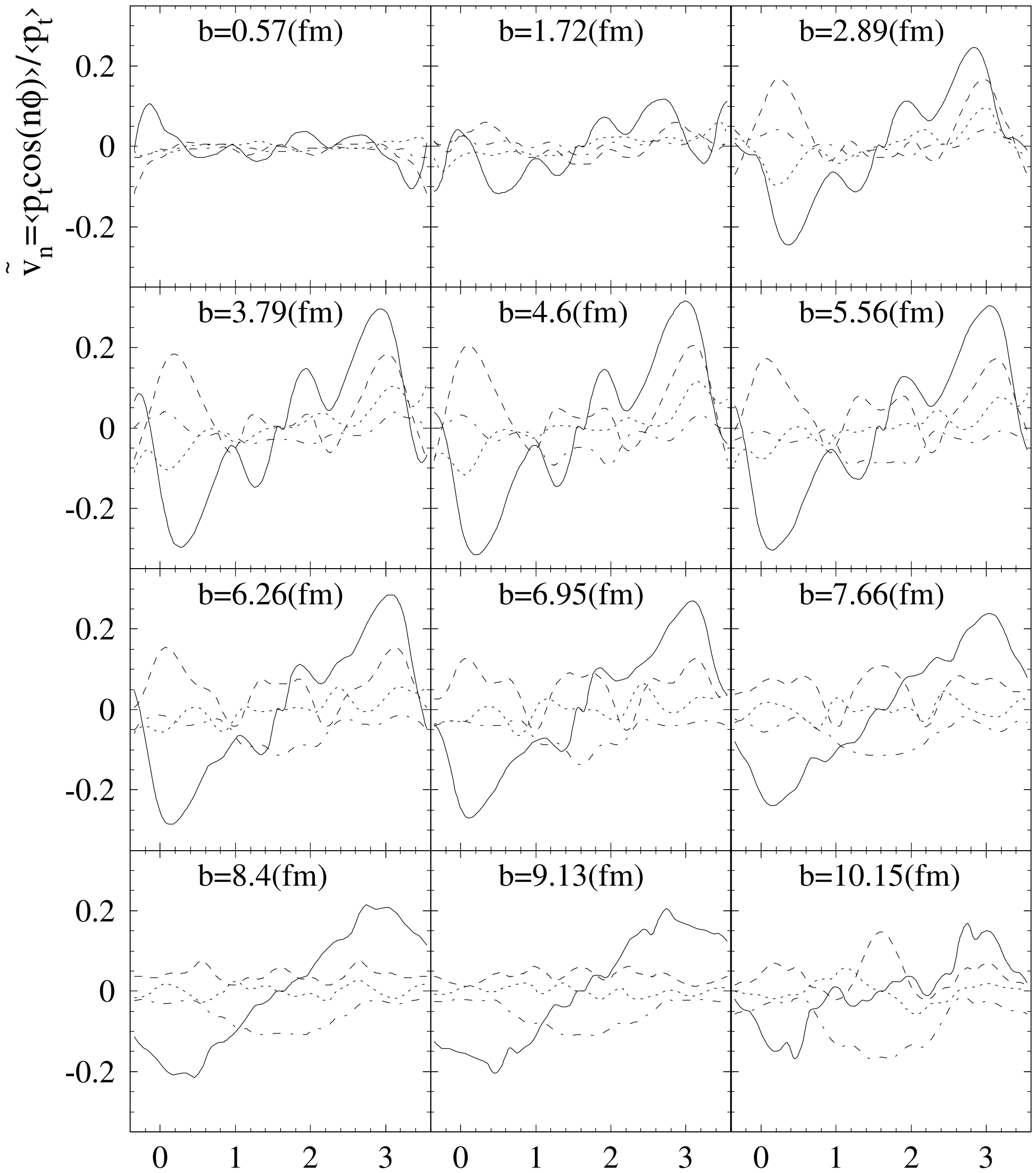

Figure 5.8: Anisotropy parameters $\tilde{v}_1$ (solid lines), $\tilde{v}_2$ (dashed lines), $\tilde{v}_3$ (dotted lines), and $\tilde{v}_4$ (dashed-dotted lines) for transverse momentum flow calculated from the hydrodynamical model with the hadronic scenario, shown for different centrality bins.

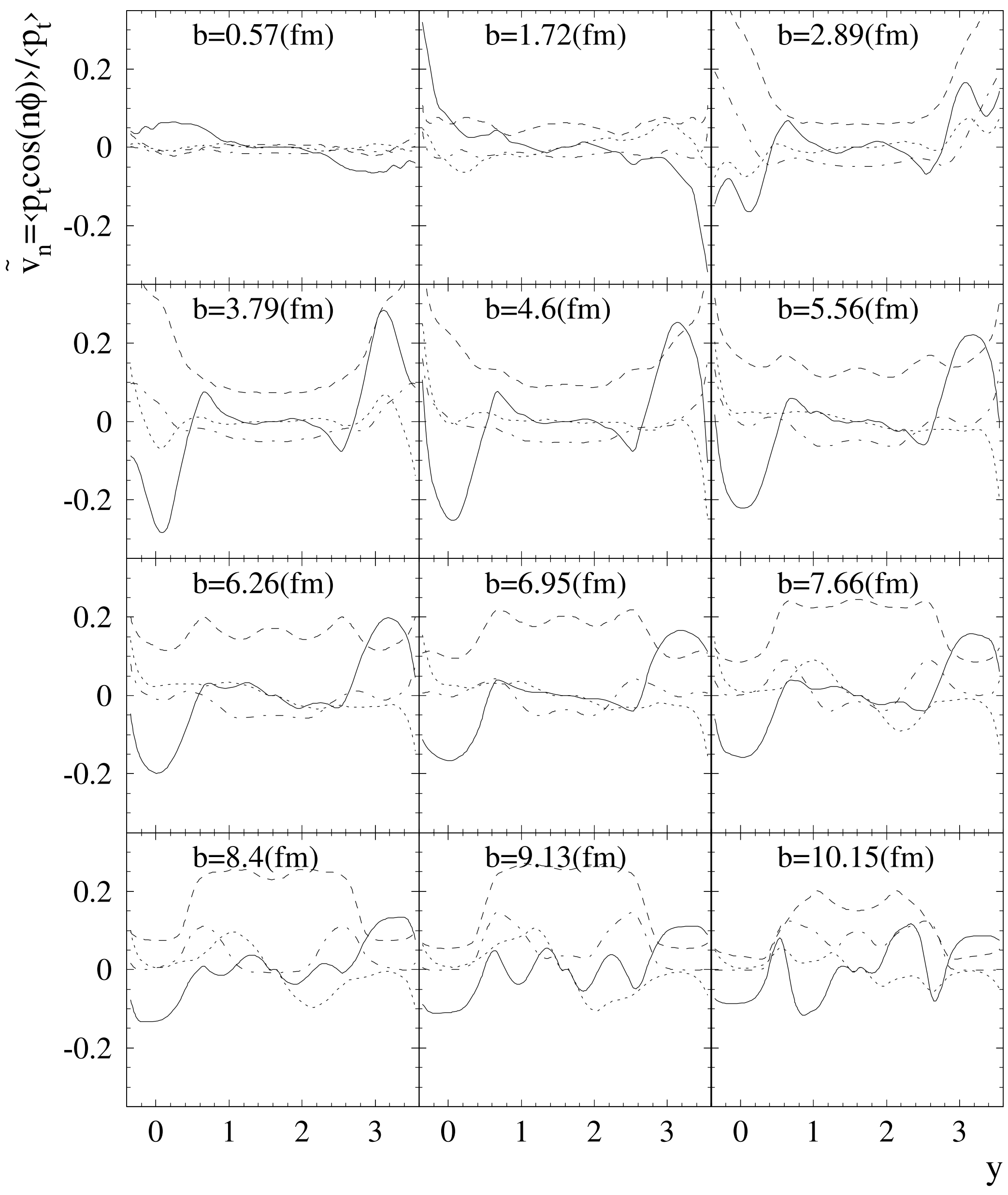

Figure 5.9: Anisotropy parameters $\tilde{v}_1$ (solid lines), $\tilde{v}_2$ (dashed lines), $\tilde{v}_3$ (dotted lines), and $\tilde{v}_4$ (dashed-dotted lines) for transverse momentum flow calculated from the hydrodynamical model with the QGP scenario, shown for different centrality bins.

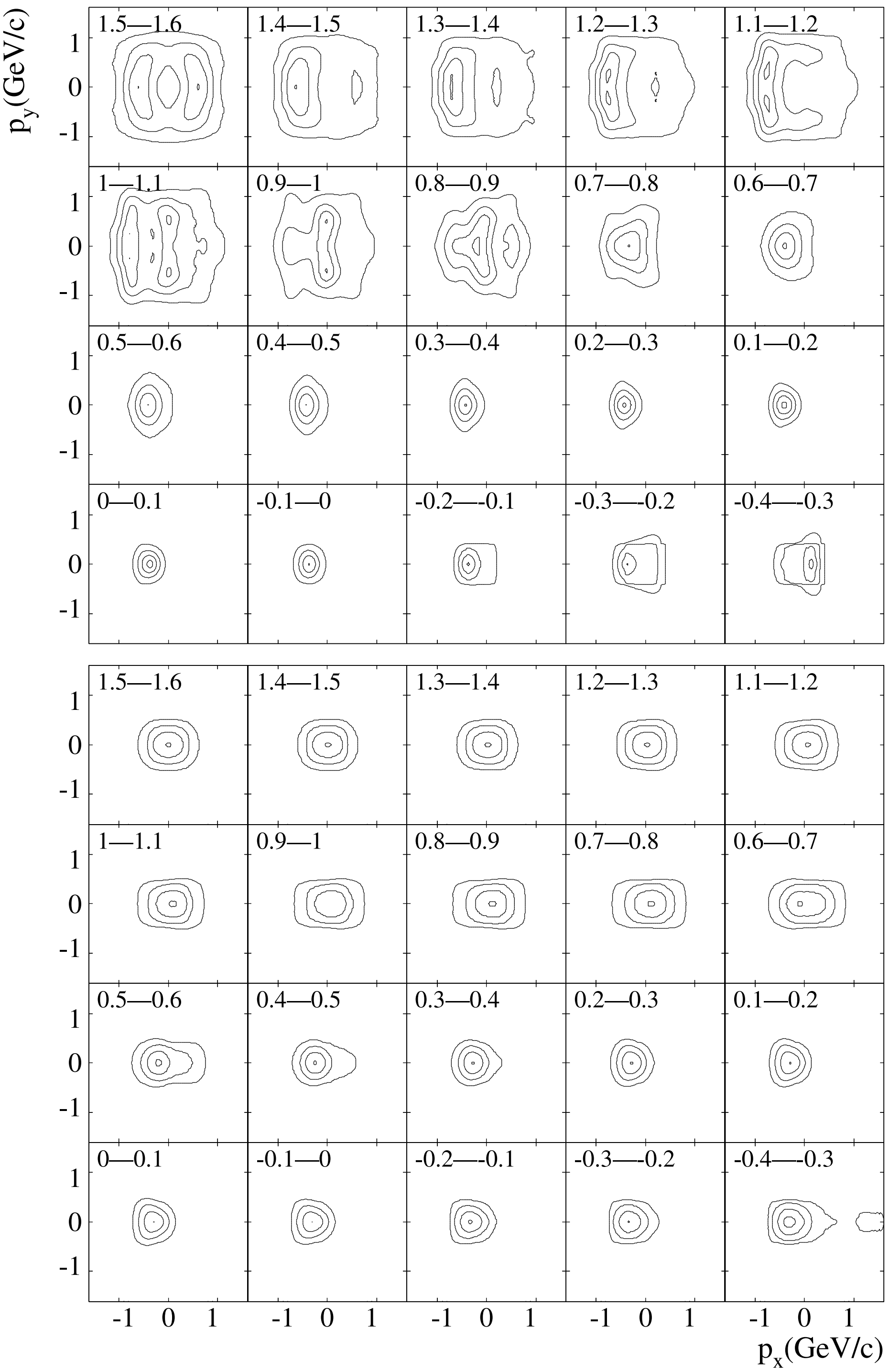

Figure 5.10: Momentum distributions $\frac{d^2M}{dp_x dp_y}$ for different rapidity bins from a hydrodynamical calculation for hadronic (top) and QGP (bottom) scenarios [85]. The centrality is $b = 5.56$ fm.

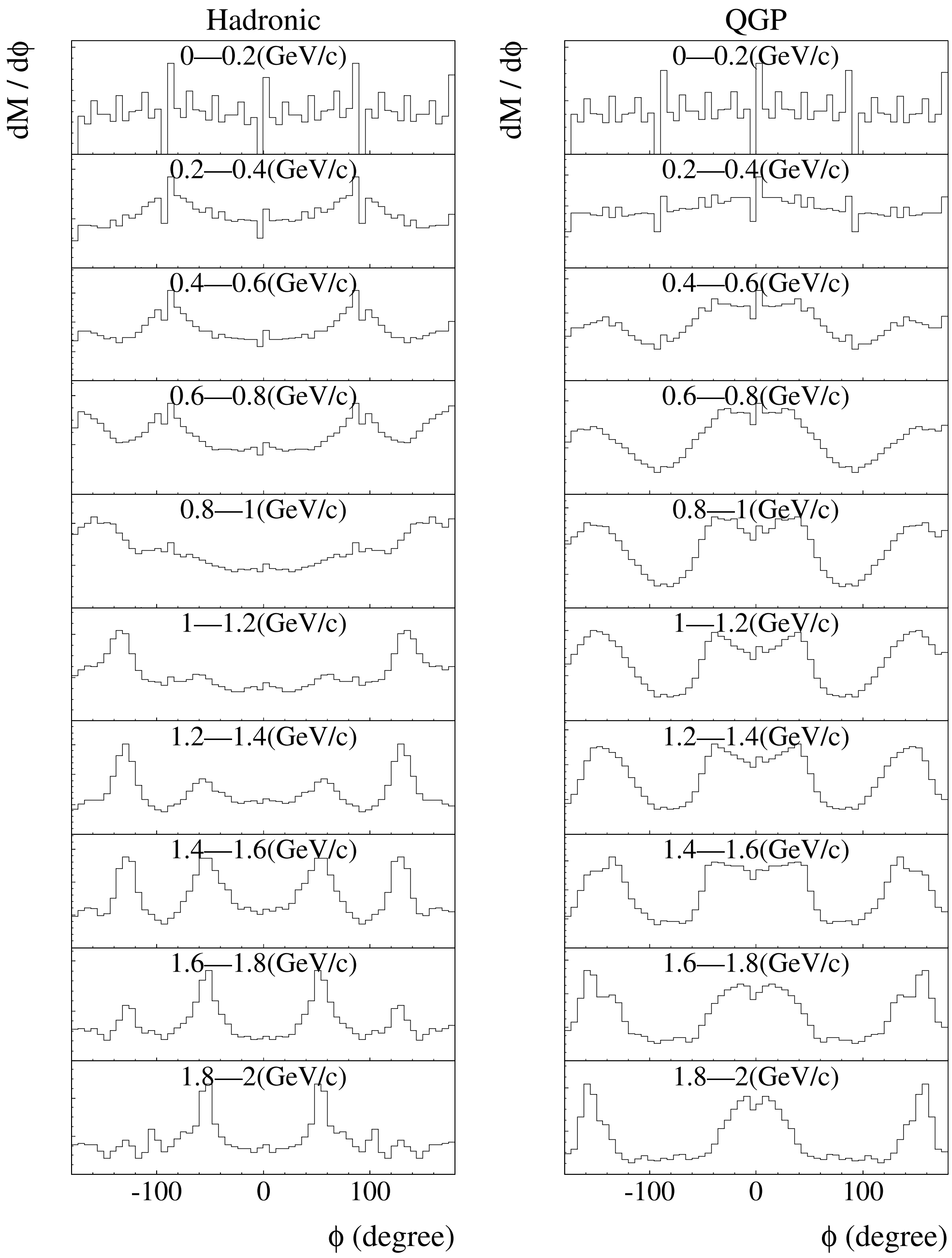

Figure 5.11: Azimuthal distributions $\frac{dM}{d\phi}$ for different p_t bins in a rapidity window $1.0 < y < 1.1$ from a hydrodynamical calculation for hadronic (left) and QGP (right) scenarios [85]. The centrality is $b = 5.56$ fm.

Triple differential cross section:

Fig. 5.10 displays the differential cross section $d^2M/dp_x dp_y$ in each rapidity bin for the hadronic (top) and the QGP scenario (bottom). The impact parameter for these two events is 5.66 fm. A rather complicated anisotropic distribution is seen for the hadronic scenario, whereas a smooth, yet anisotropic, event shape is seen for the QGP scenario. The azimuthal distribution $dM/d\phi$ for different p_t bins in the rapidity window $1.0 < y < 1.1$ is plotted in Fig. 5.11. For the hadronic scenario (left panel), the first four bins ($p_t < 0.8$ GeV/c) demonstrate a strong second harmonic, oriented such that $\psi_2 = \pi/2$. This is the so called squeeze-out flow where particles are emitted preferentially perpendicular to the reaction plane. Note though the rapidity window is not at $y_{\text{c.m.s.}} = 1.6$. In the fifth bin ($0.8 < p_t < 1.0$ GeV/c), the first harmonic is dominating, corresponding to sideward flow. The direction of flow is $\psi_1 = \pi$ because the rapidity window here is located backward with respect to mid-rapidity. The forth harmonic is clearly seen (with $\psi_4 \simeq \pi/4$, see discussion in Sec. 2.3.3) in the $dM/d\phi$ distributions in the high p_t bins ($1.2 < p_t < 1.8$ GeV/c). For the QGP scenario (right panel), the second harmonic dominates for $p_t > 0.4$ GeV/c. Contrary to the squeeze-out flow in the hadronic scenario, here particles are emitted preferentially in the reaction plane direction ($\psi_2 = 0$ or π). The low p_t particles ($0.2 < p_t < 0.4$ GeV/c) shows some sideward flow as the main component, but $\psi_1 = 0$ is unexpected from a convention in the backward rapidity. This is the cause of some of the reversed flow angle observed in Fig. 5.9. We draw two conclusions from this study. First, the detailed azimuthal distribution is sensitive to the EOS, and Fourier analysis is a valuable tool to detect possibly complicated event shapes. Second, the stiffer EOS produces more complicated the event shapes with higher harmonic components, especially in the high p_t region. To turn this argument around, the observation of a strong higher moment could prove the existence of a highly collective motion governed by hydrodynamics. At least there are no cascade models at present that are capable of producing such complicated azimuthal distributions.

Signature for the QGP phase transition:

The same model was used to calculate the sideward flow signal for different beam energies [82]. Fig. 5.12 shows $\langle p_x \rangle$ as a function of beam kinetic energy. The collision system is Au on Au, with an impact parameter b =3 fm. The QGP phase starts to emerge at $E_b^{\text{lab}}/A = 1$ GeV. It softens the EOS and reduces the pressure in the collision system, and consequently suppresses the

Figure 5.12: The transverse flow, $\langle p_x \rangle$, as a function of beam kinetic energy in the hydrodynamical calculation. This figure is reproduced from [82].

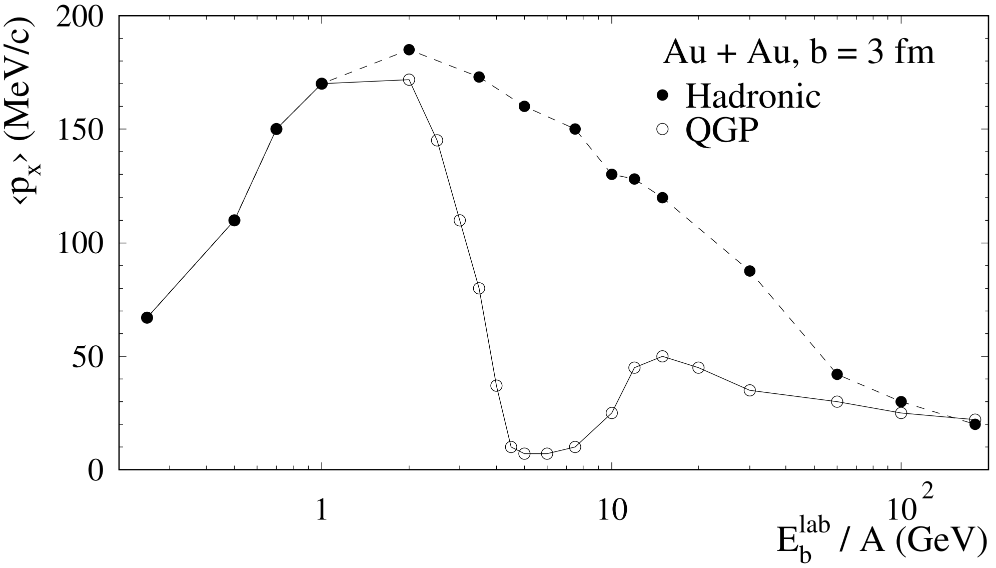

transverse flow. We discussed this qualitatively in Chapter 1 as one of the motivations for flow study. In reality, the starting point for the phase transition may be different from this calculation, but the qualitative features, including a drastic change as a function of the beam energy, and the appearance of minimum in the flow signal at certain beam energy, should exist, and can be used as a signature for the QGP phase transition.

5.3 Discussion

Since hydrodynamics treats the heavy ion collisions at a macroscopic level with only a few equations, it has the advantage of anticipating new physics, which can be put into the EOS. But the two strong assumptions it is based on may not be justified in the case of heavy ion collisions. First, it assumes local equilibrium at every instant throughout the collision, and colliding fluid elements are forced by momentum conservation to stop instantaneously. This assumption may be valid for the expansion stage of the collision, but probably not for the initial stage. One solution is to consider multi-fluid [86, 87] scenarios, where local equilibrium is only assumed within each fluid. Second, the continuum assumption is only justified for macroscopically large system, as *e. g.*, the collision of a two neutron stars. In heavy ion collisions, we have a finite number of nucleons of the order of 400 at maximum.

The non-equilibrium and finite size effects are naturally accounted for in the cascade models like RQMD. It is based on the known two-body hadron-hadron interactions, and assumes that the many-body problem can be adequately described in terms of two-body interactions. However, it is difficult to implement new collective physics, like a phase transition, where many-body effects can be very strong.

The two approaches seem to be complementary to each other. But in my view they should find their common ground in a sufficiently large collision system. A recent study by N. Xu has revealed a sort of hydrodynamic behavior of RQMD [88] for Au on Au and Pb on Pb collisions at AGS and SPS energies, respectively. This means that the finite size effects do not rule out applications of hydrodynamics when comparing to the present experiment.

Concerning the comparison to experimentally observed flow effects at the AGS, it appears that reality is in between the two models applied.

Chapter 6

Conclusions

6.1 Summary

In this thesis, we present our measurements of transverse energy with a nearly 4π solid angle for Au on Au collisions at a beam momentum of 11.4 A·GeV/c. The total transverse energy production for the central collisions is somewhat less than that from a 3-D isotropic fireball, but well accounted for if longitudinal expansion is taken into consideration. The correlation between global variables shows much reduced fluctuations in the Au on Au collisions compared to Si on Al collisions. The pseudorapidity distribution from TCAL matches well with the one from PCAL in all centrality bins. Most importantly, anisotropic event shapes and sideward flow were observed for the first time at the AGS energy. The azimuthal anisotropy was measured as a function of centrality, and shows a maximum for semi-central collisions. The measured transverse energy flow is larger than that predicted by the RQMD model in its cascade mode, but smaller than the prediction given by a one-fluid hydrodynamical model.

Our method of Fourier analysis was applied for the first time in flow analyses, and has proven to be effective. It is especially useful if the momentum of single particles is not measured, but rather, only the azimuthal distribution of a global observable like the transverse energy or multiplicity. The calorimeters used in the analysis served well in measuring the energy flow, and in determining the reaction plane. This is the starting point for more detailed exclusive measurements in future.

6.2 Outlook

We discuss two issues concerning flow analyses in the future.

Detailed Exclusive Measurements:

In the near future, the goal of the flow analysis for E877 and other AGS experiments is to measure particle azimuthal distributions in a detailed, exclusive fashion. Specifically, experiments will aim to measure the triple differential cross sections for many hadron species, including protons, pions, kaons, heavy clusters, even resonances, anti-protons and anti-clusters.

The method used in this thesis requires 2π azimuthal acceptance, which is not the case for most spectrometers. The alternative approach, as discussed briefly in Sec. 4.3.4, is to measure the reaction plane event-by-event in one detector (which should have a 2π azimuthal acceptance over a finite pseudo-rapidity interval), and then to obtain the azimuthal distribution of particles from another detector (*e. g.*, a spectrometer) relative to the measured reaction plane. However, the azimuthal distribution is smeared by fluctuations in the measured orientation of reaction plane. Thus, it is important to correct the measured distribution back to the primary one.

Let $r(\phi - \psi_r)$ and $r'(\phi - \psi_1)$ be the primary and measured azimuthal distributions, where ϕ is the measured particle emission angle, ψ_r and ψ_1 are the true and measured reaction plan angles. Both can be expanded in terms of Fourier series,

$$r(\phi - \psi_r) = \frac{1}{2\pi} + \frac{1}{\pi}\sum_{n=1}^{\infty}[v_n \cos n(\phi - \psi_r)], \tag{6.1}$$

$$r'(\phi - \psi_1) = \frac{1}{2\pi} + \frac{1}{\pi}\sum_{n=1}^{\infty}[v'_n \cos n(\phi - \psi_1)]. \tag{6.2}$$

The sine terms drop out since both r and r' are even functions. The difference between the measured and true reaction angle, $\psi_1 - \psi_r \equiv \psi$, follows a distribution (2.39), denoted as $\mathcal{F}(\psi)$ here. If the emissions of particles in the two detectors are independent, the measured distribution $r'(\phi - \psi_1)$ is the convolution of the primary distribution $r(\phi - \psi_r)$ with the reaction plane dispersion $\mathcal{F}(\psi)$:

$$r'(\phi - \psi_1) = \int_{-\pi}^{\pi} r[(\phi - \psi_r) + \psi]\, \mathcal{F}(\psi)\, d(\psi). \tag{6.3}$$

Inserting the Fourier expansions to Eq. (6.3), one obtains the relation between the measured and the true Fourier coefficients,

$$v'_n = v_n \int_{-\pi}^{\pi} \cos(n\psi)\mathcal{F}(\psi)d\psi = v_n\langle\cos(n\psi)\rangle. \tag{6.4}$$

In Sec. 2.5, we discussed $\langle\cos(\psi)\rangle$ in Eq. (2.42) and Fig. (2.8). This can be generalized to $\langle\cos(n\psi)\rangle$, which is derived, and its dependence on the parameter $\tilde{\chi}_1 = \tilde{v}_1/\sigma$ is given in [89]. For a given $\tilde{\chi}_1$, the larger The n, the smaller the value of $\langle\cos(n\psi)\rangle$, which means for the higher harmonics, v_n' is largely reduced from the real value of v_n, thus it is increasingly difficult to detect.

Nevertheless, in principle, Eq. (6.4) provides a means to recover the azimuthal distribution from the dispersion of the measured reaction plane orientation. If one constructs and corrects the azimuthal distribution in all p_t and y bins, the full triple-differential cross sections in the second detector's acceptance can be obtained.

Systematic and Multi-dimensional Analysis:

We measured and discussed the centrality dependence of the flow signal. For a complete systematic study, it would be desirable to do flow measurements at different beam energies. As discussed in Chapters 1 and 5, the QGP phase transition should reduce the pressure and hence the flow signal. Hopefully, the appearance of the transition will be sharp as a function of beam energy and/or impact parameter, so that a sudden change can be observed. But the finite collision system and possibly large fluctuations may smear out the discontinuity into a smooth transition over a wide range of beam energies and impact parameters. In this case, it will be difficult to identify the phase transition. To overcome this difficulty, one solution is to undertake a multi-dimensional event-by-event analysis, which would be possible for Au on Au collisions at the RHIC, where the multiplicity is sufficiently high. First, one would collect all the event-by-event observables, including the global variables (M, E_T, and E_z), thermal variables ("temperature" parameter, T, for protons and pions), QGP signatures (such as the kaon/pion ratio), and flow quantities (Fourier coefficients v_n, flow velocity). Then, one would check to see if there is a positive multi-correlation between these variables. For example, if events with given E_z and high M or E_T coincide with events with high large kaon/pion ratio but small flow signal, they are possibly the QGP events. A sharper transition might be observed in the ratio of the QGP events over the normal events as a function of centrality (E_z) and beam energy, which would be a strong evidence for the phase transition.

The optimistic view for the future of relativistic heavy physics is that the RHIC energy is far beyond the transition region and is deep inside the QGP phase, so that the latter will be observed immediately after RHIC is turned on in 1999. We hope this will be the case. But as long as there still is a theoretical alternative to explain the signatures of the QGP by pure hadronic physics, we will have to locate experimentally the transition point, which may require varying RHIC's energy between 30 GeV and 100 GeV, where the multi-dimensional analysis described above could be important. We are looking forward to the exciting moment of discovery of the QGP phase transition in the years to come.

Bibliography

[1] F. Capra, *The Tao of Physics*, Shambhala Publications, Inc., Boston, (1991).

[2] J. C. Collins, M. Perry, Phys. Rev. Lett. **34**, 1353 (1975); E. V. Shuryak, Phys. Rep. **68**, 71 (1980).

[3] S. Nagamiya, Banquet Speech presented at 4th International Conference on Nucleus-Nucleus Collisions, Kanazawa, Japan, June 10-14, 1991.

[4] J. Stachel, and G. R. Young, Annu. Rev. Nucl. Part. Sci. **42**, 237 (1992).

[5] T. W. Ludlam, H. E. Wegner, eds., Proc. Quark Matter '83, Nucl. Phys. **A418** (1984);

[6] L. S. Schröder, M. Gyulassy, eds., Proc. Quark Matter '86, Nucl. Phys. **A461** (1987);

[7] H. Satz, R. Stock, H. J. Specht, eds., Proc. Quark Matter '87, Z. Phys. **C38** (1988);

[8] G. Baym, P. Braun-Munzinger, S. Nagamiya, eds., Proc. Quark Matter '88, Nucl. Phys. **A498** (1989);

[9] J. P. Blaizot, *et al.*, Proc. Quark Matter '90, Nucl. Phys. **A525** (1991);

[10] T. C. Awes, F. E. Obenshain, F. Plasil, M. R. Strayer, and C. Y. Wong, eds., Proc. Quark Matter '91, Nucl. Phys. **A544** (1992);

[11] E. Stenlund, H. A. Gustafsson, A. Oskarsson, and I. Otterlund, eds., Proc. Quark Matter '93, Nucl. Phys. **A566** (1994);

[12] Proc. Quark Matter '95, Nucl. Phys. **A**, in print.

[13] J. Barrette, *et al.*, E814 Collaboration, Phys. Rev. Lett. **64**, 1219 (1990).

[14] J. Barrette, *et al.*, E814 Collaboration, Phys. Rev. Lett. **70**, 2996 (1993).

[15] J. Barrette, *et al.*, E814 Collaboration, Z. Phys., **C59**, 211 (1993).

[16] J. Dee, Ph.D. thesis, SUNY at Stony Brook (1995).

[17] J. T. Mitchell, *et al.*, LBL Report LBL-35810, (1994).

[18] J. Stachel, *et al.*, E814 Collaboration, Nucl. Phys. **A566**, 183c (1994).

[19] P. Braun-Munzinger, J. Stachel, J. P. Wessels, and N. Xu, Phys. Lett. **B344**, 43 (1995).

[20] J. Barrette, *et al.*, E814 Collaboration, Phys. Lett. **B333**, 33 (1994).

[21] H. A. Gustafsson, *et al.*, Phys. Rev. Lett. **52**, 1590 (1984).

[22] U. Heller, and K. Kersch, Nucl. Phys. **B251**, 254 (1985).

[23] T. Cerik, J. Engels, and H. Satz, Nucl. Phys. **B256**, 670 (1985); F. R. Brown, *et al.*, Phys. Rev. Lett. **65**, 2491 (1990).

[24] W. Scheid, H. Müller, and W. Greiner, Phys. Rev. Lett. **32**, 741 (1974).

[25] H. Heckman, *et al.*, Phys. Rev. **C17**, 1651 (1978).

[26] H. Wieman, *et al.*, Proc. Quark Matter '90, Nucl. Phys. **A525**, 617c (1991).

[27] H. H. Gutbrod, A. M. Poskanzer, and H. G. Ritter, Rep. Prog. Phys. **52**, 1267 (1989).

[28] H. Stöcker, and W. Greiner, Phys. Rep. **137**, 277 (1986).

[29] J. Cugnon, J. Knoll, C. Riedel, and Y. Yariv, Phys. Lett. **B109**, 167 (1982).

[30] A. Bonasera, L. P. Csernai, and B. Schürmann, Nucl. Phys. **A476**, 159 (1988).

[31] W. Schmidt, *et al.*, Phys. Rev. **C47**, 2782 (1993).

[32] G. F. Bertsch, and S. Das Gupta, Phys. Rep. **160**, 189 (1988); W. Cassing, and U. Mosel, Prog. Part. Nucl. Phys. **25**, 235 (1990).

[33] P. Danielewicz, Phys. Rev. **C51**, 716 (1995).

[34] G. David, PhD thesis, SUNY at Stony Brook (1991).

[35] T. Abbott, *et al.*, the E802 Collaboration, Phys. Rev. Lett. **70**, 1393 (1993).

[36] P. Danielewicz, and G. Odyniec, Phys. Lett. **B157**, 146 (1985).

[37] M. Gyulassy, K. A. Frankel, and H. Stöcker, Phys. Lett. **B110**, 185 (1982).

[38] P. Danielewicz, and M. Gyulassy, Phys. Lett. **B129**, 283 (1983).

[39] J. Ollitrault, Phys. Rev. **D46**, 229 (1992).

[40] J. Ollitrault, Phys. Rev. **D48**, 1132 (1993).

[41] S. Wang, *et al.*, Phys. Rev. **C44**, 1091 (1991).

[42] J. Jiang, *et al.*, Phys. Rev. Lett. **68**, 2739 (1992).

[43] J. Cugnon, and D. L'Hôte, Nucl. Phys. **A452**, 738 (1986).

[44] E. Farhi, Phys. Rev. Lett. **39**, 1237 (1977).

[45] J. Kapusta, and D. Strottman, Phys. Lett. **B106**, 33 (1981).

[46] S. Voloshin, and Y. Zhang, preprint hep-ph/9407282 (July 1994).

[47] J. Gosset, *et al.*, Phys. Lett. **B247**, 233 (1990).

[48] J. Barrette, *et al.*, E877 Collaboration, Phys. Rev. **C49**, 1669 (1994).

[49] J. Barrette, *et al.*, E877 Collaboration, Phys. Rev. **C51**, 3309 (1995).

[50] B. Hong, PhD thesis, SUNY at Stony Brook (1995).

[51] L. S. Waters, PhD thesis, SUNY at Stony Brook (1990).

[52] Z. Zhang, PhD thesis, Univ. of Pittsburgh (1993).

[53] J. Simon-Gillo, PhD thesis, Texas A&M Univ. (1992).

[54] Z. Zhang, P. Braun-Munzinger, W. E. Cleland, G. David, and D. Lissauer, Nucl. Instr. Meth. **A343**, 610 (1994).

[55] W. J. Llope, PhD thesis, SUNY at Stony Brook (1991).

[56] W.-C. Chang, private communication, July 1995.

[57] P. Braun-Munzinger, and J. Stachel, Phys. Lett. **B216**, 1 (1989).

[58] R. Albrecht, *et al.*, WA80 Collaboration, Phys. Rev. **C44**, 2736 (1992).

[59] R. Brun, *et al.*, GEANT 3.15, CERN DD/EE/84-1, revised 92-1, 1992.

[60] T. Ludlam, A. Pfoh, and A. Shor, in "Proceedings of the RHIC Workshop I", Upton, BNL Report No. 51921, (1985).

[61] F. Paige, and S. Protopopescu, ISAJET: A Monte Carlo Event Generator for pp and $p\bar{p}$ Interactions, BNL, 1990.

[62] B. Nilsson-Almqvist, *et al.*, Comp. Phys. Comm. **43**, 387 (1987).

[63] Y. Pang, T. J. Schlagel, and S. H. Kahana, Phys. Rev. Lett. **68**, 2743 (1992).

[64] H. Sorge, H. Stöcker, and W. Greiner, Ann. Phys. **192**, 266 (1989).

[65] J. Barrette, *et al.*, E877 Collaboration, Phys. Rev. Lett. **73**, 2532 (1994).

[66] Y. Zhang, and J. P. Wessels, for the E877 Collaboration, Proc. Quark Matter '95, Nucl. Phys. **A**, in print.

[67] J. P. Wessels, for the E877 Collaboration, Proceedings of 10^{th} Winter Workshop on Nuclear Dynamics, Keywest (1995), in print; W.-C. Chang, private communication, 1995.

[68] J. Barrette, *et al.*, E877 Collaboration, manuscript in preparation; S. Voloshin, private communication, 1995.

[69] Z. Chen, AGS users meeting, June 1995.

[70] H. Sorge, H. Stöcker, and W. Greiner, Nucl. Phys. **A498**, 567c (1989); H. Sorge, A. v. Keitz, R. Mattiello, H. Stöcker, and W. Greiner, Z. Phys. **C47**, 629 (1990); H. Sorge, R. Mattiello, H. Stöcker, and W. Greiner, Phys. Lett. **B271**, 37 (1991).

[71] B. Andersson, G. Gustafson, and B. Nilsson-Almqvist, Nucl. Phys. **B281**, 289 (1987).

[72] G. Peilert, H. Stöcker, and W. Greiner, Rep. Prog. Phys. **57**, 533 (1994).

[73] S. Gagan, and Y. Oren, PROPHET, Calorimeter Simulation Program, Helios Notes #184, CERN

[74] D. Fox, *et al.*, Nucl. Instr. Meth. **A317**, 474 (1992).

[75] H. Stöcker, *et al.*, Proc. Quark Matter '95, Nucl. Phys. **A**, in print.

[76] R. Mattiello, PhD thesis, Univ. Frankfurt, 1995.

[77] H. Sorge, A. v. Keitz, R. Mattiello, H. Stöcker, and W. Greiner, Phys. Lett. **B243**, 7 (1990).

[78] D. Miśkowiec, for the E877 Collaboration, Proc. Quark Matter '95, Nucl. Phys. **A**, in print.

[79] D. Strottman, Nucl. Phys. **A566**, 245c (1994).

[80] L. Bravina, L. P. Csernai, P. Lévai, and D. Strottman, Phys. Rev. **C50**, 2161 (1994).

[81] D. H. Rischke, *et al.*, preprint Nucl-Th-9505014.

[82] Y. Pürsün, PhD thesis, Univ. Frankfurt, 1994.

[83] A. Chodos, R. L. Jaffe, K. Jonson, C. B. Thorn, V. F. Weisskopf, Phys. Rev. **D50**, 3471 (1974).

[84] M. I. Gorenstein, D. H. Rischke, H. Stöcker, and W. Greiner, J. Phys. **G19**, L69 (1993).

[85] U. Katscher, and D. H. Rischke, private communication, 1994.

[86] L. P. Csernai, I. Lovas, J. A. Maruhn, A. Rosenhauer, J. Zimanyi, and W. Greiner, Phys. Rev. **C28**, 264 (1982).

[87] U. Katscher, D. H. Rischke, J. A. Maruhn, W. Greiner, I. N. Mishustin, L. M. Satarov, UFPT preprint 312, 1992.

[88] N. Xu, private communication, 1995.

[89] W.-C. Chang, E877 note #SUNYSB-95-001, March 1995.

Appendix A

Central Limit Theorem

Proof of the central limit theorem can be found in text books. Here we only give the theorem and derive the forms used in this thesis. We also examine the condition, or the limit for using this theorem.

A.1 Central Limit Theorem

If x_1, x_2, ..., x_M are independent variables following the same distribution with mean value $Mx_i = \tilde{x}$ and variance $Dx_i = \sigma^2$, then

$$\lim_{M\to\infty} P\left(\frac{1}{\sqrt{M}\sigma}\sum_{\nu=1}^{M}(x_\nu - \tilde{x}) < y\right) = \frac{1}{\sqrt{2\pi}}\int_{-\infty}^{y}\exp\left(-\frac{t^2}{2}\right)dt. \tag{A.1}$$

Let $\sum_{\nu=1}^{M} x_\nu \equiv v_x$, $\sum_{\nu=1}^{M}\tilde{x} = M\tilde{x} \equiv \tilde{v}_x$, and $\sigma_x = \sqrt{M}\sigma$ from (A.1) we have

$$\frac{dP}{dv_x} = \frac{1}{\sqrt{2\pi}\sigma_x}\exp\left(-\frac{(v_x - \tilde{v}_x)^2}{2\sigma_x^2}\right), \tag{A.2}$$

which is a Gaussian distribution with a centroid $\tilde{v}_x$ and a variance σ_x.

For a 2-D independent distribution (x_1, y_1), (x_2, y_2), ..., (x_M, y_M), one gets the 2-D probability distribution for v_x and v_y as the product of Eq. (A.2) in x and y,

$$\frac{dP^2}{dv_x dv_y} = \frac{dP}{dv_x}\cdot\frac{dP}{dv_y} = \frac{1}{2\pi\sigma_x\sigma_y}\exp\left(-\frac{(v_x - \tilde{v}_x)^2}{2\sigma_x^2} - \frac{(v_y - \tilde{v}_y)^2}{2\sigma_y^2}\right), \tag{A.3}$$

where $\tilde{v}_y$ and σ_y and defined the same way as $\tilde{v}_x$ and σ_x. In case $\sigma_x = \sigma_y$, one can transform distribution (A.3) to a polar coordinate to obtain $\dfrac{d^2P}{vdv\,d\psi}$ as in Eq. (2.32) with $\tilde{v}_x = \tilde{v}_y = 0$ and Eq. (2.34) with $\tilde{v}_x = \tilde{v}$ and $\tilde{v}_y = 0$.

A.2 Limit Test of the "Central Limit"

Central limit theorem is valid only if $M \to \infty$. In data analysis M is finite, corresponding to particle multiplicity in certain (pseudo)rapidity window within experimental acceptance. This raises the question of how large M should be to have Eqs. (A.2–A.3) valid. Firstly, if x_ν distribution itself is a Gaussian, Eqs. (A.2–A.3) are true even for $M = 1$. Normally particle distributions $d^2M/p_t dp_t$ are rather close to Gaussian at low p_t, while closer to exponential at high p_t, which means the above equations should hold even for low multiplicity events. Secondly, for a given x_ν distribution, Monte Carlo studies can help us to find a critical number M_1; for $M > M_1$ the summed distribution is close to a Gaussian distribution. In Fig. A.1, for an input 1-D flat distribution x_ν (from -1 to 1, $\sigma = 1/\sqrt{3}$), the summed distributions dP/dv_x are fitted with Gaussian distributions for a number of multiplicities. Fit parameters σ and χ^2 are shown in Fig. A.3 (left figures). The σ_x from the Gaussian fitting (solid lines) and the expected value from central limit theorem, $\sqrt{M}/\sigma = \sqrt{M/3}$, are almost identical. However, the reduced χ^2 does depend strongly on M. It drops to a value of 1.0 for $M > 4$.

Similar calculations are done for a 2-D flat distribution, which is a constant within a radius $r < 1$ and 0 otherwise. We examine how does distribution of $v = \sqrt{v_x^2 + v_y^2}$ compare to Eq. (2.32). Fig. A.2 shows dP/vdv distributions from Monte Carlo and the fitted Gaussian distributions. The values of σ from the fit are compared with the expected values (shown Fig. A.3, upper-right), where they are again very close to each other. The reduced χ^2, on the other hand, decreases to a value of 1.0 around $M = 10$. We conclude that the critical or "limit" numbers are $M = 5$ for 1-D and $M = 10$ for 2-D. This conclusion depends on the input distribution as well as the number of events.

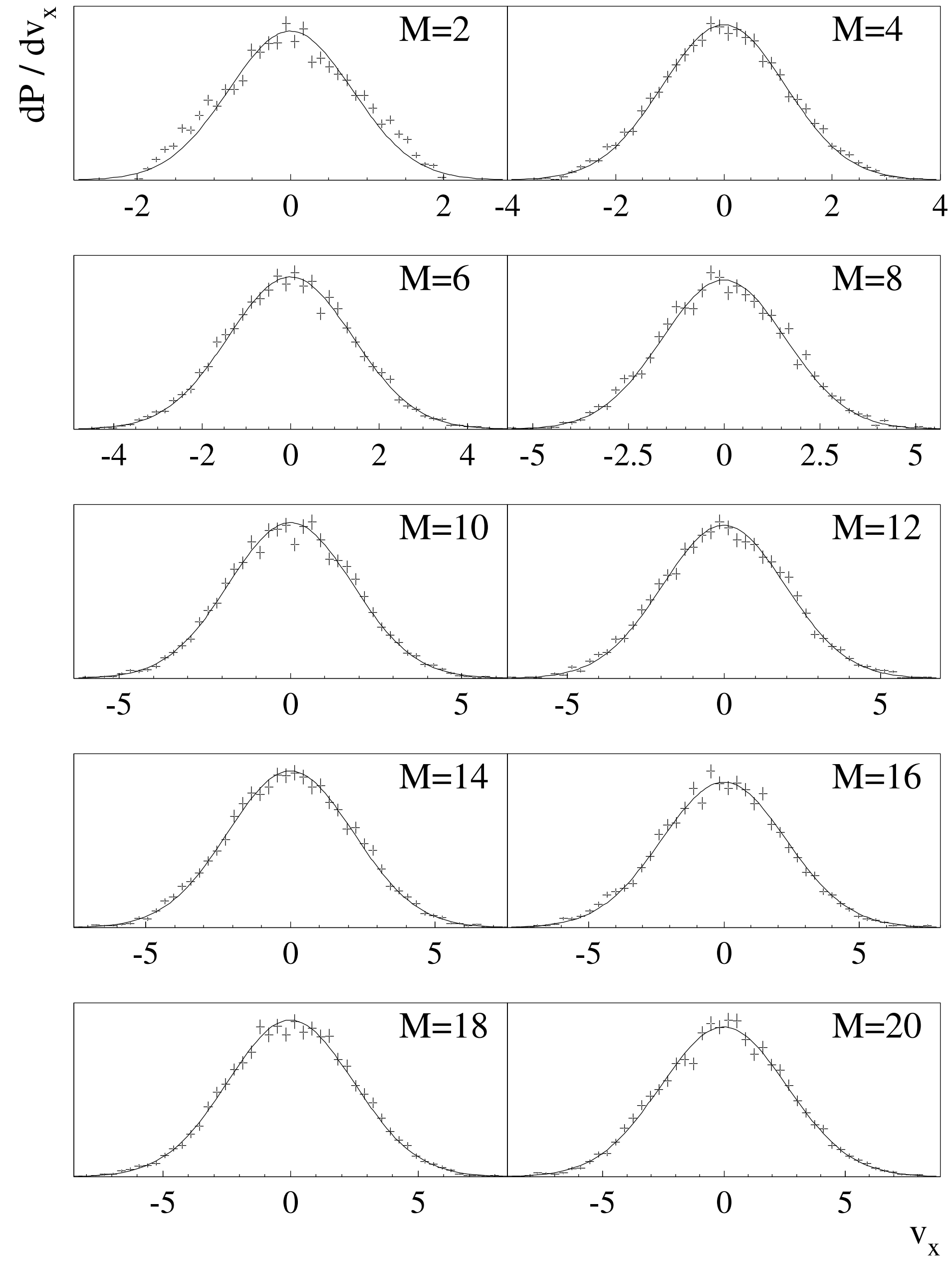

Figure A.1: Distribution of the summed variable, $v_x = \sum_{\nu=1}^{M} x_\nu$, where x_ν follows a flat distribution, from Monte Carlo (dots) are compared to Gaussian fits (lines) for different values of M. There are 8,000 events in Monte Carlo calculations.

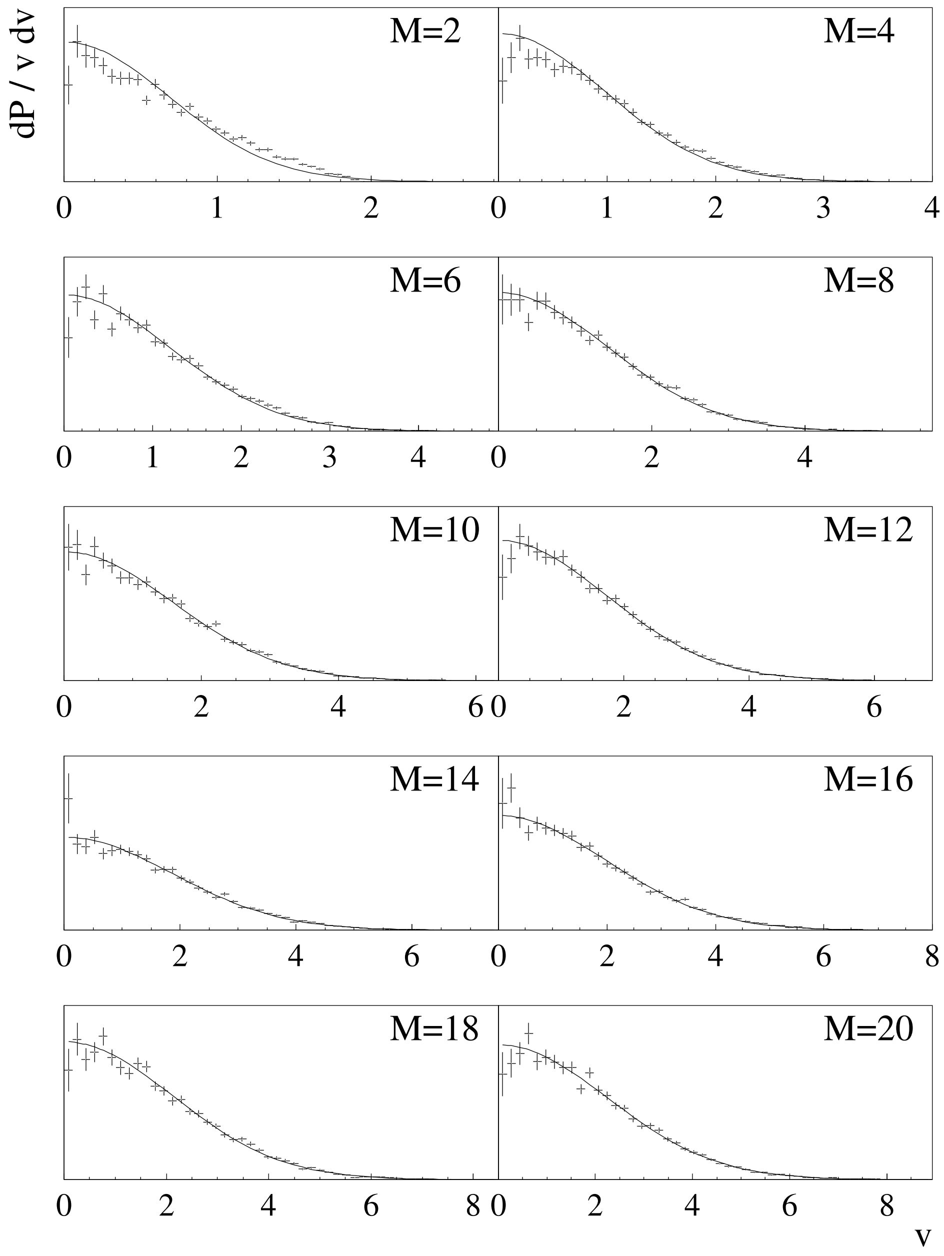

Figure A.2: Distribution of the summed variable $v = \sqrt{v_x^2 + v_y^2}$ from Monte Carlo (dots) are compared to Gaussian fits (lines) for different values of M. There are 8,000 events in Monte Carlo calculations for each value of M.

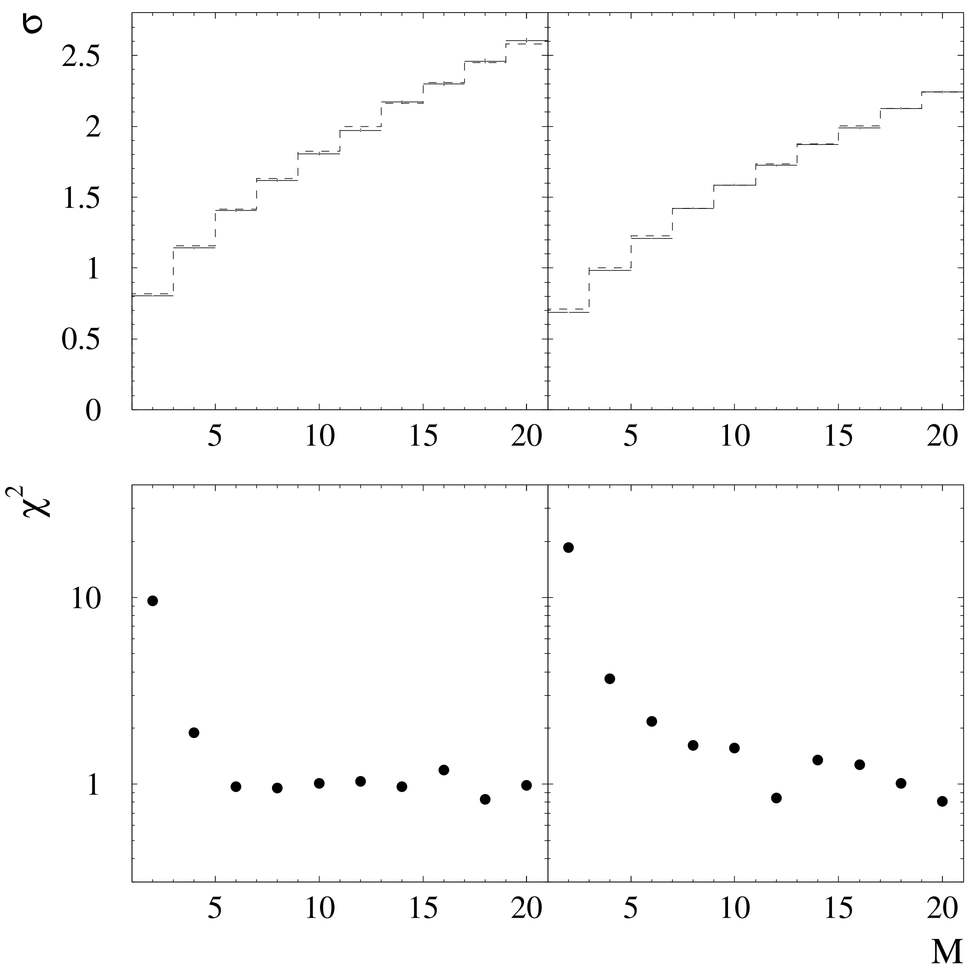

Figure A.3: The σ (solid histograms) and χ^2 (dots) from the Gaussian fits in Fig. A.1 (left figures) and in Fig. A.2 (right figures) as a function of multiplicity. Dashed lines are the expected value from the central limit theorem.

Appendix B

Modified Bessel Function

The modified Bessel function $I_\nu(y)$ is one of the following solutions[1] of differential equation

$$y^2 \frac{d^2 w}{dy^2} + y \frac{dw}{dy} - (y^2 + \nu^2) = 0, \tag{B.1}$$

and can be written in ascending series:

$$I_\nu = (\frac{y}{2})^\nu \sum_{k=0}^{\infty} \frac{(\frac{y^2}{4})^k}{k!\,\Gamma(\nu + k + 1)}. \tag{B.2}$$

Recurrence and derivative relations can be derived from this,

$$\frac{2\nu}{y} I_\nu(y) = I_{\nu-1}(y) - I_{\nu+1}(y), \tag{B.3}$$

$$2\frac{d\,I_\nu(y)}{dy} = I_{\nu-1}(y) + I_{\nu+1}(y). \tag{B.4}$$

Taking $\nu = n$ as an integer, $I_n(y)$ can be expressed in a integral form:

$$I_n(y) = \frac{1}{2\pi} \int_0^{2\pi} \exp(y \cos\psi) \cos(n\psi) d\psi. \tag{B.5}$$

We are interested only in the case that y is a positive real number. It is obvious that $I_n(y) = I_{-n}(y) > 0$ for $y > 0$. For $y = 0$ we have $I_n(0) = 0$ $(n \neq 0)$ and $I_0(0) = 1$. The condition for distribution (2.35) to exhibit extrema is the derivative of (2.35) to be zero,

$$\frac{d}{d\chi} \left[\exp(-\frac{\tilde{\chi}^2}{2} - \frac{\chi^2}{2})\, I_0(\tilde{\chi}\chi) \right] = 0. \tag{B.6}$$

[1] The other is $K_\nu(y)$, not used in the data analysis.

Let us define $y \equiv \tilde{\chi}\chi$, the above equation becomes

$$\tilde{\chi}^2 I_1(y) = y\, I_0(y), \tag{B.7}$$

which is the same as Eq. (2.36). There is alway a solution $y = 0$, indicating that distribution (2.35) has a extrema at $\chi = 0$. A non-zero solution $y > 0$ is more interesting, corresponding to a maximum at $\chi > 0$. To find the criteria for the existence of a maximum at $\chi > 0$, we examine the behavior of the function $f(y) \equiv \tilde{\chi}^2 = y\, I_0(y)/I_1(y)$. We first check $f(0)$ using the derivative relation (B.4),

$$f(0) = \frac{\lim\limits_{y\to 0} y\, I_0(y)}{\lim\limits_{y\to 0} I_1(y)} = \frac{\lim\limits_{y\to 0} \dfrac{d}{dy}[y\, I_0(y)]}{\lim\limits_{y\to 0} \dfrac{d}{dy}[I_1(y)]} = \frac{I_0(0) + 0\, I_1(0)}{\frac{1}{2} I_0(0) + \frac{1}{2} I_2(0)} = 2. \tag{B.8}$$

From recurrence relation (B.3) we have $2\, I_1(y)/y = I_0(y) - I_2(y)$, which yields

$$f(y) = \frac{y\, I_0(y)}{I_1(y)} = 2 + \frac{y\, I_2(y)}{I_1(y)} > 2,\ (y > 0). \tag{B.9}$$

In order to have a positive solution for Eq. (B.7), parameter $\tilde{\chi}^2$ should be greater than 2, or $\tilde{\chi} > \sqrt{2}$.

Appendix C

The Method of Maximum Likelihood

Let us take $n = 1$ in 2-D Gaussian distribution (2.35) and re-write it as:

$$\frac{d^2 w}{\chi d\chi d(\psi - \psi_r)} = \frac{1}{2\pi} \exp\left(-\frac{\tilde{\chi}^2}{2} - \frac{\chi^2}{2} + \tilde{\chi}\chi \cos(\psi - \psi_r) \right). \tag{C.1}$$

It gives (χ, ψ) probability distribution around the sideward flow parameter $(\tilde{\chi} = \tilde{v}_1/\sigma)$ and the reaction plane angle (ψ_r). We define $\mathcal{L}(\psi_r) = f(\psi_r;\, \psi, \tilde{\chi}, \chi)$ as the above distribution (C.1), where $\mathcal{L}(\psi_r)$ is called likelihood. Equation

$$\frac{\partial \mathcal{L}}{\partial \psi_r} = 0 \tag{C.2}$$

gives the maximum likelihood estimate of the reaction plane, which simply yields $\psi_r = \psi$. If there are m rapidity windows, the likelihood should be the product of the probability distributions (C.1) in all windows $\mathcal{L}(\psi_r) = \prod_i^m f(\psi_r;\, \psi_i, \tilde{\chi}_i, \chi_i)$,

$$\mathcal{L}(\psi_r) = \frac{1}{(2\pi)^m} \exp\left(\sum_i^m [-\frac{\tilde{\chi}_i{}^2}{2} - \frac{\chi_i^2}{2} + \tilde{\chi}_i\chi_i \cos(\psi_i - \psi_r)] \right). \tag{C.3}$$

Put this into Eq. (C.2), we obtain the estimate of the reaction plane,

$$\psi_r = \arctan \frac{\sum_i^m \tilde{\chi}_i\chi_i \sin\psi_i}{\sum_i^m \tilde{\chi}_i\chi_i \cos\psi_i}. \tag{C.4}$$

This is the same as Eq. (2.44) if we replace the summation over all windows with summation over all particles in all windows. Note that $\tilde{\chi}_i$ comes with a positive or a negative sign; positive if the sideward flow goes into the same direction as the impact parameter, and negative if it goes the opposite direction.